Titre: Title:	In Situ Studies of Volatile Molecules Trapping in Zirconium Alloy-Based Non-Evaporable Getter
Auteur: Author:	Zeinab Abboud
Date:	2016
Type:	Mémoire ou thèse / Dissertation or Thesis
Référence: Citation:	Abboud, Z. (2016). In Situ Studies of Volatile Molecules Trapping in Zirconium Alloy-Based Non-Evaporable Getter [Mémoire de maîtrise, École Polytechnique de Montréal]. PolyPublie. https://publications.polymtl.ca/2382/

UNIVERSITÉ DE MONTRÉAL

IN SITU STUDIES OF VOLATILE MOLECULES TRAPPING IN ZIRCONIUM ALLOY-BASED NON-EVAPORABLE GETTER

ZEINAB ABBOUD

DÉPARTEMENT DE GÉNIE PHYSIQUE

ÉCOLE POLYTECHNIQUE DE MONTRÉAL

MÉMOIRE PRÉSENTÉ EN VUE DE L'OBTENTION

DU DIPLÔME DE MAÎTRISE ÈS SCIENCES APPLIQUÉES

(GÉNIE PHYSIQUE)

DÉCEMBRE 2016

UNIVERSITÉ DE MONTRÉAL

ÉCOLE POLYTECHNIQUE DE MONTRÉAL

Ce mémoire intitulé:

IN SITU STUDIES OF VOLATILE MOLECULES TRAPPING IN ZIRCONIUM ALLOY-BASED NON-EVAPORABLE GETTER

présenté par : ABBOUD Zeinab

en vue de l'obtention du diplôme de : Maîtrise ès sciences appliquées

a été dûment accepté par le jury d'examen constitué de :

M. DESJARDINS Patrick, Ph. D., président

M. MOUTANABBIR Oussama, Ph. D., membre et directeur de recherche

M. CHARETTE Paul, Ph. D., membre externe

DEDICATION

To Hala Ghazi,

Who was persistently pursuing her education until her last breath

May she rest in peace

ACKNOWLEDGEMENTS

I would like to express my deepest gratitude to individuals without whom this work would not be possible. First and foremost, to my supervisor Prof. Oussama Moutanabbir, for your trust, guidance, and support, this work and the progress I made in the past two years would not have been possible. Thank you. I would like to thank Professors Patrick Desjardins and Paul Charette for taking the time to review and provide input and suggestions to improve my thesis.

I sincerely thank my Polytechnique family, my colleagues, my friends, who have helped me throughout the past two years, brought joy, and so much laughter into my life. Thank you, to all of you, you have all contributed in one way or another in making this journey easier, and more enjoyable. Thanks to all the support staff from LMF, GCM, and Université de Montréal, your help and assistance have had tremendous influence on progressing my work. I would especially like to thank Josianne Lefebvre, who I am extremely grateful for, for her help, advice, and stress-relieving chats. Special thanks to Olga for dragging me out of my thesis cave whenever she got a chance to, the few times that I had taken a break from writing, were tremendously helpful in keeping me sane. Thank you. The work presented in this thesis would not have been possible without the help and input from collaborators from Teledyne DALSA Semiconductor, C2MI, and Université de Sherbrooke. Special thanks to Pascal Newby for his support and valuable input on this work. Thanks to Cédrik Coia for his advice. Cedric Spits, Jean-Sebastien Poirier, Jonathan Lachance, Luc Fréchette, Jean-Philippe Dery and Maxime Biron, thank you all for your time and help.

Nothing would have been possible without the endless support of my parents; mother, father, thank you for your faith in me and your prayers. My brothers, thank you for your help, and your little bundles of joy that always bring me happiness, no matter how short and seldom my visits were. Special thanks to my sister, Khadige, whose support and advice has brought me hope, no matter how harsh it was. I wish you all the best in your career, you deserve it. Thanks to my little twin-10 sister, Fatima, for all the laughter and cheesy comments. Best of luck in your next phase in life! I hope it will be full of success and joy.

My friends, Sarah and Malak, despite the distance, and the time we have been apart, you have always been, and remain to be true friends, thank you for all your support. Thanks to Judy, Anand, Jafar, and Mohamed for all your support and patience with me all these years. And last but not least, to Eugene, thank you for listening.

RÉSUMÉ

La demande pour le maintien du vide et l'expulsion de gaz résiduels dans les micro-cavités dans les systèmes microélectromécaniques (MEMS) et dans d'autres dispositifs micro-fabriqués a augmenté significativement lors des dernières années.. Les gaz résiduels empoisonnent souvent le vide et finissent par détériorer le fonctionnement des dispositifs. Afin de maintenir le vide dans les cavités, quelques étapes doivent être mises en œuvre: i) une étanchéité hermétique de la cavité doit être réalisée pour éliminer les fuites de gaz; ii) un dégazage approprié du système pour déloger et libérer les gaz piégés dans les matériaux est nécessaire avant de sceller de la cavité; Et iii) si nécessaire, incorporer une bande ou une couche mince d'un alliage métallique réactif agissant comme pompe chimique pour débarrasser le système des gaz résiduels pendant le fonctionnement du dispositif. De tels alliages sont connus sous le nom de *getters*, formés entre autres de métaux de transition actifs tels que Zr, Ti, V et Fe qui chimisorbent spontanément les gaz actifs dans les cavités. Pour améliorer l'efficacité de l'adsorption, une variété de systèmes de matériaux ont été proposés et testés, et deux caractéristiques semblent être critiques: (1) la morphologie (aire de surface); Et (2) la composition (réactivité physique et / ou chimique). Malgré leur importance technologique, peu de choses sont connues sur les mécanismes exacts de piégeage de gaz dans les matériaux. Ce projet aborde cette question en se basant sur des études *in situ* pour élucider la nature des réactions entre les constituants getters et les gaz résiduels et l'effet de la température d'activation sur la composition de surface et le piégeage des molécules volatiles.

Nos études ont porté sur les alliages de zirconium-cobalt-terres rares (REM) qui ont été conçus pour avoir une basse température d'activation (<350^{o}C) compatible avec les processus de fabrication et d'intégration de certains dispositifs MEMS. Des couches minces de ces alliages ont été pulvérisées sur Si. Les films obtenus sont très poreux, ce qui est critique pour réduire la température d'activation. La microscopie électronique à balayage (SEM), la spectroscopie de photoélectrons X (XPS), la spectrométrie de masse d'ions secondaires au temps de vol (TOF-SIMS) et la détection de recul élastique en temps de vol (TOF-ERD) ont été utilisées afin d'examiner la morphologie et la composition de la surface et du matériau massique. L'évolution de la surface en fonction de la température a été analysée *in situ* via XPS. Ce travail propose des mécanismes détaillés expliquant la réactivité à température ambiante et à haute température du matériau avec O_2, N_2 et CO_2.

Les résultats montrent que l'activation débute à 200ºC et n'est que partielle à 350ºC. Le processus d'activation thermique entraîne la réduction partielle de ZrO_2, la réduction totale de l'oxyde de Co et n'a aucune influence sur l'état des REM. Des études en fonction du temps et de la température montrent que la diffusion d'oxygène de la surface vers le volume est activée thermiquement avec une énergie d'activation de 0,21 ± 0,02 eV. L'exposition de la surface partiellement activée à O_2 à une pression de 10^{-5} Torr pendant 30 minutes a été trouvée suffisante pour saturer la surface, d'autre part l'exposition de N_2 n'a eu aucun impact sur la chimie de surface. Les espèces N-apparentées apparaissent seulement après des expositions à haute température du matériau, montrant la réactivité limitée du getter avec N_2. CO_2 conduit à la formation de monocouches de CO sur la surface du getter et à la diffusion de O_2- dans le volume du matériau. Ces résultats indiquent la réactivité élevée du getter avec des gaz contenant de l'oxygène, mais une réactivité plutôt limitée avec N_2. Un mécanisme de diffusion de l'oxygène vers le volume ainsi qu'un mécanisme de piégeage des gaz sont proposés. Les résultats donnent un nouvel aperçu des avantages et des limites du *getter* pour les applications MEMS.

ABSTRACT

Recently, there has been an increasing interest in vacuum maintenance and residual gases expulsion within small cavities in microelectromechanical systems (MEMS) and advanced field emission displays. Residual gases often poison the vacuum and eventually deteriorate device and system operation. In order to maintain vacuum in cavities, there are a few steps that must be implemented: i) a hermetic sealing of the cavity should be realized to minimize gas leakage from surrounding environment; ii) proper degassing of the system before seal-off is needed to dislodge and release trapped gases within the materials; and iii) if necessary incorporating a strip or a thin film of a reactive metal alloy which acts as a chemical pump to rid the system of residual gases during the device lifetime. Such alloys are known as getters, which contain active transition metals such as Zr, Ti, V, and Fe that spontaneously chemisorb active gases within cavities. To improve the gettering efficiency, a variety of material systems have been proposed and tested, and two characteristics appear to be critical: (1) morphology (surface area); and (2) composition (physical and/or chemical reactivity). Despites their technological importance little is known about the exact mechanisms of gas trapping within the material. This project tackles this very issue by using *in situ* studies to investigate the nature of bonding between the getter constituents and residual gases and the effect of the activation temperature on the surface composition and volatile molecules trapping.

Our studies focused on zirconium-cobalt-rare earth metal (REM) alloys which have been developed with a low activation temperature (<350^{o}C) for MEMS devices. Thin films of these alloys were sputtered on Si. The obtained films are highly porous, which is critical to lower the activation temperature. Scanning Electron Microscopy (SEM), X-ray Photoelectron Spectroscopy (XPS), Time of Flight Secondary Ion Mass Spectrometry (TOF-SIMS), and Time of Flight Elastic Recoil Detection (TOF-ERD) are utilized to examine the morphology and composition of both bulk and surface of the alloy. The surface evolution as a function of temperature is monitored *in situ* via XPS. This project elucidates the room temperature and high temperature reactivity of the material with O_2, N_2, and CO_2.

The results show that annealing at 350^{o}C only leads to a partial activation of the surface, with an onset at 200^{o}C. The thermal activation process results in the partial reduction of ZrO_2, full reduction of Co from its oxide state and has no influence on REM states. Time and temperature-dependent studies show that oxygen diffusion from surface to bulk is thermally activated with an

activation energy of 0.21±0.02 eV. Exposure of the partially activated surface to O_2 at a pressure of 10^{-5} Torr for 30 minutes was found to saturate the surface, on the other hand N_2 exposure was found to have no impact on the surface chemistry. N-related species were only apparent at high temperature exposures of the material, displaying the limited reactivity of the getter with N_2. CO_2 results in the formation of CO monolayer on the surface of the getter with the diffusion of O^{2-} to the bulk of material. These results indicate the high reactivity of the getter with oxygen-containing gases, but a rather limited reactivity with N_2. A mechanism of oxygen diffusion to the bulk as well as for trapping of gases are proposed. The results give new insights into the advantages and limitations of the material for MEMS applications.

TABLE OF CONTENTS

LIST OF TABLES

LIST OF FIGURES

LIST OF ABBREVIATIONS

ABBREVIATIONS

AES	Auger Electron Spectroscopy
BCC	Body Center Cubic
HCP	Hexagonal Close-Packed
NEG	Non-Evaporable Getter
SEM	Scanning Electron Microscope
TDS	Thermal Desorption Spectrometry
TOF-ERD	Time-of-Flight Elastic Recoil Detection
TOF-SIMS	Time-of-Flight Secondary Ion Mass Spectrometry
XPS	X-ray Photoelectron Spectroscopy
UHV	Ultra-High Vacuum

LIST OF APPENDICES

CHAPTER 1 INTRODUCTION

1.1 Context

Developing materials for gas trapping and storage is of utmost importance for several technologies including; clean energy applications[1], [2], noble gas separation[3], [4], carbon sequestration[5], [6], and removal of residual gases in vacuum cavities or chambers[7]–[10]. Such materials are very reactive and specifically designed with high porosity, nano- and micro-sized pores, to allow high gas sorption capacities[5], [11], [12]. Their functionality and gas selectivity can be tailored through material design and engineering for specific applications. Structural selectivity rises from the pore size distribution within the material that preferentially traps certain molecules. This behavior, which is governed by the steric effect, is known as "molecular sieving"[13]–[15]. "Quantum sieving" is a particular case of the molecular sieving effect, where the diameter of the pore is in the sub-nanometer range[14], [16]. Chemical selectivity, on the other hand, originates from the nature of interaction between impinging gas molecules and atoms present on the surface, which is governed by thermodynamics constraints[13]. Kinetics can also play an important role in selective interaction, where different gases have different diffusion rates depending on the adsorbent material[14], [15]. Materials designed for gas trapping include metal-organic frameworks[3], [11], [14], [17], carbon-based materials[5], [18], polymeric networks[5], [19], transition metal alloys[9], and alkaline earth metal alloys[8].

Transition and alkali earth metal alloys are used as getter materials for residual gas removal in vacuum chambers[9], [10], [20]. These materials are capable of sorbing a wide range of gases at room temperature. They are able to irreversibly trap O_2, N_2, H_2, CO, CO_2, H_2O, and hydrocarbons[20]. There are two main classifications of getter materials: evaporable (flashed), and non-evaporable (bulk getters). The former is composed of an alloy or pure metal (e.g. $BaAl_4$, Ti, Ni) in powder or bulk form, which is cyclically sublimated within the chamber, while the latter is deposited as a film of a few micrometers (<5 μm) in thickness and is often composed of transition metal alloys [20]–[22]. Flashed getters react with residual gases by sublimation (>1000°C) and condensation on the inner walls of the vacuum chamber[21], [23], [24]. On the other hand, bulk getters are deposited prior to forming the vacuum cavity and are then thermally activated (<500°C) to react with surrounding contaminants. Getters are used in sublimation pumps[23], ion pumps[25],

accelerators[26], and microelectromechanical systems (MEMS) vacuum packaged devices[8], [27]–[29].

Bulk getters were developed for vacuum chambers or cavities that are incompatible with the continuous evaporation of materials, and cannot withstand the high temperatures at which flashed getters are sublimated (>1000ºC)[8], [21], [27]. Bulk getters are often integrated in vacuum packaged MEMS devices for maintaining proper operating conditions for the lifetime of the device (10+ years)[29], [30]. The vacuum requirement varies depending on the application and ranges between 10^{-4}-225 Torr[27]. Considering a hermetically sealed cavity (i.e. no leakage), material outgassing would be the only source of pressure increase within MEMS cavities[31]. The material is generally sputter deposited on the cap wafer for wafer-level packaging prior to wafer bonding[27]. However, the material remains inactive due to the formation of an oxide layer on the surface upon exposure to ambient condition. The oxide acts as a passivation layer preventing further oxidation of the material and diffusion of gases to the bulk. Thus, the surface must be activated during or after formation of the microcavity. The activation process must also be compatible with the thermal budget required to maintain the device operation.

In order to activate the getter, the material is annealed to a critical temperature at which the oxide and other contaminants would diffuse into the bulk freeing up surface sites to interact with residual gases[21]. The activation temperature changes depending on the composition of the material, and can range between 200-400ºC[32]–[34]. The overall sorption capacity of the material is limited by the available surface area, which is dependent on the morphology of the thin film[26]. Bulk getters are mainly composed of zirconium due to its highly electropositive nature and innate ability to dissolve its own oxides, carbides, and nitrides upon annealing[35]–[37].

Despite their technological importance, to the best of our knowledge, no detailed study has been conducted on the kinetics and the underlying mechanisms of gas trapping and surface contaminant diffusion into the bulk of a Zr-Co-REM (rare earth metals) getter material. *in situ* X-ray photoelectron spectroscopy (XPS) has been utilized to study the activation process of various getter materials due to its high surface sensitivity[38]–[47]. Petti *et al.*[47] and Xu *et al.*[30] investigated the influence of annealing temperature up to 450ºC on the surface chemistry and microstructure from engineering and industrial perspectives. Petti *et al*. concluded that the Zr-Co-REM getter is activated at 300ºC by reducing the ZrO_2 species to its metallic form and a segregation

of Co towards the surface at 450ºC. On the other hand, Xu *et al*. examined the effect of annealing temperature on the microstructure, as well as the resistance of the getter to various wafer cleaning processes by examining the getter's sorption characteristics [30]. Despite the recent efforts in providing a complete study of the gettering properties of the Zr-Co-REM alloy, a rigorous study of the physical and chemical characteristics of the alloy are still missing. The studies also lack an examination of trapping of common residual gases within MEMS cavities, especially N_2, since many industrial processes are conducted in an N_2 environment, increasing the partial pressure of N_2 within cavities. Therefore, it is of utmost importance to understand and quantify the ability of the Zr-Co-REM getter of trapping N_2, along with other volatile molecules.

1.2 Thesis Objectives & Outline

The brief overview above highlights the importance of understanding the characteristics of getter materials at the micro- and nano-scale in order to improve material performance for targeted applications. This thesis focuses on understanding the mechanism in which gases are trapped in a Zr-Co-rare earth metal (REM) alloy based getter that has been recently developed for MEMS applications. The main objectives and addressed questions in this thesis are as follows:

- Elucidation of the influence of low temperature activation on the alloy surface chemistry.
- Investigations of the kinetics of oxygen diffusion from surface to bulk of the material.
- Qualitative and quantitative studies of the reactivity of the getter with O_2, N_2, and CO_2 molecules.

The thesis is organized in the following manner:

- Chapter 2 gives the scientific and technological background of the development of getters as well as the theoretical basis of their operation, their classifications, and specific examples from the broad spectrum of their applications.
- Chapter 3 describes the experimental techniques employed in this work, including XPS, TOF-SIMS, and TOF-ERD.

- Chapter 4 discusses the experimental results obtained from *in situ* XPS and *ex situ* TOF-SIMS and TOF-ERD studies of the getter activation and reactivity (manuscript submitted to Journal of Physical Chemistry)
- Chapter 5 summarizes the important findings and identifies key points that need to be addressed in future projects.

CHAPTER 2 CRITICAL REVIEW OF THE LITERATURE

2.1 Getter

Getter is a term that describes materials that are capable of chemically absorbing (sorbing) active gases. In the late 19th century, Malignani, Thomas Edison's assistant, used the term "getter" to describe red phosphorous in incandescent lamps [36], [48]. Red phosphorous was used to prevent the blackening of incandescent lamps, which was due to the deposition of tungsten oxide on the inner walls of the lamp. Tungsten oxide forms as a result of tungsten evaporation from the hot filament and its reaction with residual water vapor within the bulb [49]. Evaporation of tungsten from the hot filament is known as thermionic emission or Edison effect, and efforts to prevent this phenomenon have led to the development of vacuum tubes [48]. The integration of phosphorous as a getter was able to reduce the level of water vapor within incandescent lamps, and therefore increase the lifetime of the bulbs. Then, in the early 1900s, with the development of electron tubes, great effort was put into increasing their lifetimes. After the Second World War, a study was conducted on the causes of failure in electron tubes and it was found that poor vacuum was the main culprit. Barium (Ba) was then incorporated in an effort to maintain vacuum within the tube. The result was a dramatic increase in the lifetime of the tube to tens of thousands of hours (500% increase) [48].

Commercialized getters were developed by SAES Getters S.p.A.. and Telefunken companies in Italy and Germany in the late 1940's and early 1950's [50]. Getters are composed of materials that naturally allow for the adsorption, absorption, and dissociation of gases. They are widely utilized in vacuum systems in order to either improve or maintain a level of vacuum, or to purify inert gases within a particular system. They are capable of irreversibly trapping reactive gases such as O_2, H_2, N_2, CO_2, CO, H_2O, and hydrocarbons, but not noble gases [21], [24], [51], [52]. Getter materials are able to produce stable solid compounds by chemically reacting with residual gases forming oxides, nitrides, carbides, hydroxides, and hydrides [21]. Getters are increasingly utilized in many applications including but not limited to the following; particle accelerators for extreme high vacuum [33], lighting applications [53], vacuum microcavities in MEMS [8], [36], [54], [55],

flat-panel displays [22], ultrahigh vacuum systems [24], [51], [56], and inert gas purification [45], [57].

In the following sections, the different types of getters, the principles of their operation, and the materials used for gettering will be discussed.

2.1.1 Classification

The first class of getter material developed, which was briefly mentioned earlier, was Ba for electron tubes and cathode ray tubes. Ba-based getters were initially used as pure metal in bulk form. However, they were unstable due to the high reactivity of Ba with water vapor and O_2 rendering it unstable and difficult to handle. In the early 1950's della Porta of SAES group in Italy solved this issue by alloying Ba with aluminum (Al), $BaAl_4$, allowing the material to pump for increasingly longer hours while being more easily handled [21], [36]. Ba alloy is part of the class of getters that are used for high temperature applications, where the material is heated to substantially high temperatures (>1000^{o}C). The heat treatment results in the evaporation of the material, which would then react with residual gases and condensate on the inner walls of the chamber as a thin film. Today, titanium (Ti) sublimation pumps operate on the same concept [23], [58], [59]. This class of materials is known as evaporable (flashed) getters [21], [50]. The evaporation cycle can be repeated many times during the lifetime of the device or chamber to maintain proper operating conditions [21]. Due to the volatile nature of evaporable getters and the high temperatures at which they are sublimated, another class of materials was developed in the late 1950's known as non-evaporable getters [60]. These materials are deposited as thin films prior to the formation of the vacuum cavity or chamber and operate at much lower temperatures (<700^{o}C) [21], [50], [60]. Recent progress in developing different materials for non-evaporable getters has sparked a surge of studies to elucidate their principles of operation, which will be briefly discussed in the following section.

2.1.2 Gettering Principle of Operation

2.1.2.1 Activation Process

For Ba evaporable getter, the $BaAl_4$ alloy is mixed with a nickel (Ni) powder and compressed into a disk vessel. The getter container is placed into the vacuum system and is heated via a radio frequency (RF) coil up to 800^{o}C inducing a highly exothermic reaction releasing Ba atoms and forming NiAl alloy. The exothermic reaction increases the temperature of the material up to 1200^{o}C, which sublimates Ba into the tube. As Ba is evaporated it chemically reacts with active residual gases within the vacuum tube or chamber and condenses on a collecting surface as a thin film [20]. Inert gases cannot be gettered, and therefore they must be eliminated prior to sealing of the vacuum tubes to maintain a low operating pressure. Other materials that have been used as flash or evaporable getters include strontium, calcium, and titanium [23], [59], [61]–[64].

Non-evaporable getters come in the form of powdered metals or alloys, or deposited thin films of a few micrometers in thickness. In the case of powders, they are painted inside the vacuum tubes as a paste or sintered and formed into strips or other geometries. On the other hand, thin films are directly sputtered on an appropriate substrate and loaded inside the chamber [65], [66]. Since these materials are deposited *ex situ* a passivating oxide layer forms on the surface of the material upon exposure to air, preventing its possible reaction with residual gases within the system. The passivating layer acts as a barrier for gases to further diffuse into the bulk of the material, protecting the bulk of the material from oxidation. However, since the material is capped by a passivating layer, it must be activated once a certain level of vacuum is achieved within the chamber or device. The activation process is often achieved by annealing the material *in situ*, driving the surface contaminants to the bulk of the material through a diffusion process as shown in the schematic below (Figure 2.1) [21]. The diffusion process of different contaminants (e.g. C, O, N) depends on the solubility of the contaminants in the material from which the getter is composed [13]. Thus the onset of activation temperature and the degree of activation is defined by the basic constituents of the getter material, the getter morphology, as well as the crystalline nature of the getter [5], [12]. The performance of the non-evaporable getter material is also defined by a number of different variables which will be discussed below.

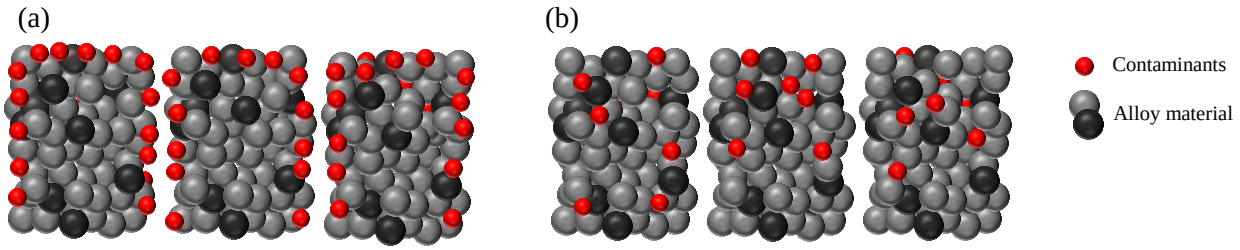

Figure 2.1: Schematic representation of the thermal activation process for non-evaporable getter alloy. (a) Shows the grains of the alloy material, with a passivating layer of contaminants encapsulating the entire surface of the material (red spheres) l. (b) Annealing the alloy to a critical activation temperature allows for surface contamination to diffuse to the bulk of the material freeing up surface sites for subsequent gettering.

2.1.2.2 Performance-limiting factors

There are multiple variables that define the performance of a getter. First, macroscopically, the sorption capacity and gettering rate can be determined by sorption measurement. A typical sorption measurement set-up is composed of two chambers, where the gas is introduced in one chamber and leaked through a small opening into the second chamber where the sample is held. The pressure difference between the chambers is measured using ion gauges. The RGA (residual gas analysis) method is often used to measure the partial pressures of constituent gases [67]. The important macroscopic parameters deduced from the sorption measurements are the pumping speed and the sorption capacity. First, the pumping speed, given by units of cm^3/s, represents the volume of gas that the material is capable of absorbing in 1 second, while the sorption capacity is the total amount of gas the getter is able to absorb, and is given by units of pressure × volume. The macroscopic properties of a getter are governed by the molecular interaction between the gas molecules and the surface. Therefore, it is important to discuss the molecular-level parameters that play an important role in determining the macroscopic characteristics of a getter.

Microscopically, the material performance is dependent on the kinetics of surface-gas interaction, and bulk diffusion of trapped species [68]. The kinetics entails first the adsorption of the gas species on the surface, followed by either desorption or surface reaction, and then diffusion of the species [68], [69]. The probability of a reaction to occur between an adsorbed gas molecule and the surface, i.e. chemisorption, is dependent on the sticking coefficient and the free energy of

the molecule-surface interaction. The sticking probability is defined as the probability for an impinging gas molecule to adsorb on the surface for a finite interval of time rather than be instantaneously reflected off the surface into the gas phase [69]. The sticking probability (*S*) is inversely proportional to the impingement rate (*v*) and directly proportional to the rate of adsorption. The impingement rate is given by [69]

$$v = \frac{P}{\sqrt{2\pi mkT}} \ (cm^{-2}s^{-1}) \tag{2.1}$$

where *P* is the pressure, *m* is the mass of a single molecule for a given gas, *k* is the Boltzmann constant, and *T* is the temperature of the gas. The sticking probability is also dependent on the adsorbate coverage of the surface. Initially, with low surface coverage, the sticking probability is constant, but rapidly diminishes with increasing coverage values. The sticking probability varies as a function of temperature; lower temperatures are coupled with a decrease in the thermal desorption rate, and as a result higher surface coverages are achieved [69], [70].

An adsorbate can either weakly or strongly interact with a surface. Weak interaction is in the form of van der Waals forces, where a molecule can either occupy a single adsorption site or two neighboring sites depending on its orientation on the surface. On the other hand, if a molecule chemisorbs on the surface, both atoms would form strong covalent bonds on adjacent adsorption sites, and the bond between the two atoms is broken. This is assuming the diatomic molecule is symmetric in the form of X_2 (X=H, O, N) [69]. CO molecules can also chemisorb on certain metal surfaces, however, the bond between C and O is not broken, therefore CO occupies a single adsorption site [71]. Bond cleavage, which occurs during chemisorption, is dependent on the strength of the M-X bond, where M is metal surface atom, and X is the gas atom. If the M-X bond is larger than or equal to half of X-X bond, then X_2 molecule would break and two M-X bonds would form [69]. It is worth noting that the nature of H_2 bonding with materials is peculiar. H_2 can be trapped molecularly or chemisorb depending on the nature of interaction between the molecule and atoms on the surface. Moreover, in non-evaporable getters, H_2 molecules tend to desorb from the material upon annealing, but are recaptured by the material when cooled down [72]. The bonding nature of the gas with the surface is dependent on the free energy, which is sensitive to the electronic structure of the surface and the availability of electrons for bonding. Chemisorption is often coupled with a negative change in enthalpy ($\Delta H < 0$), meaning the reaction is exothermic.

As a result, the free energy of formation of the new bond is also negative ($\Delta G < 0$). Thermodynamically, the reaction is favorable since the overall free energy of the surface is reduced. The free energy of formation is described by the Gibbs-Helmholtz relationship,

$$\Delta G = \Delta H - T\Delta S \tag{2.2}$$

such that ΔS is the difference between the final and initial entropy states. Since ΔS is negative after the adsorption/chemisorption of a gas molecule on a surface, due to the decrease in rotational and translational degrees of freedom, then ΔH must be negative in order to reduce the overall free energy of formation. The surface electronic structure determines whether the surface is able to covalently bond with an adsorbate or not. The outer energy bands of the material must have unpaired electrons that would participate in bonding. If the energy bands are completely filled with electrons the surface is rendered inert, as with noble metals [69]. Transition metals have partially filled *d*-orbitals increasing their surface activity in the presence of ambient gases [73]. Transition metals often have at least two unpaired electrons in their outer *d*-orbital. Since transition metals have surfaces with electronic structures that favor surface reactions, then they are ideal candidates for gas trapping and absorption.

Other variables that govern the pumping properties of a getter is the rate of gas diffusion from the surface of the material to the bulk and available surface area. Annealing at sufficiently high temperature was found to prompt surface contaminants to diffusion into the bulk [62], [74], [75]. Thus, choosing the right material (alloy) allows for optimizing the material for specific gettering applications. In the following section, a review of the different metals and metal alloys utilized for non-evaporable getter materials will be discussed.

2.1.3 Current Status of Getter

Since the initial discovery of non-evaporable getters, there has been great progress in the development of materials, as well as in the techniques used for fabricating non-evaporable getters. Table 2.1 summarizes some of the important literature that has been published since the early 1970's until 2016, on the different materials, their preparation, and the targeted application (when listed). A large number of studies, which are not included in this list, are more focused on examining the pumping properties using sorption measurements, for different gases and at different operating temperatures. However, since the focus of this thesis is on understanding the mechanisms

of gas trapping within the getter on a molecular level, such studies were not included in this list. Looking at the range of materials used in the literature, one common denominator in the alloys developed is zirconium (Zr). Zr is a transition metal with 4 valence electrons, and an electronegativity of 1.33, therefore it has a high affinity for oxygen which diffuses readily into Zr-based oxides, nitrides, and carbides upon annealing [35], [76]. The surface properties and chemistry of Zr will be discussed in further detail in section 2.2.

There are certain requirements that must be satisfied for developing new non-evaporable getter materials for specific applications. First, an appropriate selection of the substrate is critical such that the getter thin film must exhibit good adhesion properties after deposition. Second, the activation temperature must be compatible with the targeted application, which can be tuned by changing the composition and the morphology of the thin film. Third, the constituents of the material must also have a relatively high oxygen affinity and solubility (>10%), to allow for multiple activation cycles [38]. These are general guidelines for material development for various applications, specific requirements such as high hydrogen or nitrogen capacity can be accommodated through material design and engineering [12], [14], [38], [60]. Many studies have examined the effect of thermal activation process on the surface composition of different getter alloys using surface sensitive techniques such as Auger electron spectroscopy (AES) [32], [62], [77], [78] and X-ray photoelectron spectroscopy (XPS) [34], [41], [43], [46], [79]. A few studies have also utilized secondary ion mass spectroscopy (SIMS), elastic recoil detection (ERD), X-ray diffraction (XRD), and other bulk techniques to characterize the change in bulk composition of the material (ERD, SIMS), and in crystalline phases of materials (XRD) as a function of temperature and reactivity with different gases [80]–[85].

2.1.3.1 Non-Evaporable Getter: Deposition & Influence on Morphology

As shown in Table 2.1, the preparation of getter material can be achieved by either ball-milling, e-beam evaporation, or magnetron sputtering, depending on the application. For more recent non-evaporable getters (NEG), magnetron sputtering is usually the more favored technique, since it allows for alloying of materials easily, as well as the control over the structure and composition of the deposited thin film by optimizing deposition parameters. In magnetron sputtering, substrate temperature, deposition pressure, substrate material and structure, and flow of sputtering gas have a significant impact on the microstructure of the deposited thin film, which influence the gettering

properties of the thin film. Benvenuti, *et al*. [86] studied the effect of substrate temperature on the microstructure of a Ti-Zr-V thin film. Ti-Zr-V thin films were deposited for particle accelerator applications, where the getter must be activated at temperatures lower than 200^{o}C for aluminum-based chambers. In their study, they varied the substrate temperature from 100 to 350^{o}C, and found that 250^{o}C was the optimal temperature for achieving highly porous thin films. The porosity of the thin film is coupled with the presence of columnar structures in the cross-section of the thin film, which act as channels for the diffusion of contaminant species from the surface to the bulk of the material. The activation temperature of the thin film deposited at a substrate temperature of 250^{o}C was found to be 180^{o}C, compatible with aluminum chambers for particle accelerators [86]. Malyshev, *et al*. [87] showed that higher sputtering pressure increases the roughness of the thin film and introduces a larger distribution of columnar structure for Ti-Zr-V thin films. Other studies investigated the effect of glancing angle between substrate surface and target on morphology of Ti-Zr-V [88], pressure and substrate temperature on morphology and sorption properties of Zr-Co-Ce getters [89]. This is as far as getter morphology and thin film composition, as mentioned in the previous section, influence the activation temperature and efficiency of contaminant bulk diffusion.

Table 2.1: List of non-evaporable getter materials examined in the literature, the deposition technique, their activation temperature, and the targeted application.

Material	**Deposition Technique**	**Activation Temperature**	**Application**	**Reference**
Ti capped with Au	Magnetron sputtered	380-415^{o}C	MEMS	[90]
Ti capped with Ni, Au	e-beam evaporation	300^{o}C	MEMS	[91]
Ti capped with Cr, Pt	e-beam evaporation	200-400^{o}C	N.A.	[92]
TiZrV	Magnetron sputtered	<300^{o}C	Particle accelerators	[32], [77], [81], [83], [85], [88], [93]–[100]
TiHf, TiZr, TiZrV, HfZr	Magnetron sputtered	<400^{o}C	Particle accelerators	[33]
Ti-Mo	Sintered powders or magnetron sputtered	400-750^{o}C	N.A.	[101], [102]
$Zr(V_xFe_{1-x})_2$ $ZrMn_2$, TiFe	Radio frequency melting	<430^{o}C	N.A.	[43]

Zr, Ti, Mn				
ZrVFe	Powder	<600°C	N.A.	[80]
$Zr(VFe)_2$	Powder	N.A.	N.A.	[103]
Zr_2Fe	Powder	N.A.	N.A.	[104]
Zr_2Fe, ZrVFe	Arc melted ingot	400-800°C	N.A.	[45], [57], [105]
ZrV	Magnetron sputtered	<320°C	Particle accelerators	[39], [41], [106], [107]
ZrV, ZrCo, ZrTi	Magnetron sputtered	<350°C	N.A.	[108]
ZrAl, ZrNi, ZrVFe	N.A.	<800°C	N.A.	[34]
ZrCo with Ni cap	Arc melted		H_2 storage	[109]
ZrCoCe ZrCoREM	Magnetron sputtered	<330°C	MEMS	[30], [47], [89], [110]
ZrCoREM	Powder	<330°C	N.A.	[111]
ZrFe	Arc melted	500°C	N.A.	[78]
ZrFeV with Pd cap	Arc melted	550°C	H_2 storage	[112]
ZrTiV	Electromagnetic induction melting	260°C	H_2 storage	[44]
ZrVFe	Magnetron sputtered	<700	Accelerator	[46], [72], [79], [113], [114]
	Rf melted	<380	MEMS	[115]
Zr-$Zr(VFe)_2$	Powder	N.A.	N.A.	[116]

2.1.3.2 NEG Alloying Effects

Mašek, *et al.* [41] investigated the effect of varying Zr-V alloy composition on the activation temperature of the getter. They used intertwined wires as the target material for magnetron sputtering, and by changing the number of wires used of each metal, the film composition was

altered. During the *in situ* activation process which was monitored using XPS, it was shown that higher V content led to a lower activation temperature (220^{o}C). The activation process is often monitored by tracking the level of oxygen and oxygen-related species on the surface of the material [34]. Mašek, *et al*. found that V_xO_y tends to be the first species to be reduced to metallic state, and more efficiently than ZrO_2, by heating the samples to 220^{o}C for 2 hours under ultra-high vacuum (UHV). By varying the V content (34%, 54%, and 72%), they found that very high V content is coupled with a decrease in the rate of the activation process, and the optimal composition was found to be 54% V. However, despite increasing the temperature to 320^{o}C, the surface still contained sub-oxide species. The thermal treatment also showed that Zr is more actively reacting with other constituents of the passivation layer, such as H_2O and hydrocarbons, where carbide and hydroxide species are formed upon annealing. On the other hand, V only seemed to be reactive with O_2 [41]. From their study, it appears that Zr has a higher affinity to contaminants compared to V, which leads to the slower activation process of Zr compared to that of V. The authors did not investigate or discuss the underlying causes of different behavior of V and Zr in the thin film, however one can deduce the following based on their observations. When V content was increased to 72%, the activation process was found to significantly decrease, i.e. higher O content was retained on the surface, which indicates that a sufficient amount of Zr in the matrix facilitates the reduction process. Moreover, Zr and V have an electronegativity of 1.33 and 1.63, respectively, indicating that Zr has a higher affinity to O, which assists in the diffusion process of O to the bulk of the material [76]. The enthalpy change for the oxide and carbide formation for Zr is more negative than V. Consequently, it is more thermodynamically favorable for Zr than for V to stay in the oxide state during the activation process [34]. Thus, by achieving a balance between the two elements, one can attain a low activation temperature getter.

Similar behavior was observed in TiFe alloys, where Fe was completely reduced to metallic phase at 357^{o}C while Ti remained oxidized [43]. Meli, *et al*. [43] compared the behavior of TiFe alloy upon annealing to 357^{o}C to that of pure Ti, and found that in pure Ti, the metallic phase is fully recovered after subjecting Ti to the same annealing conditions. These observations indicate that during the annealing process, both Ti and Fe oxide phases are decomposed, but the oxygen from Fe can be recaptured by Ti, due to the difference in electronegativity (Ti: 1.54, Fe: 1.83) resulting in the fast and complete reduction of Fe_xO_y to Fe^0 assisted by Ti oxidation [43], [76]. Again, following the same trend, the enthalpy change and the free energy of formation of oxide

and carbide for Ti is significantly lower than that of Fe [34]. Thus, alloying has a significant effect on the activation temperature and the pumping properties of a getter material. Alloying increases the number of defects and grain boundaries in the material, which can significantly reduce the activation temperature and increase the surface area. By varying the alloy composition and optimizing the deposition process, nanocrystalline grains with sizes that range between 3-5 nm can be formed increasing the number of grain boundaries and therefore facilitating the diffusion of the passivation layer to the bulk [32].

Analytical models based on Fick's law have been developed to describe the gettering mechanisms, however the studies targeted dense polycrystalline rather than porous materials [52], [68]. Therefore, there is a still gap in the fundamental understanding of the trapping and diffusion of contaminant species in porous materials. A quantitative and predictive models would take into account microstructural contribution to the activation and gettering properties of various materials. Where diffusion through the material is governed by Fick's law only through the grains, in contrast the diffusion through the pores would be considered more surface diffusion.

2.1.3.3 Recent NEG Material

The more recently developed getter materials for MEMS applications is a Zr-Co-rare earth metals (REM) alloy, with a relatively low activation temperature at 300^{o}C, compatible with the temperature-sensitive nature of MEMS devices [47], [110]. The material is nanoporous and composed of nanocrystalline grains that substantially increase its surface area. Xu, *et al*. [89] investigated the effects of magnetron sputter deposition pressure and substrate temperature on the microstructure and hydrogen sorption properties of a Zr-Co-Ce thin film. The target material is an alloy of 76.2:20.7:3.1 (atomic%) of Zr:Co:Ce. The deposition pressure and Si substrate temperature were varied from 1-60 mTorr and 25-300^{o}C, respectively. Their results show that lower deposition pressures produced denser thin films with poor getter characteristics. In contrast, high sorption properties were obtained at substrate temperature of 150^{o}C coupled with a high specific surface area as measured by Brunauer–Emmett–Teller (BET) [89]. The sputter deposition parameters affect the mobility of adatoms on the surface of the substrate, and the microstructure can be predicted using the structure zone model [117]. In a separate study, Xu, *et al.* [30] examined the effects of activation temperature on the microstructure of a Zr-Co-Ce getter, as well as the stability of the material to different cleaning processes. They investigated the material's thermal behavior

in the range of 250-400^{o}C. They concluded that high sorption capacity is achieved with an annealing cycle at 300^{o}C for 30 minutes. Scanning electron microscopy (SEM) analysis demonstrated a slight change in the microstructure of the thin film as a function of temperature. They observed a growth in the nanocrystalline grains with increasing temperature and increase in the crystallization, however they did not provide detailed analysis regarding the nature of the evolving nanocrystals [30].

As shown in the previous sections, Zr is the most common component of NEGs, thus reviewing the structure, chemistry, and reactivity of pure Zr with gases is an important step in understanding the mechanisms of gas trapping within NEGs.

2.2 Zr: Chemistry, Reactivity, & Applications

Zr has a wide range of industrial applications. One of the earliest uses for Zr is in the nuclear reactor industry, due to its low neutron absorption [37], [118], [119]. Moreover, because of Zr's high chemical reactivity with gases, it is one of the most used metals in the development of non-evaporable getters. Zr alloys have been utilized for a number of applications; ZrCo alloy for tritium storage and handling [120], variety of Zr-alloys for getter applications (as shown in Table 2.1), zirconia for dental application [121], [122], and ZrN and ZrC for machining and cutting tools [123]. Zr is an abundant metal representing 0.017% of the lithosphere, similar to carbon concentration [37]. Due to its highly reactive nature, it is not present as a pure metal, but rather as an oxide, ZrO_2. High purity Zr has two phases, α-Zr (HCP) and β-Zr (BCC) stable below and above 860^{o}C, respectively. Pure Zr can only be prepared under vacuum or inert conditions, especially in the absence of oxygen, nitrogen, hydrogen, and carbon, which are readily absorbed by Zr. In order to obtain a pure metal, a reducing agent must be added to reduce ZrO_2 to metallic form. Reducing agents can be in the form of Mg, Al, or Ca, which have higher O affinities than that of Zr. Zr is able to dissolve up to 29 atomic % and 20 atomic % of oxygen and nitrogen, respectively, in its lattice at increased temperatures, without the separation of a ZrO_2 phase. On the other hand, ZrC phase forms and separates readily after the incorporation of 1 atomic% of carbon [37]. Zr surface reactivity arises from the fact that the metal has two unpaired electrons in its outer *4d*-orbital, and has four valence electrons. Its atomic mass is 40 and thus its electron configuration is [Kr] 4d2 5s2 [37]. Moreover, Zr one of the more electropositive transition metals, with an electronegativity of

1.33, thus not only it reacts with surrounding oxygen, it can also reduce other metal oxides granted the metals are more electronegative than Zr [37], [76].

When the metal is purified and exposed to ambient atmosphere, a passivation layer of oxide forms on the surface, which prevents the bulk of the material of interacting with other gases. Therefore, the oxide layer forms as both a diffusion barrier and as a corrosion-resistive layer [118]. When the metal is subjected to annealing at 250^{o}C, it is found to slowly react with surrounding hydrogen. Heating Zr under UHV up to 500^{o}C, allows for the passivation layer constituents to diffuse to the bulk of material rendering the surface of the metal active to interact with surrounding gases. In terms of hydrogen, Zr can rapidly solubilize a hydrogen molecule at 150^{o}C as an interstitial hydride compound. Absorbed hydrogen shows a hysteresis phenomenon, where hydrogen can be reversibly absorbed and desorbed depending on the temperature at which the metal is annealed [37], [118], [124]. Hydrogen absorption results in the embrittlement of the metal, however, hydrogen can be expelled from the material by annealing the metal under vacuum at high temperatures [37]. It can also readily react and diffuse oxygen, carbon, nitrogen, and other oxygen-containing gases [35], [37], [125], [126]. Rate of nitrogen diffusion in Zr is lower than that of oxygen, but increases with increasing temperatures, especially beyond the $\alpha - \beta$ phase transition [37]. Zr's reactivity with different gases has been extensively investigated using surface sensitive techniques such as *in situ* AES and XPS. Many studies have been conducted on its reactivity with oxygen [35], [125]–[132], hydrogen [130], [131], [133]–[135], deuterium [35], carbon monoxide [35], [125], [126], hydrocarbons [136], [137], and nitrogen [35], [125], [126], [138], [139].

CHAPTER 3 EXPERIMENTAL TECHNIQUES

As discussed in the previous chapter, gettering reactions occur on the surface of the material and therefore it is important to examine the surface chemistry and how it evolves during the thermal activation process as well as in the presence of contaminating gases. The most common technique for analyzing surfaces for chemical composition and bonding is X-ray Photoelectron Spectroscopy (XPS). One important characteristic of certain XPS systems is *in situ* annealing capabilities, which allows for monitoring the evolution of surface composition during the thermal activation process of non-evaporable getters. It is also important to characterize the distribution of the contaminants within the bulk of the material through depth-resolved analysis. Time of Flight Secondary Ion Mass Spectrometry and Time of Flight Elastic Recoil Detection are qualitative and quantitative material science techniques that are used for in-depth analysis of chemical composition. This chapter will briefly discuss the theory on which these techniques are based.

3.1 X-ray Photoelectron Spectroscopy

3.1.1 Overview

The photoelectric effect was discovered by Hertz in 1887 during his attempts to experimentally validate Maxwell's equations. Many studies followed Hertz's observations in attempt to explain the phenomenon. However, it was not until 1905 that Einstein explained that high energy, low intensity electromagnetic radiation would induce electron emission from metal surfaces. Einstein described the energy of a photon using Planck's constant and the frequency of the photon for which he won the Nobel Prize in 1921. After the discovery and experimental confirmation of the phenomenon, scientists attempted to exploit the photoelectric effect for spectroscopic methods. Nevertheless, the lack of high vacuum systems and electronics to support it rendered the development of spectroscopic techniques difficult. It wasn't until 1950's that a spectroscopic technique was developed to detect photoelectrons by Kai Siegbahn in Sweden. The first ESCA (electron spectroscopy for chemical analysis) spectrum was produced in 1955. Siegbahn was awarded a Nobel Prize in physics in 1981 for his development of the ESCA technique [140]–[144].

3.1.2 Set up & Theoretical background

ESCA, or what is known today as X-ray photoelectron spectroscopy (XPS), is a surface analysis technique that provides information about the chemical composition and bonding nature of atoms of surfaces. A conventional XPS set up is displayed in a schematic in Figure 3.1. It consists of an X-ray source, a concentric hemispherical electron analyzer, and a detector. Samples are irradiated with soft X-rays of energies 1.2-1.5 keV, which results in the emission of core-level photoelectrons with kinetic energy *KE*. The emitted photoelectrons are focused and directed to an electron analyzer by means of electrostatic lenses and are deflected according to their kinetic energy [145]. *KE* of the photoelectron is dependent on the energy of the incident X-ray photon ($h\nu$), the binding energy of the photoelectron (*BE*), and the work function of the spectrometer (ϕ). *KE* is given by the following equation,

$$KE = h\nu - BE - \phi \tag{3.1}$$

Where *h* is Planck's constant and *v* is the frequency of the impinging photons. The binding energy is given by the energy difference of the material's Fermi level (E_F) and the core energy level from which the photoelectron was ejected (Figure 3.1). All elements of the periodic table can be detected using this technique, except for hydrogen and helium. Hydrogen cannot be detected because the hydrogen atom has a single valence electron and an extremely small photoionization cross-section. Therefore, if hydrogen is present in the material and it is ionized due to absorption of high energy X-rays, then the hydrogen signal would overlap with valence electrons ejected from other atoms within the material at very low binding energy (<20 eV) [146]. The *KE* given by the equation above assumes that the photoelectron emission process is elastic. If the photoelectron suffers energy loss (i.e. inelastic emission) this would give rise to a stepped background as marked in Figure 3.2. Conventional XPS uses either Al $K\alpha$, Mg $K\alpha$, or Zr $M\zeta$ with photon energies of 1486.3 eV, 1253.6 eV, and 151.4 eV respectively [142], [145]. X-rays of this energy can penetrate a few micrometers in depth of a solid, however the probed depth by XPS is typically on the order of a few nanometers. The surface sensitivity of XPS rises from the fact that photoelectrons have an inelastic mean free path (IMFP) on the order of 0.3-5 nm [147]. Therefore, photoelectrons that are emitted from deep within the material (i.e. beyond 10 nm) experience inelastic collisions with atoms or other electrons that dissipate their *KE*. Due to the electron's small IMFP, XPS measurements must be carried out under ultra-high vacuum in pressures below 10^{-9} Torr, to minimize energy loss of photoelectrons

with gas molecules. The XPS probing depth therefore depends on the IMFP, such that 95% of the signal comes from a depth equivalent to $3\lambda_i$, where λ_i is IMFP of the photoelectron. The probing depth, also referred to as escape depth, is given by the following equation

$$d = 3\lambda_i \cos\theta \tag{3.2}$$

where d is the probing depth and θ is the photoelectron take-off angle with respect to the surface normal [145]. By changing the take-off angle, the sampling depth can be varied, and information regarding uppermost monolayers can be deduced. However, the sample surface must have minimal roughness, since roughness and grains lead to shadowing effects [145]. Today, the attenuation length of photoelectrons through a material is used as a more comprehensive parameter instead of the IMFP. The attenuation length is defined as the transparency of a solid material to an electron, i.e. how far an electron can travel through a specific solid material experiencing minimal energy losses. One must distinguish IMFP from the attenuation length of electrons, such that the former is defined as the average distance between inelastic collisions [144], [148]. Recently, a more comprehensive parameter has been introduced, known as the effective attenuation length, which takes into account both elastic and inelastic collisions [144].

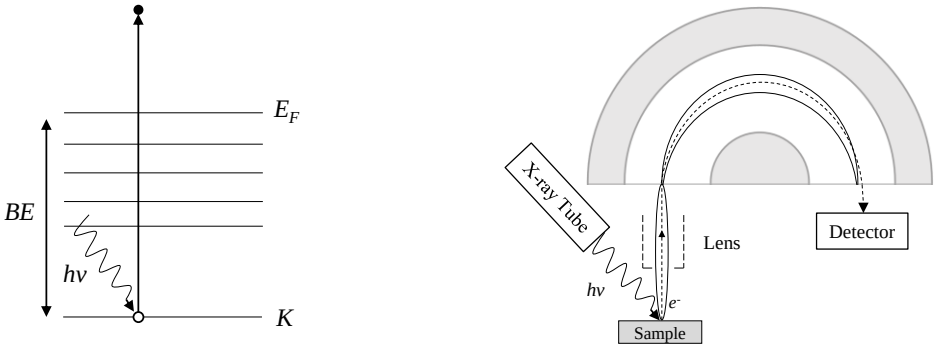

Figure 3.1: (Left) Energy band diagram representation of the photoelectric emission process. A core level electron absorbs a photon of energy *hv*, resulting in the emission of the photoelectron with kinetic energy *KE*. (adapted from [142]) (Right) Schematic representation of a conventional XPS set up, presenting the X-ray source, the sample, electron analyzer and the detector. (reproduced from [151]).

Attenuation lengths are approximated both theoretically and experimentally using over-layer experiments. Approximations are made regarding the over-layer, such that the surface is considered to have minimal roughness. Therefore, the estimated values prior to the development

of accurate techniques to measure thin film thickness and roughness such as atomic force microscopy generally have large errors (50% or more) [148]. The effective attenuation length, λ_{AL}, is approximated using the following equation,

$$\lambda_{AL} = \lambda_i\left(1 - 0.028\sqrt{Z}\right)(0.501 + 0.068\ln(KE)) \tag{3.3}$$

where *Z* is the atomic number, and *KE* is the kinetic energy of the electron [144]. A comprehensive database of the electron effective attenuation length is given by NIST, the National Institute of Standards and Technology [149]. In a specific system where there is an over-layer involved, the theoretical approximations would not be representative of the actual attenuation length of the photoelectrons. Experimentally, from XPS intensity variation, the signal intensities must be taken into account according to the following equation,

$$\frac{I}{I^{\infty}} = 1 - \exp\left(-\frac{t}{\lambda_i \cos\theta}\right) \tag{3.4}$$

$$\frac{I_s}{I_s^0} = \exp\left(-\frac{t}{\lambda_i^s \cos\theta}\right) \tag{3.5}$$

Such that I/I^{∞} is the ratio of the intensities from the over-layer to the intensity of a thick over-layer, while I_s/I_s^0 is the ratio of intensities for the signal from the covered substrate to the bare substrate, and λ_i, and λ_i^s are the IMFP of the photoelectrons from the over-layer and the substrate, respectively [148]. The two equations above depend on prior knowledge of the over-layer thickness (*t*). Thus, a more practical approach to approximating the effective attenuation length (λ_{AL}) was developed in 1997 by Cumpson and Seah [150] which takes into account material properties. The effective attenuation length developed by Cumpson and Seah is given by,

$$\lambda_{AL}(nm) = 0.31\left[10^9\left(\frac{M}{\rho n_M NA}\right)^{1/3}\right]^{3/2}\left[\frac{KE}{Z^{0.45}(\ln(KE/27) + 3)} + 4\right] \tag{3.6}$$

The first half of the equation takes into account properties of the material such as molar mass *M* (*kg/kmol*), density ρ (*kg/m*^{3}), n_M number of atoms in a molecule, and Avogadro's number (*NA* in *kmol*$^{-1}$), while the second part considers the kinetic energy of the photoelectron emitted from an

atom with mass *Z* [144], [150]. A detailed discussion on the more recent progress in estimating the attenuation length is given by Jablonski and Powell [148], [149]. Therefore, in order to have a better approximation of the probing depth, instead of using the IMFP in equation (3.2), it is substituted by λ_{AL} from equation (3.6).

3.1.3 Spectral shape & Quantification

XPS spectra are plotted as intensity, number of counts of photoelectrons per second, as a function of *BE*. Sharp peaks emerge at specific electron binding energies that are signatures for their respective atomic species, thus XPS gives information regarding the chemical composition of the surface [151]. The *BE* of a photoelectron represents the Coulombic attraction of the electron to the nucleus, which can be screened by the interaction of other electrons with the nucleus within the atom. Therefore, any type of chemical bonding (covalent, ionic) or van der Waals interaction between the atom and its surroundings results in the deformation of the electron density, thus changing the *BE* of the photoelectron [151]. As a result, XPS can provides information not only on the chemical composition of the surface, but also the nature of bonding between atoms.

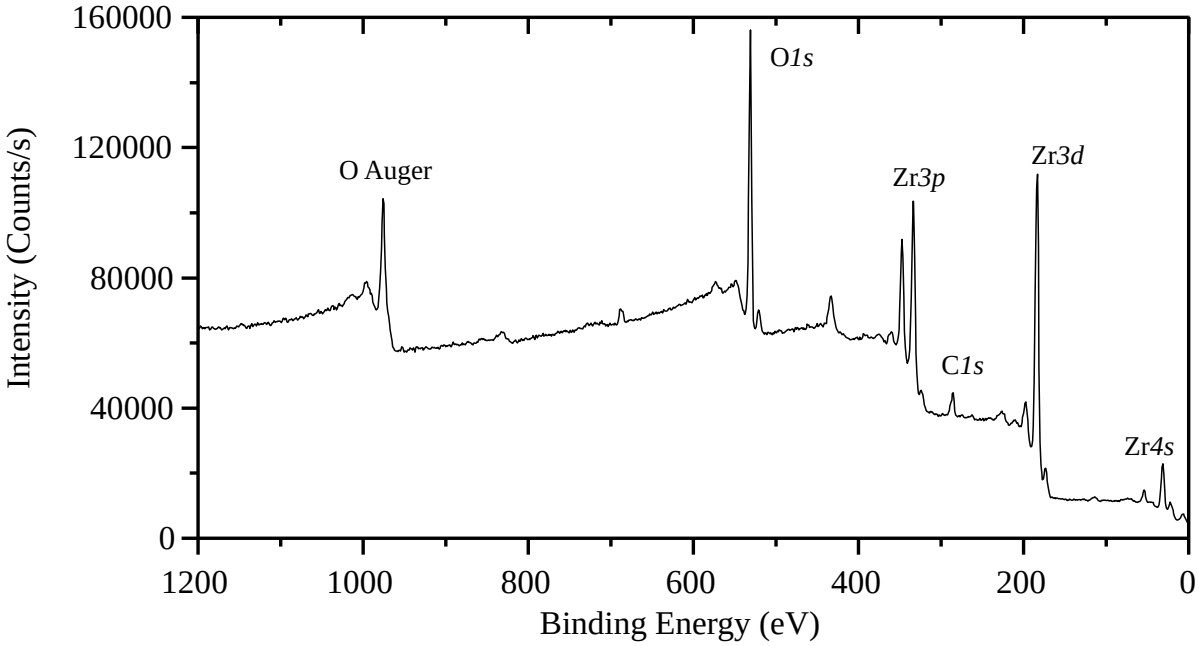

Figure 3.2: XPS spectrum of a polycrystalline Zr surface, generated using Al Kα X-ray source.

Electrons emitted from orbitals with an angular momentum ($l > 0$), i.e. orbitals other than *s*, give rise to a coupling between the spin (+½, -½), known as the *j-j* coupling, such that *j*, the total angular momentum, is given by ($l+s$), where *l* is the orbital angular momentum and *s* is the spin quantum number. As a result, doublets arise in XPS spectral peaks associated with (*p, d, f*) orbitals. The peak energy split can range between a few meV to more than 10 eV. The spin orbit splitting depends on the atomic mass of the species (higher *Z* increases ΔE, for same *j* value), and increases with *l* for orbitals with the same principal quantum number *n*. For spin-orbit splitting peaks, also known as doublet peaks, they have a fixed ratio for the relative areas given by the degeneracy of the states ($2j+1$) [145]. The intensity of the peaks is directly related to the number of emitted photoelectrons from a specific subshell for an element. However, for a given element *A*, the photoelectron peak intensity for the different subshells will differ from one another (e.g. $3d_{3/2}$ has a different intensity than $2p_{3/2}$) at a specific X-ray energy *hv*. The intensity is dependent on the photoionization cross-section for a given subshell *i*, and the *KE* of the photoelectron. The photoionization cross-section is defined as the probability for an electron from a subshell *i* to be emitted upon interacting with a photon with energy *hv* [152].

The photoionization cross-section value is essential for quantifying the atomic percentage of a chemical species on the surface of the material under investigation. These values are known as "relative sensitivity factors" are either based on theoretical calculations, Scofield cross-sections [153] or on experimental observations as in Wagner sensitivity factors [154], [155]. For obtaining a relative quantification of species present in the topmost layers of a specimen, other considerations must be taken into account. For elements with several photoemission peaks, then the highest intensity peak is usually taken as the reference peak for quantification. However, proper peak fitting and background subtraction must be taken into consideration. There are multiple models for background subtraction; linear or straight background, Tougaard method, Shirley background, and Smart [144], [145].

The linear background is the simplest form of background subtraction where the area under the peak is defined by a straight line that is drawn from end points on either side of the peak. Due to the simplicity of this method, it is extremely sensitive to the location of the user-defined end points. Shirley background on the other hand is less sensitive to the defined end points. It requires the lower binding energy end (higher kinetic energy) to have a lower intensity than the higher binding energy end of the peak. The difference of the intensity of the two points is assumed to

originate from the loss of energy of photoelectrons due to inelastic scattering. Shirley integral method assumes that the peak area at a given binding or kinetic energy is proportional to the background intensity. It is worth noting that Shirley background subtraction is an iterative method, and the higher the number of iterations, the better the estimate of the background [144], [145]. The Smart method is based on the Shirley method with an additional constraint. Smart background was developed by Thermo Fisher Scientific. Smart background insures that the background at any energy point below the peak would not have a higher intensity than any data point in the spectra, while still maximizing the area under the peak. Smart background subtraction is the preferred technique for multi-state peaks as shown in Figure 3.3 (b) showing the difference between linear, Shirley, and Smart background subtraction for Sb*3d* and O*1s* peaks. It is clear from the figure below that linear subtraction would be a poor estimation for the background, especially in this case where there are multiple states engulfed under a peak area, Shirley background would give a better fit, but when putting the additional constraint on the background intensity as with the Smart background, it is evident that the maximum area under the peak is achieved.

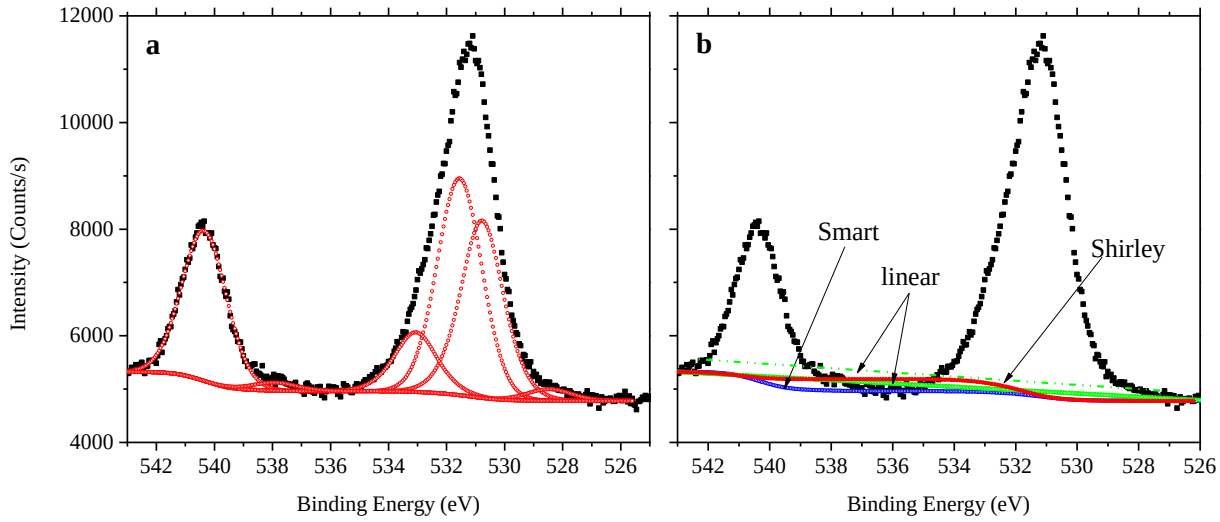

Figure 3.3: High resolution XPS signal (black trace), with deconvoluted peaks for Sb3d and O1s signals. (a) showing the deconvoluted peaks for the sub-species, (b) background subtraction using linear, Shirley and Smart methods.

3.2 Time-of-Flight Secondary Ion Mass Spectrometry

Secondary ion mass spectrometry (SIMS) is a destructive analytical technique that provides elemental composition analysis regarding both the surface and bulk of thin films. SIMS involves a primary ion beam such as Bi^+. A secondary ion beam is used for depth profiling which is in the form of Cs^+, O_2^+, Ar^+ with energies that ranges between a few keV up to 30 keV. The sputtered surface ions are either atoms or clusters of atoms (Figure 3.4 (a)). The nature of the primary ion beam influences the sputtering rate of specific species. Thus, for detecting oxides, it is generally preferred to use a more electropositive primary beam (e.g. Cs^+). The emitted ions have kinetic energies in the 0-100s eV range. A Time of flight (TOF) detector categorizes ions according to their mass to charge ratio, where the ions are accelerated through a "flight tube" with a known length L to a specific kinetic energy K, and the mass is determined from the time it requires the ion to travel through the tube. TOF-SIMS is sensitive up to 1 ppm-ppb, thus can provide qualitatively accurate information regarding the composition of the material [151], [156], [157]. It is worth noting that TOF-SIMS is a qualitative technique, and can only be quantitative provided a reference sample with known composition for calibration. The technique is also adapted for depth profiling, such that a beam of ions is used as the primary sputtering ion beam (e.g. Cs^+, O_2^+) and the ions ejected by this beam are not analyzed. A second beam (e.g. Bi^+) is used to analyze the species on the surface of the area that has been etched. These two beams are interchanged within a single cycle (<1s) and thus an in-depth profile of the material composition over an approximate area of 0.25 mm^2 is produced [158].

3.3 Time-of-Flight Elastic Recoil Detection

Elastic recoil detection (ERD) is a quantitative technique utilized in material science for analysis of concentration profiles in thin films. The technique entails a high energy primary ion beam with energy E_0~20-200 MeV, and mass m_1, which is directed onto a sample at an angle α. The ions are generated and accelerated in a particle accelerator, and are directed on the sample surface at a grazing angle. Upon interaction with the target atoms (m_2), the ions are scattered, and the target atom is recoiled at an angle ϕ, with energy E_2 (Figure 3.4 (b)). The target-ion interaction is Coulombic in nature (as described in equation (3.7)), and thus the conservation of energy and momentum applies. The energy of the recoiled atom E_2 is related to the energy of incident ions E_0

with mass m_1, giving information about the nature of the recoiled atom (m_2), according to the following equation,

$$\frac{E_2}{m_2} = \frac{4\cos^2\phi}{\left(1+\frac{m_2}{m_1}\right)^2}\left(\frac{E_0}{m_1}\right) \tag{3.7}$$

In ERD the ion mass is larger than that of target atoms, i.e. $m_1 > m_2$, and the energy of the incident beam is varied depending on the nature of the target material. By tuning the energy of the incident ions and their mass (i.e. the ion itself), almost all materials can be detected, including hydrogen [159].

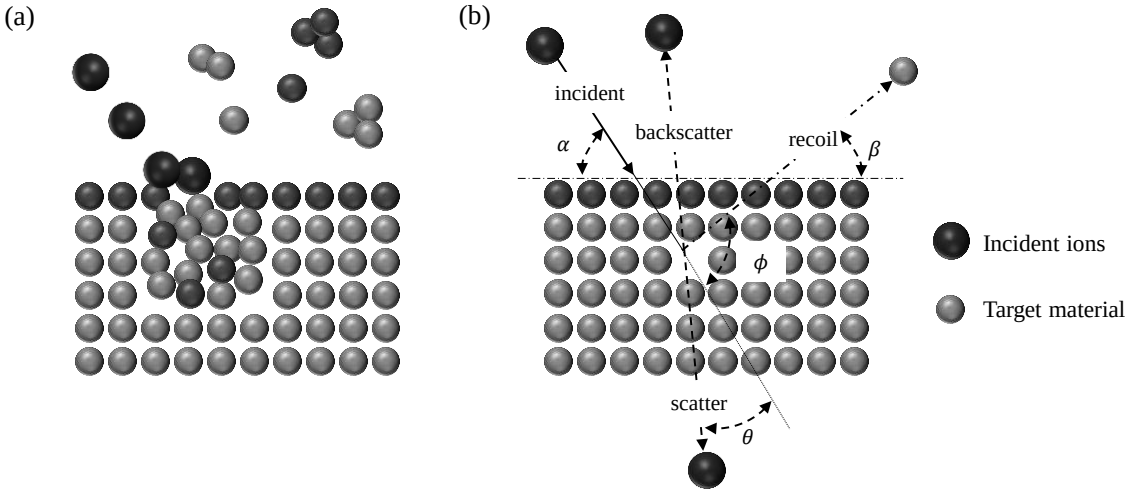

Figure 3.4: Schematic representations of (a) TOF-SIMS (adapted from [156]) and (b) TOF-ERD (adapted from [159]).

CHAPTER 4 RESULTS AND GENERAL DISCUSSION

Presentation

This chapter which encompasses the results and discussion of this thesis are presented in an article entitled as "*Temperature-dependent in situ studies of volatile molecule trapping in a low temperature-activated Zr alloy-based getter*" which has been submitted to Journal of Physical Chemistry C part of American Chemical Society on November 13th, 2016. The objective of the article is to thoroughly analyze the surface properties of the getter by investigating its behavior under various conditions *in situ*. It is also aimed to draw a link between the getter's structure and composition to its properties and the impact on the integration of the getter in MEMS cavities. The text follows describes the experimental details of the work done, results and discussion, and the conclusions from this work. The work described in this chapter was done in the context of integration of the getter in a micro-bolometer developed by Teledyne DALSA Semiconductor in collaboration with the Centre de Collaboration MiQro Innovation (C2MI).

4.1 Abstract

The activation process and the gettering mechanisms of Zr-Co-rare earth metal alloy getters were investigated. The evolution of the surface composition prior to and upon exposure to volatile molecules (O_2, N_2, CO_2) was monitored *in situ* using X-ray photoelectron spectroscopy under annealing conditions compatible with low temperature processing regimes. The thermally activated process of surface oxygen diffusion into the bulk was elucidated and found to involve an activation energy of 0.21±0.02 eV in the 200-350^{o}C temperatures range. This activation process was also found to reversibly transform ZrO_2 into $Zr(OH)_2$ through the interaction with thermally desorbed hydrogen. Carbidic species form upon annealing at 250^{o}C via the interaction with an adventitious carbon layer on the surface, which results in the decrease in the number of surface sites available for subsequent gettering. *in situ* studies of the material reactivity with high purity O_2, N_2, and CO_2 were also investigated. O_2 was found to saturate the surface after single exposure, while CO_2 dissociates into CO and O^-, where O^- is incorporated deeper in the material and CO forms an ad-layer on the surface of the getter. N_2 was found to weakly interact with the partially activated surface, and to form ZrN only upon annealing the sample to 350^{o}C indicating the poor reactivity of the material with N_2 at room temperature. The results display the importance of ridding systems

of residual gases, especially N_2, by properly degassing the system prior to sealing to minimize and/or eliminate trapped gases within devices during operation.

4.2 Experimental details

Our investigations were performed on commercially available Zr-alloyed films sputtered on silicon wafers. Scanning electron microscopy (SEM) was used to examine alloy surface via Omicron NanoSAM system equipped with a UHV Gemini Column with a 15 kV accelerating voltage, operating at a base pressure of 10^{-10} Torr. To monitor the evolution of surface chemistry upon heat treatment and exposure to gases, *in situ* X-ray photoelectron spectroscopy (XPS) studies were carried out using a VG ESCALab 3MKII system, with a 300 W Al Kα source at an energy of 1486.6 eV and a spectrometer work function of 3.60 eV. The X-ray source was operated under an anode bias of 15 kV with an emission current of 20 mA. The UHV system consists of 3 chambers including a load-lock, a preparation chamber, and an analysis chamber, at base pressures of 10^{-4}, 10^{-9}, 10^{-10} Torr, respectively. *in situ* temperature dependent studies were conducted using a resistive heater and the temperature was measured using a thermocouple that is in direct contact with the sample holder. The estimated uncertainty in temperature measurement is approximately ±30°C.

High energy resolution XPS scans were collected prior to each treatment. Scans spanning from 0 to 1400 eV were recorded at an energy step of 1 eV, a pass energy (E_{pass}) of 100 eV, and dwell time of 100 ms. High resolution spectra were collected for each element, with a resolution of 50 meV at E_{pass} energy of 20 eV and dwell time of 100 ms. An average over a minimum 9 scans is considered in these analyses in order to achieve a good signal to noise ratio for each high resolution scan. C*1s* core level orbital was used as a charge reference at a binding energy of 285±0.2 eV. The analyzed area is about 3×2 mm^2. XPS spectra were recorded and analyzed by means of Thermo Avantage v5.952 from Thermo Fisher Scientific. Shirley background subtraction was used for O*1s*, C*1s*, N*1s* XPS peaks, Smart background was used for the metal background subtraction, and relative sensitivity factors based on Wagner approximations were used for quantification of surface composition. Relative atomic composition is given in atomic %, which will be referred to hereon then as %, with an accuracy of ±1%. Handbook of X-ray Photoelectron Spectroscopy by Moulder *et al.* has been used as the main reference for the binding energies [160]. Values of 2.43 eV, 18.3 eV, 16.8 eV, and 15.2±0.2 eV were used for the spin orbit splitting for Zr*3d*, Ce*3d*, La*3d*, and Co*2p* orbitals, respectively[160].

To examine the kinetics of the activation process, different samples were heated under UHV in the XPS analysis chamber. Survey spectra were measured before subjecting the samples to annealing conditions, to have a baseline for the initial concentration of C, O, and Zr on the surface. The samples were then subjected to isothermal annealing, and XPS scans of Zr*3d*, C*1s*, and O*1s* orbitals were recorded. The area under the peaks was integrated to track the absolute change in the amount of Zr, O, and C present on the surface at a given time for each temperature. Each scan took 40 s to collect, and approximately 130 scans were recorded at each given temperature. The integrated area under the peak for O*1s*, C*1s*, and Zr*3d* were plotted as a function of time for each temperature and fitted accordingly. The analysis chamber is equipped with gas inlets, and valves that allow for the control of gas flow into the chamber. High purity gases were used for *in situ* studies O_2 (H_2O < 3 ppm, THC < 0.5 ppm), N_2 (H_2O < 3 ppm, O_2 < 2 ppm, THC < 0.5 ppm), and CO_2 (99.999% purity). Gases were introduced into the analysis chamber up to a pressure of 10^{-5} Torr for various residence times at different temperatures. Exposure is given by Langmuir (L), that is 1L= 10^{-6} Torr s.

Time-of-flight secondary ion mass spectrometry (TOF-SIMS) analysis was performed using IONTOF TOF-SIMS IV, with Bi^+ as primary beam at 25kV (target current of 1.16 pA) and Cs^+ source for depth profiling at an energy of 3keV (target current of 20.13 nA). The sputter time/depth was calibrated by measuring the depth of the 250×250 μm^2 crater using Veeco Dektak® 150 profilometer. TOF-SIMS data was acquired and analyzed using an IONTOF Surface lab 6.2. Time-of-flight elastic recoil detection (TOF-ERD) analysis was carried out using I^{10+} with an energy of 55 MeV. TOF-ERD data was analyzed using Allegria, an ERD interface program[161]. The data was calibrated for depth by approximating the material density based on its constituents. The sensitivity limit in concentration is ±1 atomic %.

4.3 Results and Discussion:

4.3.1 Structure and chemical composition of the getter

Figure 4.1 (a) displays representative SEM images of the as-deposited alloy surface. The material appears to be highly porous and nano-textured with average grain diameter between 20 and 100 nm. The large distribution of grain sizes gives rise to a high active surface area of the getter. The thickness of the film has been measured using cross-sectional SEM and was found to be

approximately 2 μm. EDX analysis shows the film is composed of 80% Zr, 15% Co, 5% traces of REM, including La, Nd, and Ce. The presence of REM has been reported to assist in the activation process of the getter [47], which will be discussed further in the following sections. Shown in Figure 4.1 (b) (inset), the O^- signal in TOF-SIMS drops an order of magnitude at an approximate depth of 70 nm, before it plateaus. The decrease in the O^- signal with increased depth is an artifact from the TOF-SIMS measurement (decrease in sputtering rate with increasing sputtering time). The high concentration of O^- within the "bulk" of the getter reflects the large active surface area of the material, such that there is an oxide passivation layer on the internal surface of the pores and grains within the material. The discrepancy between the thickness of the film measured with cross-sectional SEM (2 μm) and the thickness deduced from calibrated TOF-SIMS depth profile (~1.7 μm) due to a measurement artifact from TOF-SIMS. TOF-ERD (Figure 4.1 (c)) measurement shows the atomic concentration profiles of the main components (Zr-Co) and the other impurities within the alloy. O concentration drops down from ~50% near the surface to ~20% beyond ~250 nm below the surface. Conversely, Zr content increases monotonically beyond a depth of ~250 nm due to the presence of ZrO_2 at the surface and remains constant beyond this point. As for Co, its content is approximately 13.5 ± 0.4% within the material, with a slight depletion near the surface. The concentration of contaminants (N, H, and C) is negligible and remains below 2% across the analyzed thickness.

XPS analysis demonstrates that the surface (depth probed is approximately 4.7±1 nm) of the film is made up of 63.6% O, 18.3% Zr, 15% C, 2.4% Ce, and 0.8% La as shown in Figure 4.2(a). Figure 4.2(b)-(g) show a representative set of XPS spectra recorded for as-deposited getter. Zr and Co appear in their stable oxide states ZrO_2 and CoO, respectively, while La*3d5* at a binding energy of 835 eV, which has been reported to correspond to either hydroxide state $La(OH)_3$ or La_2O_3[160],[162]. Ce is observed in its unstable oxide state as Ce_2O_3[163], [164]. The presence of

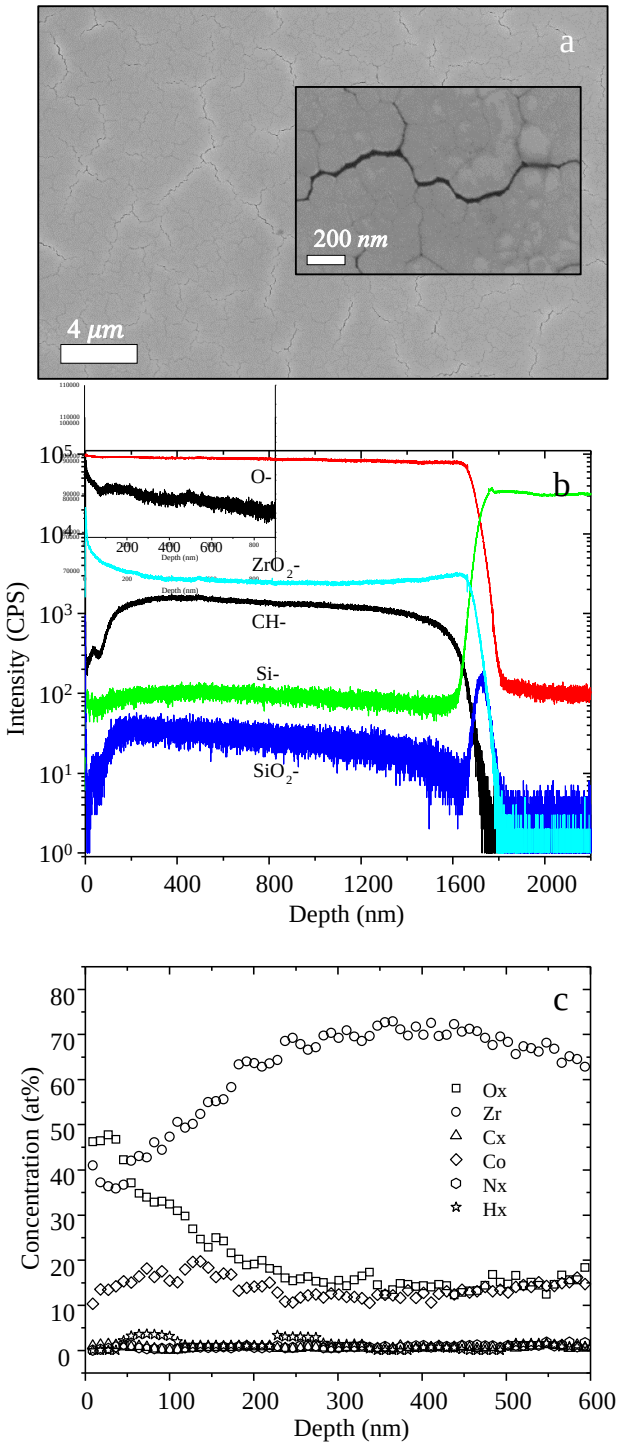

Figure 4.1:(a) SEM image of as received alloy. The inset is a close-up SEM image providing more details on the morphology of the alloy under investigation, (b) TOF-SIMS depth profile of alloy film constituents, with O^- signal shown in inset for clarity, and (c) TOF-ERD concentration profile of the important constituents in as received alloy (uncertainty ±1 at.%).

the Ce^{3+} state indicates that it forms an intermetallic phase with other REM allowing Ce^{3+} to be stable at room temperature. Such behavior has been observed in $CeSnO_x$ intermetallic films, where Ce*3d* orbital displays a Ce^{3+} rather than Ce^{4+} oxidation state [165]. O1s orbital (Figure 4.2(c)) includes 3 peaks, at 529.7, 531.4, and 532.7 eV, which are attributed to metal oxides, metal hydroxides, and contaminant groups (carboxyl/alcohols), respectively. Co*2p* orbital has a shoulder at higher binding energy, which is associated with energy loss mechanisms (shake-ups)[166]. The Ce*3d* orbital has multiplet splitting, which has been previously reported and also attributed to satellites and shake-up loss processes[167]. A summary of the details of the chemical species present on the surface of the getter with their relative quantities is presented in Table 4.1-column 1. The thickness of the oxide layer was approximated to be 2.4±1 nm using the attenuation length of the O*1s* signal in ZrO_2. However, this thickness would not be uniform on the surface of the material investigated in this work due to roughness and porosity. Details of the calculations of the oxide thickness can be found in the work by Morant *et al.*[168].

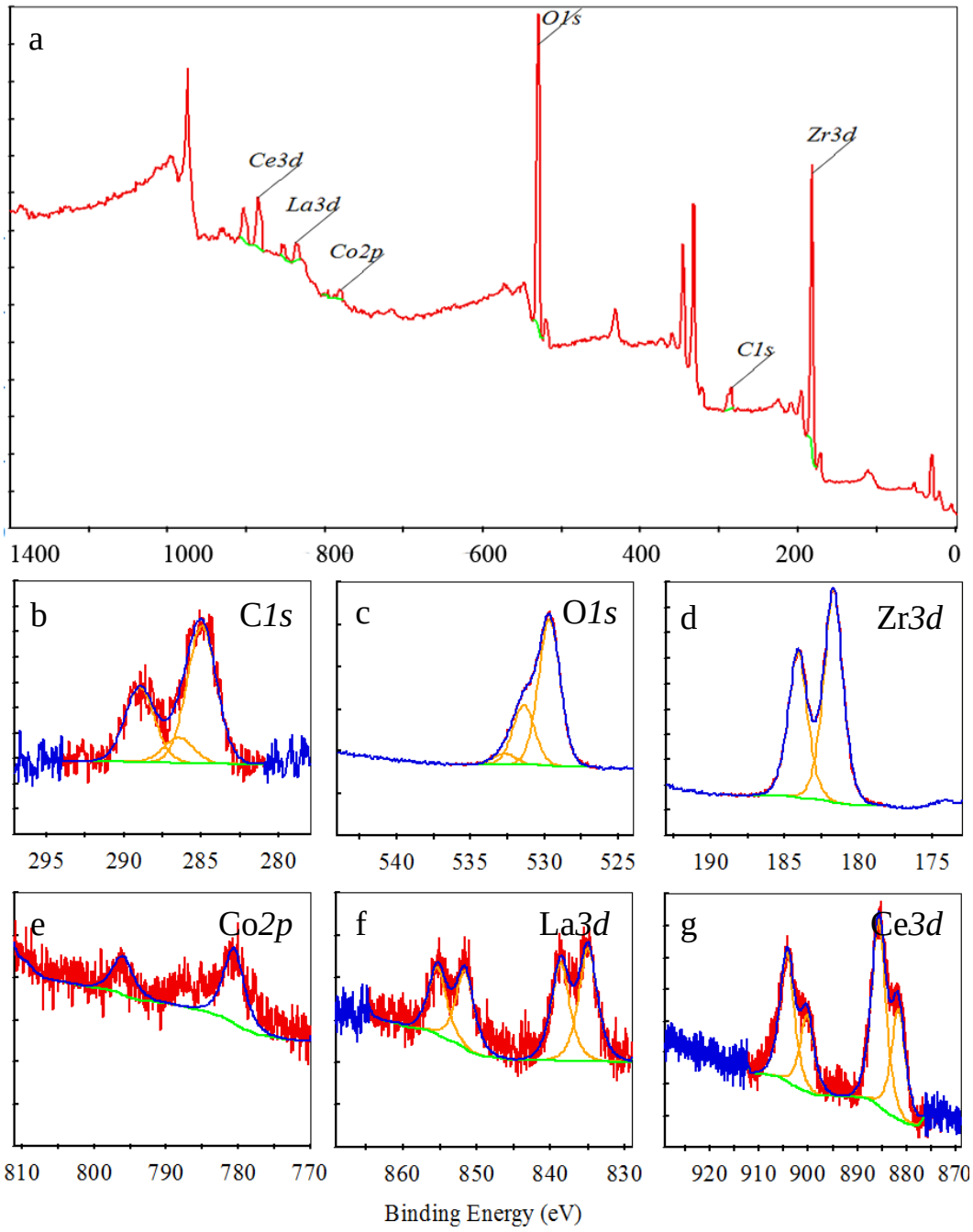

Figure 4.2: XPS of Zr-Co-REM alloy (a) Complete spectrum of as-received alloy, high resolution spectra of (b) C*1s*, (c) O*1s*, (d) Zr*3d*, (e) Co*2p*, (f) La*3d*, and (g) Ce*3d*. (red = raw counts, blue = fit, yellow = deconvoluted peaks, green = subtracted background)

4.3.2 Activation process and its effects on surface composition

The Zr-Co-REM getter was developed for low temperature operating MEMS devices that cannot withstand processing temperatures exceeding 400^{o}C. 350^{o}C was selected as the target temperature for bonding and hence was used for our *in situ* analyses as the activation temperature of the getter. *in situ* monitoring of the surface composition evolution using XPS shows that as the temperature of the material increases to 350^{o}C, peaks corresponding to surface contaminants gradually diminish. However, C appears on the surface as carbidic species at 282 eV as shown in Figure 4.3(a)-(spectrum #2). This observed formation of carbidic species upon heating Zr in the presence of hydrocarbons on the surface is in agreement with early reports on polycrystalline Zr[35], [42], [126], [136], [137], [169]. Hydrocarbon decomposition at high temperatures on transition metals is known to result in incorporation of C into the metal and desorption of hydrogen as gas[170]. We also observe a wider peak with a full width at half maximum (FWHM) of 3.2 eV at a binding energy of 283.8 eV attributed to a combination of oxycarbide groups on the surface, with residual hydrocarbons (Figure 4.3(a)-(spectrum #4)). The formation of oxycarbide groups on metals has been observed previously by Delporte *et al.* where a flow of n-hexanes/H_2 mixture was introduced at 350^{o}C to a molybdenum oxide sample[171]. In their work, they reported a C*1s* peak at 283.5 eV associated to C bonded to a molybdenum oxide. Similarly, in this work, as the hydrocarbons dissociate into free C and H atoms, and as ZrO_2 is reduced to suboxide and metallic species, free C atoms would react with ZrO_x ($0<x<2$) to form ZrO_xC_y.

As the temperature increases, Co is reduced to a complete metallic phase (Figure 4.3(d)-(spectrum #2)), unlike La and Ce both of which remain in their oxide states. In parallel, Zr*3d* orbital evolves into 3 doublet groups (Figure 4.3(c)-(spectra #2 and #3), with Zr*3d5* binding energies at 179.4, 180.5, and 183.4 eV. These doublet states represent the metallic/carbidic Zr^0/ZrC, non-stoichiometric suboxide ZrO_x, and ZrO_2, respectively[133], [134]. The FWHM of the oxide states for Zr*3d5* increases from 1.6 eV at room temperature to 2.4 eV at 200 and 300^{o}C (Table 4.1-columns #2 and #3)). This increase in FWHM can be attributed to an increase in disorder within the oxide matrix as opposed to the stoichiometric oxide initially present on the surface. The initial binding energy of Zr*3d5* for ZrO_2 appeared at 182 eV. After annealing, one of the doublet states for Zr*3d5* appears at a binding energy of 183.4 eV. This state was initially thought of to be ZrO_2, but shifted from its initial position due to the oxide decomposition[169],[172]. This peculiar

behavior of O*1s* and Zr*3d* orbitals during the activation process will be addressed in more detail in the following section.

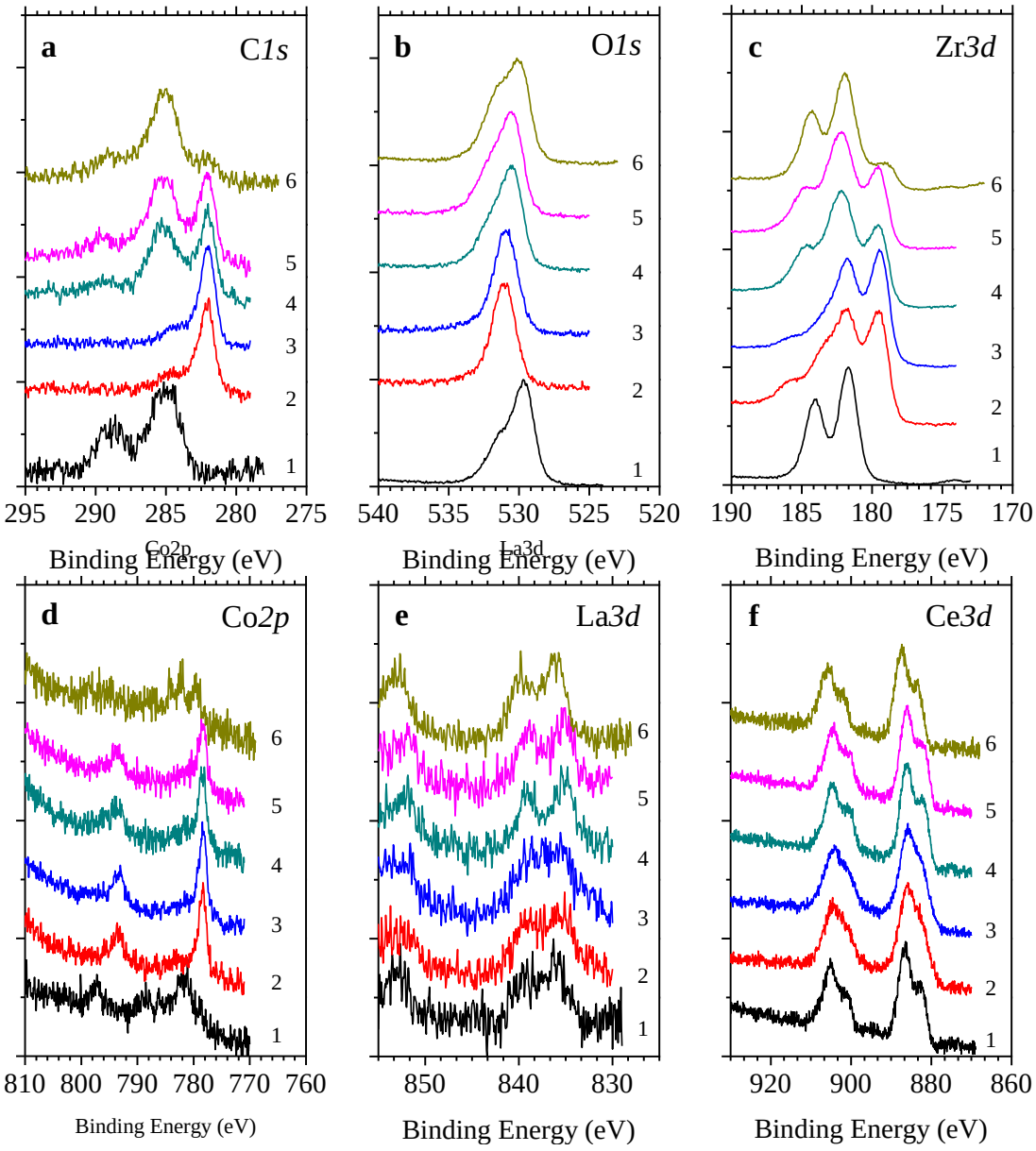

Figure 4.3: Evolution of normalized XPS spectra of (a) C*1s*, (b) O*1s*, (c) Zr*3d*, (d) Co*2p*, (e) La*3d*, and (f) Ce*3d* orbitals under the following consecutive treatments: (1) As received. (2) Annealed at 200 ^{o}C. (3) annealed at 350 ^{o}C. (4) sample cooled down to 25 ^{o}C and exposed to 1.8×10^{4} L of O_2 (30 min at 10^{-5} Torr). (5) Sample #4 exposed to 3.6×10^{4} L of O_2. (6) Sample #5 stored in ambient conditions for 1 week.

Table 4.1: Summary of XPS analysis of the alloy surface at (1) 25ºC (2) 200 ºC. (3) 350 ºC. (4) cooled down to 25 ºC and dosed with 1.8×10^4 L of O_2 (30 min at 1×10^{-5} Torr). (5) Sample 4 dosed with an additional 3.6×10^4 L of O_2. (6) Sample 5 stores in ambient conditions for 1 week. (spectra shown in Figure 4.3). M = Metal

			Atomic% (±1%) [FWHM±0.1 *eV*]					
	E_b		1	2	3	4	5	6
Orbital	(±0.2*eV*)	Species	25ºC	200ºC	350ºC	O_2-01	O_2-02	Ambient
C*1s*	282	M-C		14.6 [1.3]	16.3 [1.2]	8.6 [1.4]	8.5 [1.4]	1.7[1.4]
	283-284	M-C-O		7.6 [3.2]	8.3 [3.0]	13.5 [2.8]	15.8 [2.7]	
	285	C_xH_y	8.1 [2.2]					16.3 [2.5]
	286.5	Alcohol	1.5 [2.2]					
	289	Carboxyl	4.4 [2.2]			2.2 [2.8]	3.4 [2.7]	3.9 [2.5]
O*1s* [1.8eV]	529.7	M-O	42.8			29	27	31.4
	531.5	M-OH	17.5	26.8	22.9	13	13	20.8
	532.3	defect O^- /OH^-		5.2	4	2.9	3.5	
	533	Carboxyl	3.2					4.4
Zr*3d5*	179.4	Zr^0/ZrC		12.7 [1.4]	14.8 [1.3]	6.3 [1.3]	6.6 [1.4]	3.5 [1.9]
	180.5	ZrO_x		14 [2.4]	18.1 [2.4]	7.3 [2.2]	6.2 [2.1]	
	182	ZrO_2	16.9 [1.6]			10.2 [2.2]	9.8 [2.1]	13.6 [1.8]
	183.4	$Zr(OH)_2$		7.7 [2.4]	4.1 [2.4]			
Co*2p3*	778.5	Co^0		2.7 (2.7)	1.9 [2.2]	1.4 [3.5]	1.3 [3.2]	0.7 [3.5]
	780.6	CoO	1.4 [3.2]					
Ce*3d5*	882.2	Ce_2O_3	3.4 [3.5]	6.7 [3.5]	6.8 [3.4]	4.6 [3.5]	4.3 [3.5]	2.1 [3.5]
La*3d5*	835	La_2O_3 /$La(OH)_3$	0.8 [3.2]	1.9 [3.5]	1.6 [3.5]	1.0 [2.7]	0.8 [2.7]	0.7 [2.9]

After activation at 350ºC, the alloy was cooled down to room in approximately 10 minutes. The surface was then exposed to 1.8×10^4 L of pure O_2 gas (10^{-5} Torr for 30 minutes). Subsequently, O_2 was evacuated and the surface composition was measured (Figure 4.3 (b) and (c)-(spectrum #4)), both Zr*3d5* and O*1s* orbitals were found to shift back to 182.5 eV and 530.5 eV, respectively, with an increase in the percentage of stable oxide on the surface (ZrO_2) and a relative decrease in

suboxides. Subsequent exposure to 1.8×10^4 L of O_2 had no significant impact on the surface composition. Dry oxidation resulted in a slight increase in the oxide and hydroxide levels (Table 4.1-columns #3 and #4)). It has been shown that the surface of polycrystalline Zr is saturated upon exposure equivalent to 30-100 L of O_2 at room temperature[35], [124], [131], [168]. When the sample was stored in ambient atmosphere for one week, the surface did not revert to its initial state (see Table 4.1-(column #6)). However, the binding energies of Zr*3d* and O*1s* did revert to their original state, although a fraction of Zr shows carbidic traces, coupled with C*1s* carbidic species. Carbides were not present prior to activation and dry oxidation of the surface. It is also evident from the increase in the FWHM of the C*1s* 285 eV peak (Table 4.1-(columns #1 and #6)) that oxycarbide species are present on the surface after storing the sample in ambient conditions. The fact that the oxidation level was not completely recovered after exposure to ambient atmosphere can be explained by the formation of carbide species on the surface of Zr, which reduces the number of available adsorption sites that would otherwise be available to react with free O on the surface. The carbide poisoning of the surface was observed by Matolín *et al*.[39], where the aging mechanism of a Zr-V (58:42) getter surface was examined using XPS and SIMS. In their study, they repeatedly activated the getter *in situ* in XPS, and exposed it to air, and monitored the increase in carbide species on the surface of the getter. The repeated exposure to air led to the complete loss of the gettering ability of V after four cycles, thus impeding its overall capacity [39].

In order to elucidate the source of the shift in binding energy observed for both O*1s* and Zr*3d* orbitals, a sample was heated *in situ* up to 350^{o}C in incremental steps of 50^{o}C. Since the activation process induces changes mostly in C*1s*, O*1s*, and Zr*3d* orbitals, high resolution spectra were only recorded for the 3 orbitals. Figure 4.4 shows the evolution of C*1s*, O*1s*, and Zr*3d* through thermal annealing up to 350^{o}C. The important observation from this set of data is the gradual shift in binding energy for Zr*3d5* (182 to 183.4 eV) as well as O*1s* (529.9 to 531 eV) from 25 to 350^{o}C. Charging is dismissed as a possible source for this shift, since the data have been adjusted for charging according to the binding energy of C*1s* up to 200^{o}C beyond which no charging effects

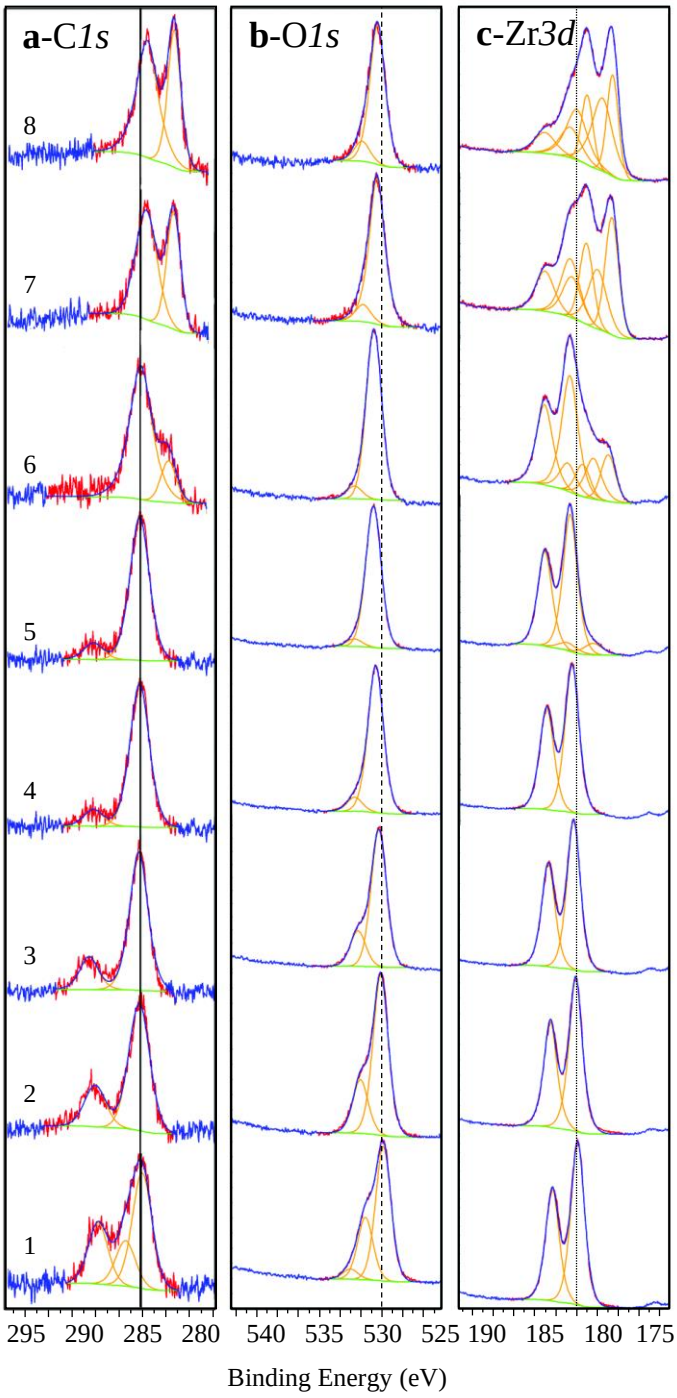

Figure 4.4: Evolution of normalized high resolution XPS spectra as a function of temperature of (a) C*1s*, (b) O*1s*, and (c) Zr*3d* orbitals. (1) 25ºC, (2) 50ºC, (3) 100ºC, (4) 150ºC, (5) 200ºC, (6) 250ºC, (7) 300ºC, (8) 350ºC. (red line represent raw data, blue line represents the overall fit, the deconvoluted peaks are represented by yellow traces, and the background is denoted by green lines).

were observed (Figure 4.4 (a)-(spectra #1-#5)). Moreover, by monitoring the binding energy of C*1s* (285 eV) as a function of temperature (Figure 4.5 (a)), it is noticeable that the peak associated with hydrocarbons does not shift, as opposed to O*1s* and Zr*3d* orbitals which experience shifts to higher binding energy with respect to room temperature spectra.

As the temperature increases, the first changes occur in the physisorbed alcohol/carboxyl groups that begin to desorb from the surface of the sample at 50 ^{o}C (Figure 4.4 (a) and (b)-spectra #2). The shift in binding energy becomes apparent at about 150 ^{o}C (+0.46 eV for O*1s*, +0.42 eV for Zr*3d*), after which a new doublet state for Zr*3d* orbital appears corresponding to ZrC or ZrC-O or ZrH_x[46], [47], [133], [134], [137], [160], [173]. At 200 ^{o}C, the shift reaches +1.0 eV for both orbitals and increases further to about +1.5 eV at 250 ^{o}C with the dissolution of oxides into the bulk, and increase in the carbide and oxycarbide species. Figure 4.4 (a)-(c) and Figure 4.5 (a) show the gradual shift in binding energy for both O*1s* and Zr*3d* orbitals, while C*1s* binding energy is constant up to 250 ^{o}C until the dissociation of surface hydrocarbons becomes significant resulting in the formation of carbide/oxycarbide complexes with Zr. The shift has also been observed with a polycrystalline Zr foil sample that has been subjected to higher annealing temperatures (supplementary information).

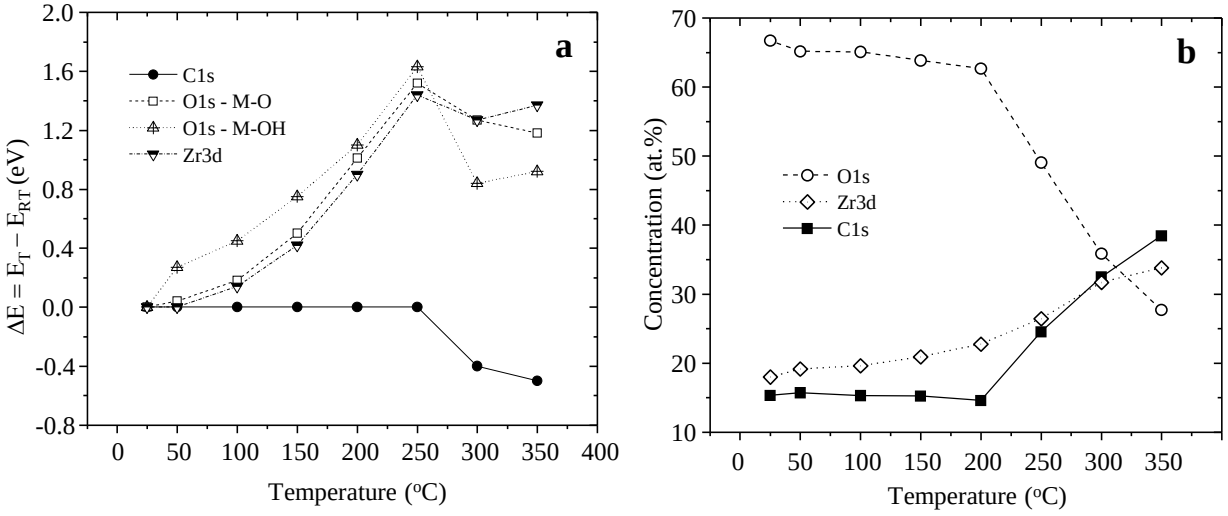

Figure 4.5: (a) Shift in binding energy with respect to room temperature upon thermal annealing for C*1s*, O*1s* and Zr*3d*, vs. temperature ($\Delta E = BE_T - BE_{25^{o}C}$). (b) Atomic concentration as evaluated by XPS measurement of C*1s*, O*1s*, and Zr*3d* orbitals as a function of temperature (±1%).

One may invoke several pathways to explain the observed shifts. Initially, as the temperature increases to 100^{o}C, trapped H_2 molecules within the pores and the bulk of the material tend to desorb and as the oxide layer dissociates, some of the H_2 molecules would thermally dissociate and react with ZrO_x species forming hydroxide species. It has been observed that Zr based materials, as well as pure polycrystalline Zr trap H_2 molecules at temperatures as low as 25^{o}C, if the surface is O-free [174]. H_2 desorption from polycrystalline Zr has been measured using temperature programmed desorption (TPD) [124], [135], [139]. It was found that H_2 desorption peaks at 230^{o}C for polycrystalline Zr sample[124]. Asbury *et al.* examined the influence of the presence of an oxide on the surface of a polycrystalline Zr sample on H_2 desorption [124]. They gradually increased the O concentration on the surface of Zr by controlling the dosage and measured the intensity of the H_2 TPD peak at 230^{o}C as a function of O concentration on the surface. They concluded that a higher surface O concentration increases the desorption of H_2 from the bulk of the material [124]. Peterson *et al.* observed that the presence of O on the surface of Zr induces a H_2 desorption peak at 230^{o}C, which is not present with an O-free Zr[135]. TPD analysis has also been performed on a Zr-based getter and hydrogen desorption was initiated at approximately 200^{o}C [80]. Our observations agree with these findings, where the shift in ZrO_2 and O*1s* orbitals to higher binding energy corresponds to metal hydroxide. This shift becomes significant at 250^{o}C, when the binding energy of the initial ZrO_2 (Zr*3d5*=182 eV) moves to 183.5 eV, which can be attributed to the presence of $Zr(OH)_2$ species [134]. The doublets at 181.2 eV and 179.8 eV are associated with ZrO_x ($0<x<2$) and ZrC-O/Zr-C and some metallic species, respectively. Transition metal hydroxide species have been reported to have a higher binding energy compared to their stable oxide states as has been observed by Biesinger *et al.* [166]. Moreover, the broadening of the peak as indicated by the increase in the FWHM (as shown in Table 4.1), is associated the increase in inhomogeneity of the species present on the surface. Thus, the peak at 183.4 eV (Zr*3d5* at 350^{o}C) would represent a non-stoichiometric $Zr(OH)_2$. Subsequently, when the activated sample was exposed to a controlled O atmosphere (as shown in Figure 4.3 (b) and (c)-spectra #4 and Table 4.1--column #4), the binding energy shifted back to its original value. This observation points to either the formation of full oxide layer on top of a hydroxide layer or the decomposition of hydroxide species into H^+ and O^- to form H_2 upon O_2 chemisorption. Indeed, it has been shown that dissociative chemisorption of O molecules on metal surfaces at room temperature is an exothermic reaction

leading to the decomposition of chemical species on the surface and migration of their ions to deeper layers within the material[175].

It is noteworthy that similar shifts in the binding energy of Zr*3d* and O*1s* were reported by Li, Wong, and Mitchell in their *in situ* studies of a ZrO_2 thin film deposited on Au foil in a H_2O rich environment[134]. Their Zr*3d5* corresponding to ZrO_2 was initially at 182.9 eV and after heating the sample to 500^{o}C in UHV, this binding energy shifted to 183.4 eV. They attributed this shift to desorption of H_2 trapped within the grain boundaries of polycrystalline Zr and the formation of hydroxide species at 183.4 eV[134]. Moreover, they reported that exposure of activated sample to oxidizing conditions reverts Zr*3d* to its original position, consistent with our results. Mašek *et al.* have also reported a similar shift in a Zr-V alloy getter as the sample was heated incrementally to 320^{o}C[41]. They observed a shift to higher binding energies for Zr*3d*, V*2p*, O*1s*, including C*1s*, which they attributed to the Fermi level shift as a result of oxide reduction[40], [41].

The O*1s* peak has a shoulder that evolves throughout the activation process (Figure 4.4(b)). Initially the peak is observed at 531.6 eV, which corresponds to hydroxide species. This peak slowly merges into the main peak as $Zr(OH)_2$ forms and becomes the dominant state in O*1s*. A small peak however is still present at 150^{o}C, at 532.3 eV, and shifts towards 533.2 eV at 250^{o}C. The shift in binding energy for this peak with respect to room temperature is shown in Figure 4.5 (a)-(O1s-M-OH). As the oxide and hydroxide species are dissociating at the surface, the O^- ions become mobile on the surface and within the grain boundaries and pores of the material, which increase their binding energy compared to lattice oxides O^{2-}. O-related defects in metal oxide surfaces have been detected at a binding energy of 532 eV[166], [176]–[178]. The thermally activated process of O^- hopping from a lattice site to an interstitial site weakens the electron screening of the Coulombic attraction of the atomic species, increasing the binding energy of the photoelectron[151]. It is difficult to distinguish these O defect states from defective hydroxyl groups, which can also occur at this binding energy, from unstable hydroxyl groups on metal surfaces. Stable oxide states would be located at a lower binding energy for O*1s* orbital (<530 eV), while oxide or hydroxide defects hydroxide groups would appear at higher binding energies due to a reduced displacement of the electron density with respect to stable oxide species[178], [179]. Physisorbed OH^- and H^+ ions would react resulting in the formation of physisorbed H_2O. This is

evident by the presence of the 533.2 eV peak at 250^{o}C (Figure 4.4(b-6)), which corresponds to physisorbed H_2O on the surface[179], [180].

4.3.3 Kinetics of the getter activation

The activation process is defined by the amount of O that diffuses/dissolves into the bulk, freeing up adsorption sites in the alloy surface for impinging gases. It is evident from Figure 4.5 (b) that 230^{o}C is the onset of activation, where O content decreases drastically. Therefore, in order to elucidate the physical and chemical phenomena involved in the getter activation further, the kinetics of this process were investigated. Samples were heated separately to 200^{o}C, 250^{o}C, 300^{o}C, 330^{o}C, 350^{o}C, and the integrated area under the O, C, and Zr-related peaks were plotted as a function of annealing time. Figure 4.6 (a)-(c) shows the evolution of the XPS signal of C*1s*, Zr*3d*, and O*1s* as a function of time and temperature. The C*1s* signal initially decreases due to contaminant desorption and then the concentration increased ever so slightly with oxide decomposition and carbide formation (Figure 4.6 (a)). The most significant change occurs in the O signal, which in turn influences the relative quantity of Zr on the surface. The attenuation of the O signal follows an exponential decay at an early stage (<800s) before showing a very slow, linear decrease with time. Both exponential and linear behaviors of diffusion of O into polycrystalline Zr have been observed on different time scales. Foord *et al.* observed an exponential decay in the O peak measured by Auger electron spectroscopy (AES) as polycrystalline Zr was heated *in situ* to 340^{o}C over a 160 s interval[35]. They associated the exponential decay of the O signal with the diffusion of O from the surface to the bulk forming a concentration gradient within the material. On the other hand, West and George reported a linear behavior for the integrated XPS peak intensity of O in polycrystalline Zr between 0-70 minutes[132]. West and George explained the linear behavior of the O signal attenuation with an "interface-controlled reaction", where the suboxide at the Zr-ZrO_2 interface acts as a diffusion barrier for O^- ions from the oxide to the metal side. The results presented in Figure 4.6 (c) display both behaviors, indicating two limiting processes taking place in different time scales. Initially, as the sample is rapidly approaching the indicated temperature, the oxide layer begins to decompose and O^- migrates into the bulk. This is a diffusion-limited process. Subsequently, a steady-state is reached at approximately 1000s, as shown in Figure 4.6 (e) for O*1s* signal attenuation at 250 ^{o}C. The time-independent process could be associated with the incorporation of diffused O into the bulk. As the O is increasingly diffusing

into the bulk, driven by the gradient of concentration, the mobile O^- begins to incorporate into the Zr matrix. West and George have attributed the steady state behavior to the presence of a diffusion barrier that prevents O species from diffusing into the bulk of Zr from ZrO_2. The barrier is in the form of a non-stoichiometric interface that develops between the oxide and the metallic phases, which has been proposed as a model for the formation of stable oxides on Zr surfaces[132], [133], [181], [182].

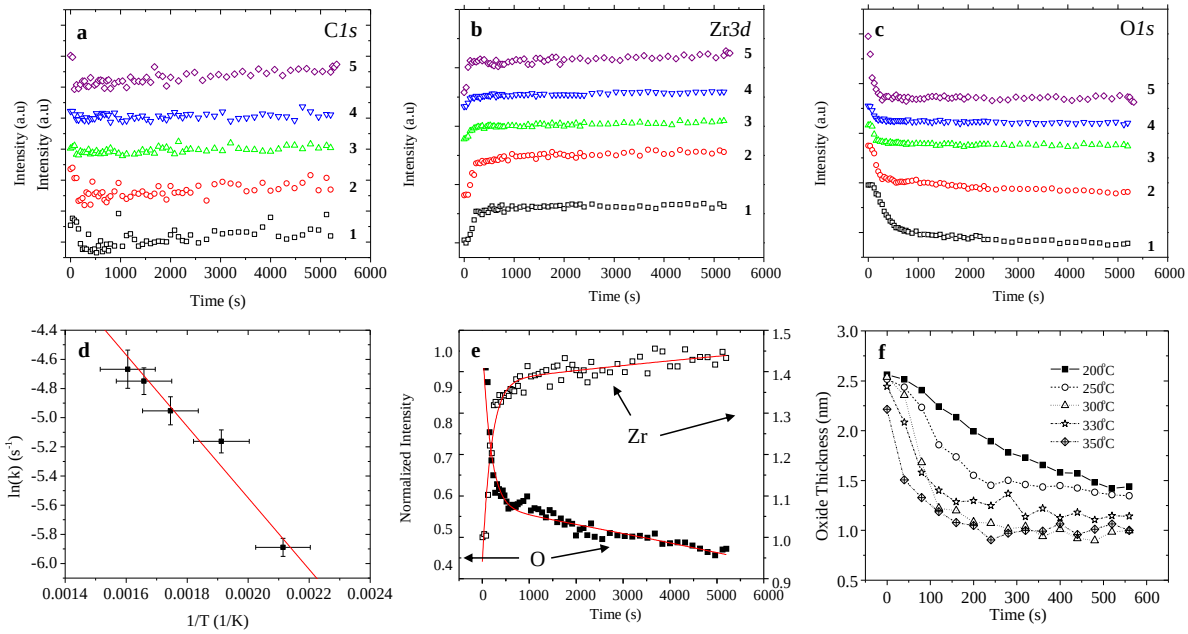

Figure 4.6: Integrated XPS signal evolution for: (a) C*1s*, (b) Zr*3d* and (c) O*1s* annealed at (1) 200 ^oC, (2) 250 ^oC, (3) 300 ^oC, (4) 330 ^oC, (5) 350 ^oC. (d) Arrhenius plot of the diffusion rate for O. (e) Evolution of XPS intensity for O, Zr at 250 ^oC. (f) Oxide thickness vs. time and temperature (±0.2 nm).

The time constant (τ) for the attenuation of the O signal on the surface of the getter as a function of temperature is summarized Table 4.2. As the temperature increases from 200 to 350^oC, the time constant decreases from 360 to 106 s, indicating a faster decomposition and migration of the oxide from the surface and into the bulk of the material. The enhanced oxide decomposition is also evident in the significant decrease in oxide thickness as the temperature increases to 350^oC (Figure 4.6 (f)). A more than 50% decrease in oxide thickness is obtained at 200 s when the sample is heated to 350^oC. The reduction in oxide thickness is not as pronounced at temperatures below

300°C, where the thickness remains above 50% of its original value after reaching steady state. Activation energy for the diffusion of O ions into the bulk was extracted from the Arrhenius plot (Figure 4.6 (d)). The activation energy of the diffusion process was found to be 0.21 ± 0.02 eV. Foord *et al.* have extracted the activation energy of 0.52 eV for O dissolution in polycrystalline Zr at temperatures between 200-350°C via *in situ* AES experiments[35]. Other groups have also estimated the activation energy and diffusion coefficients of O in Zr, however, they were in a higher temperature regime (>400°C)[127]. The activation energy extracted in this work is significantly smaller than that reported by Foord *et al.*[35] due to compositional and morphological differences between polycrystalline Zr and Zr-Co-REM getter investigated in this work. The presence of large pores within the getter structure facilitate the migration of O^- to the bulk of the material, in contrast to polycrystalline Zr, where grains are significantly larger and there are fewer grain boundaries.

Table 4.2. Summary of fitting parameters for the decay of XPS signal for O*1s* as a function of temperature.

Temperature (°C)	Fitting Parameters	
	τ (s)	$k \times 10^{-3}$ (s^{-1})
200	361 ± 22	2.8 ± 0.2
250	175 ± 14	5.7 ± 0.6
300	142 ± 14	7.1 ± 0.7
330	116 ± 11	8.7 ± 0.8
350	106 ± 14	9.4 ± 1

Figure 4.6(a) displays the stability of the carbide species that forms on the surface. The fact that annealing temperature and time has no effect on C signal indicates that carbide is substitutional rather than interstitial. This is further supported by the FWHM of the carbide peak which is 1.2±0.1 eV, whereas that of the oxide peak is 2.3±0.1 eV. The larger FWHM of the oxide peak in the alloy, as well as the attenuation of the O signal as a function of time and temperature and its higher binding energy (>530 eV), indicate that O is an interstitial rather than a lattice oxide. Lattice-oxides are often detected at lower binding energy (O*1s* < 530 eV) due to improved electron transfer from O^{2-} to Zr^{4+} and enhanced electron screening[151]. In polycrystalline Zr, both carbide and oxide form interstitial compounds, which allows the material to dissolve both contaminants in a similar manner [35]. As a result, decomposition of carbonaceous compounds on the alloy poisons the surface and renders the adsorption sites occupied by C unavailable for subsequent adsorption.

Since XPS data can only provide information regarding the changes that occur on the surface, *ex situ* TOF-ERD analysis was utilized to examine the changes of O concentration within the bulk of the material. Two samples were analyzed, one was unprocessed (control sample), and the other sample was annealed in rapid thermal annealing (RTA) under inert conditions (Ar, 1 atm) for 30 minutes at 400^{o}C and cooled down to room temperature under the same atmosphere. The annealed sample was then transferred to the TOF-ERD system under ambient conditions. As shown in Figure 4.7 (a,b), the O content within the bulk of the material increases from 25% to 45% post annealing. The concentration profile post-anneal is also more uniform compared to the untreated sample. The change in the profile is due to the diffusion of the O species present on the surface, which results in the smearing-out of the concentration profile within the bulk. The activation not only drives the O to diffuse from the topmost layers to deeper layers, it also drives the O within the pores (internal surfaces) to incorporate within the metallic matrix. As a result, the pores act as both a facile transport path for O ions from the surface and as active gettering sites when exposed to gas.

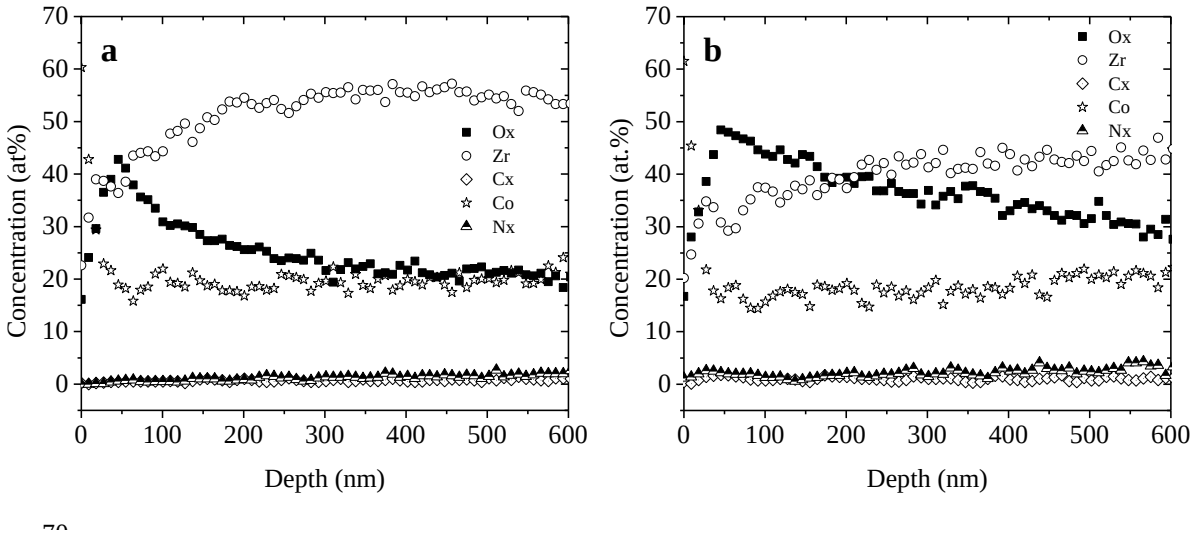

Figure 4.7: TOF-ERD depth profiles of getter sample (a) as-received, (b) treated in RTA at 400 ^{o}C under Ar for 30 min.

4.3.4 Oxygen Trapping

So far, we examined the reactivity of the alloy with O at room temperature, as shown in Figure 4.3-spectra #4 and #5 and Table 4.1-column #4. Investigating the gas-alloy interaction at elevated temperatures would give insight onto the competition between adsorption and diffusion processes. To this end, a sample was annealed *in situ* to 350 ^{o}C under UHV (<10^{-9} Torr) and O_2 gas was introduced into the chamber at a pressure of 10^{-5} Torr for 50 min, the sample was then cooled down to 25 ^{o}C under UHV to examine the surface composition via XPS. It is worth noting that prior to introduction of O_2 into the chamber there was a delay of ~5-10 minutes in order for the sample to reach 350 ^{o}C. Figure 4.8 (a-f) show the spectra for the sample prior (1) and post high temperature oxidation conditions (2). From a qualitative point of view, Zr*3d* and O*1s* show the previously observed shift in binding energy, where to a lesser extent, Zr*3d5* appears at a binding energy of 182.9 eV, and O*1s* 530.9 eV, after the high temperature oxidation (1 eV above baseline measurement). In contrast to the previous experiment, Zr*3d* and O*1s* orbitals reverted to their initial binding energy position after exposure to O_2 *in situ* at room temperature (see Table 4.1 for details).

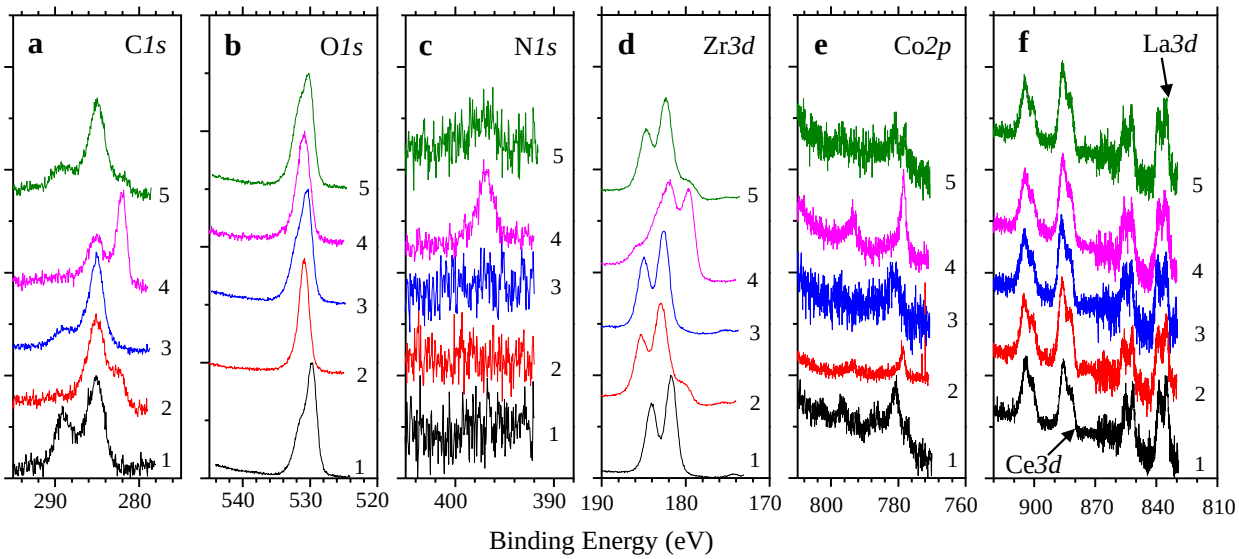

Figure 4.8: Evolution of normalized XPS spectra of (a) C*1s*, (b) O*1s*, (c) N*1s*, (d) Zr*3d*, (e) Co*2p*, (f) Ce*3d* and La*3d* orbitals; (1) as received (2) sample heated to 350^{o}C in the presence of O_2 (10^{-5} Torr for 50 min) followed by cooling to room temperature under UHV (3) Sample 2 stored in ambient atmosphere (4) A new sample heated to 350^{o}C under N_2 (10^{-5} Torr - 50 min) followed by cooling to 25^{o}C under UHV (5) Sample 4 stored in ambient conditions.

High temperature oxidation involves three processes: 1) the reduction of pre-formed oxide on the surface, 2) the dissociative adsorption of O_2 molecules impinging at the surface, and 3) the diffusion and incorporation of O^- ions into the bulk. Initially as the temperature is approaching 350^{o}C, the O concentration reaches 36% of its saturation point after 106 s (from diffusion measurements), thus freeing up adsorption sites for impinging molecules on the surface. After dosing the surface with O_2, O_2 molecules dissociate at the free sites on the surface and O^- ions diffuse into the bulk. The rates of adsorption *vs*. diffusion determine the level of oxidation on the surface and within the bulk of material. Quantitative analysis of the surface composition shows that the initial level of metal oxides (at binding energy of 529.7eV) is ~43% and metal hydroxides (531.5eV) ~18% (Table 4.3-spectra #1 and #2). After exposing the sample to O_2 at 350^{o}C, the surface is composed of a defective layer of mixed oxide and hydroxide species appearing at a binding energy of 530.9 eV amounting to 47%. The fact that the O concentration on the surface of the getter remained approximately constant post treatment indicated that the rate of chemisorption of O_2 is faster than the rate of diffusion of O^- ions into the bulk. This is true under these high dosing conditions (3×10^4 L). If lower doses were imposed, the level of oxide would not reach saturation point. This was observed by Vedel and Schlapbach, where they investigated the oxidation of a Zr-V-Fe (14:5:1) alloy getter at 25, 225, and 425^{o}C[46]. High temperature oxidation with low doses of O_2 (<100 L) was found to have no effect on the surface, where the alloy maintained its metallic state, while doses between 100-1000 L resulted in a sub-oxide formation on the surface[46].

Simultaneous oxidation and diffusion of O^- ions into the bulk results in the formation of non-stoichiometric oxide/hydroxide complexes. As a result, Zr*3d5* and O*1s* states appear at a binding energy, with a higher FWHM compared to their initial state (1.9 eV vs. 1.6 eV for Zr*3d*) which is further proof of the disordered state of the oxide present on the surface of the getter (Table 4.3- columns #1 and #2). Moreover, the introduction of O at high temperature increased the amount of oxycarbides compared to carbides with a ratio of ~6:1, while room temperature oxidation resulted in ~2:1 ratio. The FWHM is, however, the same for both treatments (see Table 4.3). Other orbitals corresponding to REM Figure 4.8 (f) show the stability of lanthanides despite various treatments. On the other hand, a slight change appears in Co*2p* orbital, where cobalt is reduced from its stable oxide state (CoO) to a non-stoichiometric oxide CoO_x (x<1) under high temperature oxidation. La, Ce, and Nd are more electropositive compared to Zr with electronegativity values of 1.1, 1.12, 1.14, and 1.33, respectively[76]. It has been observed with alloys that involve metals

Table 4.3. Analysis for XPS spectra shown in. Figure 4.8. (1) as received (2) 350 ^{o}C + O_2 (10^{-5} Torr, 50 min) (3) Sample 2 stored in ambient conditions (4) New sample heated to 350 ^{o}C and dosed wtih N_2 (10^{-5} Torr, 50 min) and cooled down to 25^{o}C (5) Sample 4 stored in ambient conditions. M = Metal.

			Atomic% (±1%) [FWHM±0.1 *eV*]				
			Sample Number				
	BE			O_2			N_2
Orbital	(±0.2*eV*)	Species	1	2	3	4	5
C*1s*	282	M-C		2.6 [1.5]		12.8 [1.4]	1.4 [1.5]
	283-284	M-C-O		16.2 [2.7]		11.4 [2.6]	15 [2.7]
	285	Hydrocarbon	6.8 [2.2]		17.3 [2.0]		
	286.5	Alcohol	2.0 [2.2]		2.8 [2.0]		
	289	Carboxyl	4.2 [2.2]		4 [2.0]		4.4 [2.7]
O*1s* [1.8eV]	529.7	M-O	43.3		35.4		31.9
	530.6	M-O/-OH		47		20	
	531.5	M-OH	18.2		15.9	11.1	19.6
	533	Carboxyl	2.6		3.9		4.5
	533.6	O^-		4.9		2.0	
N*1s*	396.9					3.5 [1.8]	1.7 [3.5]
Zr*3d5*	179.4	Zr^0/ZrC		4.5 [2.1]		9.1 [1.4]	2.7 [2.0]
	180.5	ZrO_x				14.5 [2.5]	
	182	ZrO_2	16.6 [1.6]		15.8 [1.7]		14 [1.9]
	182.9	$Zr(OH)_x$		18.3 [1.9]			
	183.3	$Zr(OH)_2$				6.3 [2.5]	
Co*2p3*	778.5	Co^0				1.8 [2.9]	
	778.9	CoO_x		1.0 [3.5]			
	780.6	CoO	1.4 [3.5]		0.6 [3.5]		0.7 [3.5]
Ce*3d5*	882.2	Ce_2O_3	3.6 [3.5]	3.9 [3.9]	2.5 [3.5]	5.3 [3.5]	3 [3.5]
La*3d5*	835	La_2O_3 /$La(OH)_3$	1.3 [3.0]	1.5 [3.4]	0.9 [3.1]	2.0 [3.5]	1.2 [3.5]

with different electronegativies that the more electropositive species tends to be reduced at higher temperatures compared to more electronegative species[20], [41], [43]. In Zr_xV_{1-x} alloys, higher V content has been shown to lower the activation temperature of the getter, where ZrV_2 has the lowest reported temperature of most alloys used as getter materials due to the more electronegative nature of V compared to that of Zr[43]. This behavior was also observed in a TiFe alloy where Ti, the more electropositive species, remains oxidized during the thermal activation process while Fe is completely reduced at 350^{o}C[43]. In Zr-Co-REM alloy, Petti *et al*. correlated the thermal stability of lanthanide oxide states to the fact that they participate in the activation process, where O attaches to REM during the diffusion process[47]. Ozawa and Kimura[183] have examined the role of modifying ZrO_2 catalyst supports with REM and observed an enhanced catalytic activity for CO with the addition of 10 mol.% REM into the material. However, the experimental proof of the role of REM in the activation process of the getter is not compelling and further studies are required to establish their specific behavior in the activation and gettering process. Specific studies must address if the REM play a significant role in assisting the reduction process, where a Zr-Co behavior would be compared to its REM counterpart, while taking into account the variations in the microstructure and their role in the activation process.

4.3.5 Nitrogen Trapping

N_2 is often used in various microfabrication processes and thus can often be trapped during material and device processing and can be later outgassed, which can limit the device performance and lifetime. N_2 gettering is therefore important for maintaining a proper environment for normal device operation. The getter reactivity with N_2 was examined at both room temperature and high temperature. A getter sample was activated at 350^{o}C as previously described and exposed to N_2 at pressure of 10^{-5} Torr for 30 min at 25^{o}C. XPS showed no evidence of N-related compounds on the surface. Subsequent exposures to N_2 room temperature for extended times (up to 20 hours at same base pressure) were found to be futile in inducing a reaction on the surface of the getter. However, when N_2 was introduced at high temperature (350^{o}C for 50 min at 10^{-5} Torr), a peak appeared at 396.9 eV corresponding to N*1s* (Figure 4.8 (c)-spectrum #4). N*1s* peak appears on the surface as nitride corresponding to ZrN at its low binding energy and amounting to 3.5% of surface content[184]. These results indicate that N_2 gettering is a thermally activated process. The low reactivity of the getter alloy with N_2 can be attributed to the presence of pre-adsorbed O on the

surface, which renders the surface N_2 inactive. Room temperature dissociative chemisorption of N_2 molecules on metal surfaces occurs if the N-metal bond is larger than 5.12 eV, equivalent to half of the bond energy within a single N_2 molecule[69]. The dissociation energy of the Zr-N bond is on the order of 5.9±0.3 eV, thus theoretically, N_2 would readily react with Zr surfaces[185]. Foord *et al.*[35] and Hoflund *et al.*[125] observed N_2 reaction with Zr at room temperature. Foord *et al.* studied the kinetics of adsorption and absorption of N_2 and NO molecules in polycrystalline Zr via AES[35]. They determined the activation energy of diffusion of N into the bulk by monitoring the attenuation of N Auger signal as a function of time, which was determined to be 0.6 eV.

Foord *et al.* also examined the effect of pre-adsorbed species, specifically O, on the adsorption of N at room temperature. They found the presence of O on the surface of Zr significantly influences N_2 adsorption. Through controlled experiments, they concluded that N chemisorption on Zr would only occur if the amount of pre-adsorbed O were less than 30% of its saturation point. Conversely, the presence of N on the surface has little or no influence on the adsorption of O[35]. N was then considered to form an underlayer, which was also observed on Fe by Ertl and Huber[175] using AES and modeled by Arabczyk *et al.*[186]. Ertl and Huber proposed that the reaction of Fe with O is exothermic, releasing enough energy to displace N atoms to deeper layers. Similar behaviour was observed by Housley and King on W (100) surface[187]. In their study, N-saturated W (100) surface underwent controlled oxidation conditions, and the AES signal of both N and W were found to be attenuated. They concluded that N adatoms were buried in deeper layers due to the formation of an electric field between the W, W-N and chemisorbed O, which drives W^+ to diffuse towards O^- [187].

To investigate N_2 dissociative chemisorption further on the Zr-Co-REM alloy, the following experiment was conducted. First the sample was activated at 350^{o}C. Activation is evident by the significant drop in O intensity as displayed in Figure 4.9 (a)-spectrum #2. The sample was then cooled down and dosed with 1.2×10^4 L of N_2 at 25 ^{o}C. No N-related compounds were detected after N exposure at room temperature, as has been observed previously (Figure 4.9 (b) and (c)-measurement #4). The sample was then annealed at 350^{o}C under UHV after which an N*1s* peak was detected (Figure 4.9 (b) and (c)-measurement #5). The N-exposure and annealing cycle was repeated several times to monitor the evolution of N*1s*. Zr*3d* and C*1s* intensities remain roughly

constant, whereas O*1s* intensity tends to fluctuate but stays within the same order of magnitude after the initial drop due to the activation process (Figure 4.9 (a)). The main observation in Figure 4.9 (c)-measurement #5 is the detection of N-species on the surface only after annealing the sample that was previously dosed with N_2 at room temperature. By repeating the cycles of sample exposure to N_2 at 25^{o}C and annealing at 350^{o}C, we see a gradual increase in the N*1s* intensity (Figure 4.9 (c)). After the first annealing step (Figure 4.9 (b) and (c)-treatment #5), the N*1s* peak observed is located at a binding energy of 397 eV and a FWHM of 1.5 eV. N*1s* at this binding energy is correlated with substitutional N in an oxide matrix[188]. After cooling down the sample, the intensity of N*1s* remains roughly unchanged. Unexpectedly, N increases in intensity after exposing the sample to N_2 at room temperature in the second cycle (Figure 4.9 (c)-measurement #7). This behavior was repeatedly observed in following cycles, except for measurement #10, where the sample was stored under UHV for 12 hours which allows for contaminants (hydrocarbons) within the chamber to adsorb on the surface. In order to explain the increase N content on the surface of the alloy following these treatments, we propose the following mechanisms.

Exposing the alloy surface to N_2 at room temperature allows for a certain amount of N_2 molecules to physisorb onto the surface and within the pores of the material. When irradiating the sample with X-rays during the measurements, molecules on the surface gain enough energy to desorb. Thus, after the first dose of N_2 at room temperature, no N-related species were detected on the surface. Photoinduced gas desorption from stainless steel and Al_2O_3 surfaces has been observed for various gases [189]. On the other hand, N_2 molecules physisorbed within pore sites may re-adsorb on a different pore site post X-ray irradiation. Upon annealing the sample, the trapped N_2 molecules obtain enough thermal energy to hop from one adsorption site to another and dissociate into N^- ions and bind to available sites forming nitrides on the surface. It is also possible that N_2 molecules would dissociate within the pores at room temperature, however, due to the limitation of XPS, these sites cannot be probed.

After the initial annealing cycle, it is observed that N_2 dosing at room temperature results in increase in N content on the surface (Figure 4.9 (c)-measurements #7, 13, 16)). This increase in N content is coupled with the appearance of a shoulder in N*1s* orbital at a binding energy of 399.4±0.2 eV and a FWHM of 3.5 eV Figure 4.9 (b)-spectra #7, 13, and 16)). This new N*1s* mode is correlated with the presence of adsorbed NO molecules or interstitial N [188], [190], [191]. It is

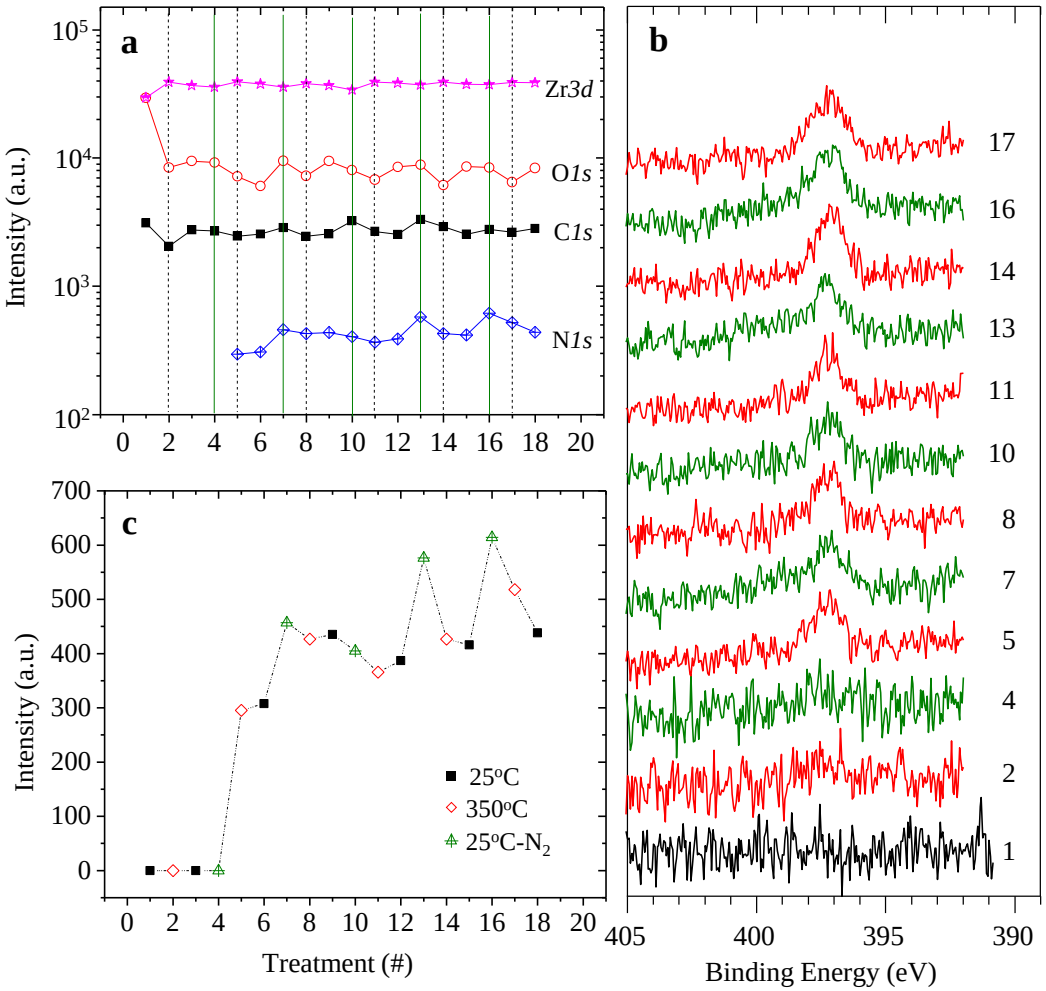

Figure 4.9: (a) Integrated XPS intensity for sample undergone repeated annealing at 350 °C (----), cooling to 25°C (no line), and dosing with N_2 (10^{-5} Torr – 20 min) (—). (b) Evolution of N*1s* signal as the sample undergone multiple annealing and nitriding steps (black = baseline measurement, red = 350 °C, green = N_2 (1.2×10^4 L – 25 °C)). (c) Evolution of normalized XPS intensity for N*1s* under several cycles of N_2 dosing at 25 °C (▲), annealing at 350 °C (◇), and cooling down to 25 °C (■).

difficult to correlate the 399.2 eV peak to a single species. Taking into account that the FWHM is so large (3.5 eV), it is more likely that it represents a combination of weakly adsorbed interstitial (or surface) molecules/atoms. This indicates that the presence of chemisorbed N on the surface act as nucleation sites for the adsorption and dissociation of N_2 molecules on the surface. The decrease of N intensity after annealing the sample at 350°C (see Figure 4.9 (b) and (c)-measurements #11, 14, and 17)) is attributed to the diffusion of chemisorbed N and interstitial N to the bulk of the

material. Note that there is a gradual increase in N intensity with increasing number of cycles Figure 4.9(c)-measurements #6 and #18. This increase indicates that there is an accumulation of N on the surface as the number of cycles increases, which supports our hypothesis of the trapping mechanism of N_2 within the alloy at room temperature.

4.3.6 Carbon Dioxide Trapping

We also investigated the reactivity of the material with CO_2. As with the previous studies, the sample was initially activated at 350^{o}C, and then exposed to CO_2 (1.8×10^4 L) at 25^{o}C. The evolution of the XPS spectra are shown in Figure 4.10 for C*1s* (a), O*1s* (b), and Zr*3d* (c). Exposing the activated alloy surface to CO_2 results an increase in intensity of the 285 eV peak in C*1s* orbital (Figure 4.10 (a)-spectrum #3) accompanied by a slight broadening of the O*1s* peak (Figure 4.10 (b)-spectrum #3). However, no significant change was observed in Zr*3d* orbital. The increase in the C*1s* 285 eV mode is associated with metal-CO bonds, which is consistent with the increase in the 532 eV peak associated with O*1s* orbital. Semi-quantitative analysis shows that metal hydroxide/oxide species surprisingly decreased on the surface (Table 4.4). This result was unexpected, since CO_2 interaction with transition metals often results in dissociation of the molecule into CO and O[192]. Thus one would expect an increase in the oxide content at the surface. The attenuation of both O*1s* and Zr*3d* signals (Table 4.4-column #3) indicates a shadowing effect. Angle-resolved XPS (ARXPS) measurements were then utilized to understand the source of this decrease in the signal. Figure 4.10 (3-6) show the signal evolution as the take-off angle was varied from 0-80^o with respect to the surface normal. By increasing the take-off angle, the XPS signal would be more sensitive to the top-most surface layers. Figure 4.10 (b)-spectrum #6 shows the O*1s* signal measured at a take-off angle of 80^o, where the shoulder at binding energies of 532 and 533 eV are accentuated compared to 0^o signal. This indicates that CO and CO_2 molecules are physisorbed on the surface burying the oxide species underneath (Table 4.4-columns #3 and #6).

Reannealing the sample at 350 ^{o}C displayed a decrease in the higher binding energy peaks in C*1s* and O*1s* orbitals (Figure 4.10 (a) and (b)-spectra #7 and #8). This result indicates that upon annealing, physisorbed CO and CO_2 molecules either desorb or incorporate into the material. However, no increase in carbide formation was observed, which reveals that hydrocarbons are the sole source of carbide species. Therefore, we postulate that CO would not decompose further into

C and O species. Foord *et al.* has shown that CO molecules occupy a single adsorption site[35]. In addition, the lack of evidence for the increase in oxide content means that O^- resulting from CO_2 decomposition would preferentially diffuse to deeper layers than react with available surface sites, which would be populated with CO molecules instead.

Table 4.4. Semi-quantitative analysis of ARXPS data for examining surface reactivity with CO_2 *in situ*.

				Atomic% (±1%)							
				1	2	3 6		7 8		10 13	
			T	25ºC	350ºC	25ºC-CO_2		350ºC		25ºC-CO_2	
Orbital	BE (±0.2eV)	Species	θ	0º	0º	0º	80º	0º	80º	0º	80º
C*1s*	282	Metal-C			14.4	13.6	13.9	14.7	8.9	10.2	6.5
	283-285	Metal-C-O			3.4	10.1	21.1	8	24.5	14.8	29.9
	285	Hydrocarbons		5.75							
	286.5	C-O		3.1							
	289-289.5	Phys-CO		4.55		2.6					
	289.5-290.4	CO_2					2.2			2.8	4.5
O*1s*	529.7	Metal-O		44.2							
	531	Metal-OH		21.1	36.4	30.9	15	34.3	28.7	31	21.8
	532	C-O			9.8	12.9	16	9.7	7.3	11.5	9
	533	CO_2		3.3			5.2				3
Zr*3d5*	179.5	ZrC/Zr^0			14.5	10.6	8	11.1	14	10	9.1
	181.8	ZrO_2/ZrO_x/Zr-C-O		18.1	9.7	8.9	10.6	10.9	7.7	9.5	9
	183.2	$Zr(OH)_2$			11.8	10.4	8.1	11.4	8.9	10.3	7.3

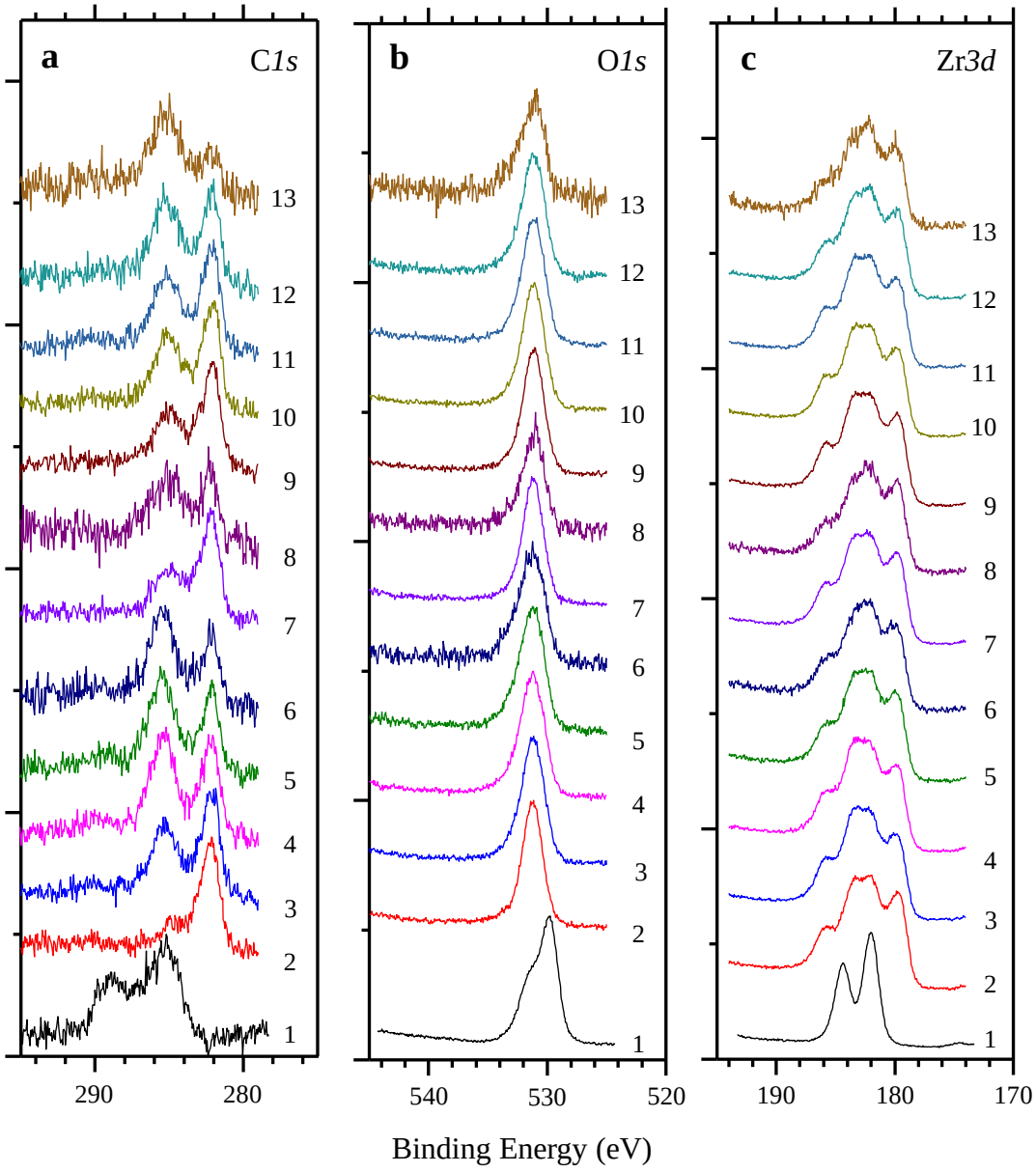

Figure 4.10: Evolution of normalized XPS spectra of (a) C*1s*, (b) O*1s*, (c) Zr*3d*, for samples under the following conditions: (1) untreated, (2) annealed at 350 ^{o}C, (3) sample #2 cooled down to 25 ^{o}C and dosed with 1.8×10^{4} L of CO_2 measured at 0^{o} take off angle. ARXPS measurements on sample #3 (4) 40^{o}, (5) 60^{o}, (6) 80^{o}. (7) Sample #3 heated to 350 ^{o}C and measured at 0^{o} and (8) 80^{o} take-off angles. (9) Sample #7 cooled down to 25 ^{o}C, (10) exposed to 1.8×10^{4} L of CO_2 and measured at 0^{o}, (11) 40^{o}, (12) 60^{o}, and (13) 80^{o}.

4.4 Conclusions

This work investigated gas trapping mechanisms in a Zr-Co-REM alloy getter designed for MEMS cavities. SEM analysis showed the porous nature of the getter with nanocrystalline grains that range between 20-100 nm in size. The bulk of the getter is composed of 80% Zr, 15% Co, and 5% of rare-earth metals (Ce, La, Nd) as displayed by EDS analysis. On the other hand, XPS analysis showed that O makes up 60% of the surface composition. The O content on the surface of the getter is mainly in the form of metal oxides, where ZrO_2 is the dominant surface component. *in situ* thermal activation at 350^{o}C showed the partial activation of the surface, where the O composition decreased to 27% such that ZrO_2 was reduced to ZrO_x and Zr^0. The annealing process was found to partly transform ZrO_x to $Zr(OH)_2$ by interacting with H_2 that out-diffused from the bulk of material evident by the shifting of the binding energy Zr3d and O1s orbitals to higher binding energy (up to 1.4 eV). The activation process also converted the adventitious carbon layer to carbides, where C from hydrocarbons spontaneously bonded to reduced ZrO_2 forming a ZrC compounds. Time- and temperature-dependent measurements of the activation process of the getter in the range of 200-350^{o}C and up to 6000s displayed the effect of temperature on the efficiency of O loss from the surface to the bulk of the getter. The measurements indicated that by increasing the temperature from 200 to 350^{o}C, the time constant for O decay decreased from 361±22 s to 106±14 s. Through extrapolation, it was found that the activation energy for O loss from the surface to the bulk was on the order of 0.21±0.02 eV, indicating the essential role of the pore and grain boundaries in facilitating the O diffusion away from the surface. C signal was found to be approximately constant after the formation of carbides, indicating the poisoning effect of the presence of the carbonaceous adventitious layer.

Controlled exposure of the partially activated surface to O_2 for 30 minutes at room temperature and a pressure of 10^{-5} Torr was found to saturate the surface via formation of metal oxides. On the other hand, exposure to N_2 at room temperature was found to have no observable change in the composition of the surface. However, upon annealing the surface after a single exposure to N_2 at room temperature, nitrides were detected on the surface. This peculiar behavior was associated with the weak trapping of N_2 within the pores of the material beyond the detection limits of the XPS instrument and the surface-diffusion of N-species within the pores and grain boundaries upon annealing. Thus, Zr-Co-REM was found to have a poor gettering capacity for N_2.

For technological applications, N_2 must be eliminated from device processing to avoid build-up of N_2 pressure post bonding of MEMS cavities. At the device level, in our case, 350^{o}C was selected due to its compatibility with the bonding process. The activation temperature of the getter must be equal to or less than the bonding temperature of MEMS cavities. Finally, to improve our understanding of the gettering mechanisms and design superior getter materials, thorough theoretical calculations must be developed to rigorously evaluate the contributions of the pores, grain size distribution, as well as the electronic structure of the surface to the efficiency of the gas-trapping mechanism within such alloys.

CHAPTER 5 CONCLUSION AND PERSPECTIVE

This thesis focused on the investigation of zirconium-cobalt-rare earth metal alloy-based getter properties and its capacity to trap volatile molecules. Chapter 1 introduced the role of porous metallic alloys for vacuum maintenance in vacuum chambers and MEMS cavities and identified the gaps in the current understanding of the basic mechanisms of gas trapping in getter material, specifically the alloys proposed for MEMS devices. Chapter 2 gave an overview on the history and development of getter materials, the operating principles of the material, and its importance for the maintenance of normal operation conditions for a range of MEMS devices. An in-depth analysis of the Zr-Co-REM getter was presented in Chapter 4, where the benefits of its low temperature activation were highlighted as well as its limitations in trapping nitrogen. The results clearly display the limitation of the getter and the influence of the activation temperature on the surface and gettering properties of the material.

The getter investigated in this thesis was shown to be composed of 80% Zr, 15% Co, and 5% of REM (Ce, La, Nd) using elemental dispersive analysis. The surface, however, contained 60% O, mainly in the form of ZrO_2 using XPS. The activation process of the getter was investigated *in situ* using XPS for low temperature activation (350^{o}C) due to its technological importance for MEMS devices. By tracking the evolution of the surface as the sample is heated to 350^{o}C, a significant decrease in the oxygen content to 27% is observed. However, due to the remaining O on the surface post annealing at 350^{o}C, the surface is only partially activated. The onset temperature of activation was found to be 200^{o}C, below which no marked changes were observed. The annealing process drives oxygen from the surface to the bulk, coupled with the partial reduction of zirconium from ZrO_2 to ZrO_x and Zr^0. Time-resolved XPS studies of activation process show that the surface O signal is exponentially attenuated and the Zr signal increases monotonically.

It was found that higher temperatures are coupled with an increase in the rate of surface to bulk diffusion of O, such that the time constant for O exponential decay in signal decreased from 361±22 s to 106±14 s when increasing the temperature from 200 to 350^{o}C. The activation energy of O diffusion from surface to bulk was found to be 0.21±0.02 eV. The low activation energy for the diffusion process is attributed to the presence of pores, which allow for surface diffusion (i.e. hopping mechanism) of O on the inner surface of the pores, increasing the rate of activation. During the activation process, a notable shift in the binding energy of both O*1s* and Zr*3d* was observed.

The binding energy shift of Zr*3d* (182 → 183.4 eV) and O*1s* (530 → 531 eV) was attributed to the formation of hydroxide species induced by upward diffusion and reaction of trapped hydrogen within the bulk of material upon annealing. Studies of trapping of O_2, CO_2, and N_2 on an activated surface display the limitations of the material in trapping O-free gases. The results display the poor performance of the material in trapping N_2 molecules at room temperature on the partially activated surface.

The results summarized above highlight the behavior of the getter under experimental conditions relevant to low temperature integration of devices. However, it is worth noting that, when the getter is incorporated into a device, it is exposed to a mixture of gases and can undergo various annealing steps. Within a device, the integration of the getter often takes place close to the bonding process in order to minimize its exposure to annealing steps prior to bonding which has been shown to deteriorate the getter's performance. Moreover, the activation process may occur during the bonding process, which generally takes place under low vacuum conditions (e.g. 10^{-5} Torr), or can be activated post bonding depending on the stability of the bonding interface and the device's durability to long annealing conditions. During the activation process the getter would be exposed to a mixture of gases and the performance of the getter under such conditions would differ from what has been described above. The getter's affinity to trapping the gases would depend on the sticking probability of the gas molecules, the number of available adsorption sites for the specific molecule, and the diffusion of the species during activation. Hence, since the sticking probability of O_2 is close to 1 on metal surfaces, it would be more efficiently trapped than other gases present within the chamber. However, due to the alloy nature of the getter, the adsorption and chemisorption of different gases would be on preferential sites. The selectivity of sites to certain gases depends on their affinity to trapping the gas which is contingent on the electronic structure and available electrons for bonding at the specific site.

From an industrial point of view, the integration of the Zr-Co-REM getter in a MEMS cavity, for example in micro-bolometers, for vacuum maintenance over the lifetime of the device (up to 10 years) must entail sufficient active surface area (getter). As mentioned in the introduction, the first requirement would be a hermetically sealed device in order to limit the contribution of the surrounding environment to the possible increase in the pressure within the cavity (i.e. leakage). When a hermetic seal is realized, the possible contribution to an increase in the pressure within the cavity of a microbolometer is the degassing of the materials upon absorption of IR, which would

slowly build up the pressure in the cavity and eventually deteriorate the performance of the device. Therefore, the use of gases, especially noble gases, must be substantially reduced during the fabrication process to limit the possible contribution to a future increase in pressure within the micro-cavity. In certain processes, carrier gases (e.g. Ar) are necessary and so a processing step must be implemented prior to bonding of the device which would rid the system of the trapped gases. This step is often in the form of a low temperature anneal under vacuum allowing the materials to degas. However, the integration of a pre-bond annealing step must be carefully and properly implemented, i.e. the impact of the annealing temperature and the duration as well as the pressure in which the annealing takes place on the materials must be taken into account. If a hermetic seal is achieved and trapped gases are sufficiently eliminated within the materials in the cavity, then a getter-less solution can be attained. A getter-less device would significantly reduce the cost of devices and reduce the complexity of the sealing process. However, proper processing also must be taken into account for a getter-less solution, where gases must be completely eliminated within the cavity. These are general guidelines that must be considered for elongating the lifetime of MEMS devices, specific requirements arise due to the complexity of microfabrication processes for different devices and bonding processes and limitations and boundaries that they bring about.

Notwithstanding recent progress, understanding of the influence of pre-adsorbed O on the chemisorption of N_2 is still incomplete, which would require more detailed investigations. In fact, due to the sensitivity of XPS, conclusions and analyses regarding the diffusion processes remain speculative to a certain extent and only limited to surface behavior. A more comprehensive study would also involve *in situ* depth analysis methods that allow for the investigation of the changes of the bulk O concentrations without having to expose the samples to atmospheric conditions. Ideally, the investigations would exploit both surface and bulk analyses techniques that would also allow for *in situ* activation at increasing temperatures with higher accuracies. Another important point to examine is the role of REM in the activation process more closely. Finally, there is a gap in the literature regarding theoretical modeling that would elucidate and quantify the contributions of the pore distribution, grain size (nm-μm) distribution, and their influence on diffusion of contaminant species from the surface to the bulk through pores and within the grains themselves.

REFERENCES

[1] M. Beckner and A. Dailly, “Hydrogen and methane storage in adsorbent materials for automotive applications,” *Int. J. Energy Res.*, vol. 40, no. 1, pp. 91–99, Jan. 2016.

[2] S. Ma and H. Zhou, “Gas storage in porous metal–organic frameworks for clean energy applications,” *Chem. Commun.*, vol. 46, no. 1, pp. 44–53, 2010.

[3] D. Banerjee, A. J. Cairns, J. Liu, R. K. Motkuri, S. K. Nune, C. A. Fernandez, R. Krishna, D. M. Strachan, and P. K. Thallapally, “Potential of metal–organic frameworks for separation of xenon and krypton,” *Acc. Chem. Res.*, vol. 48, no. 2, pp. 211–219, Feb. 2015.

[4] L. Chen, P. S. Reiss, S. Y. Chong, D. Holden, K. E. Jelfs, T. Hasell, M. a Little, A. Kewley, M. E. Briggs, A. Stephenson, K. M. Thomas, J. a Armstrong, J. Bell, J. Busto, R. Noel, J. Liu, D. M. Strachan, P. K. Thallapally, and A. I. Cooper, “Separation of rare gases and chiral molecules by selective binding in porous organic cages,” *Nat. Mater.*, vol. 13, no. 10, pp. 954–960, Jul. 2014.

[5] F. Chang, J. Zhou, P. Chen, Y. Chen, H. Jia, S. M. I. Saad, Y. Gao, X. Cao, and T. Zheng, “Microporous and mesoporous materials for gas storage and separation: a review,” *Asia-Pacific J. Chem. Eng.*, vol. 8, no. 4, pp. 618–626, Jul. 2013.

[6] Y. Zhao, M. Seredych, Q. Zhong, and T. J. Bandosz, “Aminated graphite oxides and their composites with copper-based metal–organic framework: in search for efficient media for CO_2 sequestration,” *RSC Adv.*, vol. 3, no. 25, p. 9932, 2013.

[7] K. Chuntonov, a. Ivanov, and D. Permikin, “Getter films with a reactive component,” *Vacuum*, vol. 85, no. 7, pp. 755–760, 2011.

[8] K. Chuntonov and J. Setina, “Reactive getters for MEMS applications,” *Vacuum*, vol. 123, pp. 42–48, 2016.

[9] K. Chuntonov, A. Atlas, J. Setina, and G. Douglass, “Getters: From Classification to Materials Design,” *J. Mater. Sci. Chem. Eng.*, vol. 4, no. 3, pp. 23–34, 2016.

[10] K. Chuntonov, J. Setina, and G. Douglass, “The Newest Getter Technologies: Materials, Processes, Equipment,” *J. Mater. Sci. Chem. Eng.*, vol. 3, no. 9, pp. 57–67, 2015.

[11] B. Li, H. Wen, W. Zhou, and B. Chen, “Porous Metal–Organic Frameworks for Gas Storage

and Separation: What, How, and Why?," *J. Phys. Chem. Lett.*, vol. 5, no. 20, pp. 3468–3479, Oct. 2014.

[12] R. E. Morris and P. S. Wheatley, "Gas Storage in Nanoporous Materials," *Angew. Chemie Int. Ed.*, vol. 47, no. 27, pp. 4966–4981, Jun. 2008.

[13] A. L. Myers and J. M. Prausnitz, "Thermodynamics of mixed-gas adsorption," *AIChE J.*, vol. 11, no. 1, pp. 121–127, Jan. 1965.

[14] J.-R. Li, R. J. Kuppler, and H.-C. Zhou, "Selective gas adsorption and separation in metal–organic frameworks," *Chem. Soc. Rev.*, vol. 38, no. 5, p. 1477, 2009.

[15] R. T. Yang, *Adsorbents: Fundamentals and Applications*. Hoboken, NJ, USA: John Wiley & Sons, Inc., 2003.

[16] J. J. M. Beenakker, V. D. Borman, and S. Y. Krylov, "Molecular transport in subnanometer pores: zero-point energy, reduced dimensionality and quantum sieving," *Chem. Phys. Lett.*, vol. 232, no. 4, pp. 379–382, Jan. 1995.

[17] S. Roy, A. Chakraborty, and T. K. Maji, "Lanthanide – organic frameworks for gas storage and as magneto-luminescent materials," *Coord. Chem. Rev.*, vol. 273–274, pp. 139–164, 2014.

[18] S. Gadipelli and Z. X. Guo, "Graphene-based materials: Synthesis and gas sorption, storage and separation," *Prog. Mater. Sci.*, vol. 69, pp. 1–60, Apr. 2015.

[19] W. Lu, D. Yuan, D. Zhao, C. I. Schilling, O. Plietzsch, T. Muller, S. Bräse, J. Guenther, J. Blümel, R. Krishna, Z. Li, and H.-C. Zhou, "Porous Polymer Networks: Synthesis, Porosity, and Applications in Gas Storage/Separation," *Chem. Mater.*, vol. 22, no. 21, pp. 5964–5972, Nov. 2010.

[20] B. Ferrario, "Chemical pumping in vacuum technology," *Vacuum*, vol. 47, no. 4, pp. 363–370, 1996.

[21] T. A. Giorgi, "Getters and Gettering," *Jpn. J. Appl. Phys.*, vol. 13, no. S1, p. 53, Jan. 1974.

[22] S. Tominetti and M. Amiotti, "Getters for flat-panel displays," *Proc. IEEE*, vol. 90, no. 4, pp. 540–558, Apr. 2002.

[23] A. Gupta and J. Leck, "An evaluation of the titanium sublimation pump," *Vacuum*, vol. 25,

no. 8, pp. 362–372, Aug. 1975.

[24] N. Yoshimura, *Vacuum technology: Practice for scientific instruments*. 2008.

[25] M. Mura and C. Paolini, “A new generation of getter-coated sputter ion pumps for XHV applications,” *Vak. Forsch. und Prax.*, vol. 19, no. 4, pp. 13–16, Aug. 2007.

[26] O. B. Malyshev, R. Valizadeh, J. S. Colligon, A. Hannah, K. J. Middleman, S. Patel, and V. M. Vishnyakov, “Influence of deposition pressure and pulsed dc sputtering on pumping properties of Ti–Zr–V nonevaporable getter films,” *J. Vac. Sci. Technol. A Vacuum, Surfaces, Film.*, vol. 27, no. 3, p. 521, 2009.

[27] V. Dragoi and E. Pabo, “Wafer bonding for MEMS vacuum packaging,” *ECS Trans.*, vol. 64, no. 1, pp. 221–229, Aug. 2014.

[28] L. Tenchine, X. Baillin, C. Faure, P. Nicolas, and E. Martinez, “NEG thin films for under controlled atmosphere MEMS packaging,” *Procedia Eng.*, vol. 5, pp. 359–362, 2010.

[29] W. C. I. Welch, “Vacuum and Hermetic Packaging of MEMS Using Solder,” University of Michigan, 2008.

[30] Y. Xu, J. Cui, H. Cui, H. Zhou, Z. Yang, and J. Du, “ZrCoCe Getter Films for MEMS Vacuum Packaging,” *J. Electron. Mater.*, vol. 45, no. 1, pp. 386–390, Jan. 2016.

[31] B. Savornin, X. Baillin, E. Blanquet, I. Nuta, D. Saint Patrice, P. Nicolas, P. L. Charvet, and J. L. Pornin, “Outgassing characterization of MEMS thin film packaging materials,” in *2013 IEEE 63rd Electronic Components and Technology Conference*, 2013, pp. 1514–1518.

[32] A. Prodromides, C. Scheuerlein, and M. Taborelli, “Lowering the activation temperature of TiZrV non-evaporable getter films,” *Vacuum*, vol. 60, no. 1–2, pp. 35–41, 2001.

[33] C. Benvenuti, J. M. Cazeneuve, P. Chiggiato, F. Cicoira, A. Escudeiro Santana, V. Johanek, V. Ruzinov, and J. Fraxedas, “A novel route to extreme vacua: the non-evaporable getter thin film coatings,” *Vacuum*, vol. 53, no. 1–2, pp. 219–225, 1999.

[34] K. Ichimura, M. Matsuyama, and K. Watanabe, “Alloying effect on the activation processes of Zr-alloy getters,” *J. Vac. Sci. Technol. A Vacuum, Surfaces, Film.*, vol. 5, no. 2, p. 220, Mar. 1987.

[35] J. S. Foord, P. J. Goddard, and R. M. Lambert, “Adsorption and absorption of diatomic gases

by zirconium: Studies of the dissociation and diffusion of CO, NO, N_2, O_2 and D_2," *Surf. Sci.*, vol. 94, no. 2–3, pp. 339–354, Apr. 1980.

[36] R. Ramesham and R. C. Kullberg, "Review of vacuum packaging and maintenance of MEMS and the use of getters therein," *J. Micro/Nanolithography, MEMS, MOEMS*, vol. 8, no. 3, p. 31307, Jul. 2009.

[37] W. B. Blumenthal, *The Chemical Behaviour of Zirconium*. D. Van Nostrand, 1958.

[38] J. Zemek and P. Jiricek, "XPS and He II photoelectron yield study of the activation process in Ti-Zr NEG films," *User Model. User-adapt. Interact.*, vol. 71, no. 1–2 SPEC., pp. 329–333, 2003.

[39] V. Matolín, K. Mašek, I. Matolínová, T. Skála, and K. Veltruská, "XPS and SIMS study of the ageing mechanism of Zr–V non-evaporable getter films," *Appl. Surf. Sci.*, vol. 235, no. 1–2, pp. 202–206, Jul. 2004.

[40] F. Šutara, I. Matolínová, T. Skála, K. Mašek, and V. Matolín, "Residual surface oxide on ZrV getter—XPS, LEIS and SIMS study," *Vacuum*, vol. 74, no. 2, pp. 305–309, May 2004.

[41] K. Mašek, F. Šutara, T. Skála, J. Drbohlav, K. Veltruská, and V. Matolín, "X-ray photoelectron spectroscopy and static secondary ion mass spectroscopy study of activation mechanism of Zr–V low activation temperature nonevaporable getter films," *J. Vac. Sci. Technol. A Vacuum, Surfaces, Film.*, vol. 21, no. 3, p. 797, 2003.

[42] S. Fabík, V. Cháb, V. Dudr, K. Mašek, K. C. Prince, F. Šutara, K. Veltruská, N. Tsud, M. Vondráček, and V. Matolín, "Activation of binary Zr–V non-evaporable getters: a soft X-ray photoemission study of carbide formation," *Surf. Sci.*, vol. 566–568, no. 1–3 PART 2, pp. 1246–1249, Sep. 2004.

[43] F. Meli, Z. Sheng, I. Vedel, and L. Schlapbach, "XPS analysis of the getter mechanism and getter activation process," *Vacuum*, vol. 41, no. 7–9, pp. 1938–1940, 1990.

[44] X. Yang, J. Li, T. Zhang, R. Hu, X. Xue, X. Wang, and H. Fu, "In situ investigation on transformation of valence on the surface of the alloy during thermal activation," *Solid State Commun.*, vol. 151, no. 11, pp. 842–845, Jun. 2011.

[45] M. Sancrotti, G. Trezzi, and P. Manini, "An x-ray photoemission spectroscopy investigation

of thermal activation induced changes in surface composition and chemical bonds of two gettering alloys: Zr_2Fe versus $Zr_{57}V_{36}Fe_7$," *J. Vac. Sci. Technol. A Vacuum, Surfaces, Film.*, vol. 9, no. 2, p. 182, 1991.

[46] I. Vedel and L. Schlapbach, "Surface reactivity of Zr–V–Fe getter alloys exposed to H_2O, CO, and O_2 at 300 and 700 K," *J. Vac. Sci. Technol. A Vacuum, Surfaces, Film.*, vol. 11, no. 3, pp. 539–542, May 1993.

[47] D. Petti, M. Cantoni, M. Leone, R. Bertacco, and E. Rizzi, "Activation of Zr-Co-rare earth getter films: An XPS study," *Appl. Surf. Sci.*, vol. 256, no. 21, pp. 6291–6296, 2010.

[48] S. Okamura, *History of Electron Tubes*. IOS Press, 1994.

[49] D. MacIsaac, G. Kanner, and G. Anderson, "Basic physics of the incandescent lamp (lightbulb)," *Phys. Teach.*, vol. 37, no. 9, p. 520, 1999.

[50] P. della Porta, "'Gettering': An Integral Part of Vacuum Technology," in *Proceedings of the 39th National Symposium of American Vacuum Society*, 1992, pp. 9–13.

[51] A. Roth, *Vacuum Technology*. Amsterdam, The Netherlands: Elsevier Science B.V., 1990.

[52] C. Z. Liu, L. Q. Shi, S. L. Xu, Z. Y. Zhou, S. Z. Luo, and X. G. Long, "Kinetics of hydrogen uptake for getter materials," *Vacuum*, vol. 75, no. 1, pp. 71–78, 2004.

[53] C. Boffito and A. Corazza, "Getters for lighting applications," in *CRC Press*, 2004, pp. 95–104.

[54] S. Caplet, N. Sillon, M.-T. Delaye, and P. Berruyer, "Vacuum wafer-level packaging for MEMS applications," in *Proceedings of SPIE - The International Society for Optical Engineering*, 2003, vol. 4979, no. 1, p. 271.

[55] A. Corazza and R. C. Kullberg, "Vacuum maintenance in hermetically sealed MEMS packages," in *Micromachining and Microfabrication*, 1998, vol. 3514, no. September, pp. 82–90.

[56] A. G. Jackson, "Production of Ultrahigh Vacuum by Flashed Getters," *J. Vac. Sci. Technol.*, vol. 4, no. 1, p. 42, Jan. 1967.

[57] J. Kovač, O. Sakho, P. Manini, and M. Sancrotti, "Near-surface chemistry in Zr_2Fe and ZrVFe studied by means of x-ray photoemission spectroscopy: A temperature-dependent

study," *J. Vac. Sci. Technol. A Vacuum, Surfaces, Film.*, vol. 18, no. 6, p. 2950, 2000.

[58] T. S. Pump, "Titanium sublimation pump," *Vacuum*, 1968. [Online]. Available: https://www.vacom.de/en/products/ion-getter-and-titanium-sublimation-pumps/titanium-sublimation-pumps. [Accessed: 21-Apr-2016].

[59] K. Welch, "Titanium sublimation pumping," in *Capture Pumping Technology*, Elsevier, 2001, pp. 195–227.

[60] V. Provenzano, "Nanostructured Materials for Gas-Reactive Applications," in *Nanostructured Materials*, Dordrecht: Springer Netherlands, 1998, pp. 335–359.

[61] J. C. Turnbull, "Barium, strontium, and calcium as getters in electron tubes," *J. Vac. Sci. Technol.*, vol. 14, no. 1, p. 636, 1977.

[62] J. R. Elliot, R. . Williams, L. Keller, and R. J. Taylor, "Preliminary investigations of the surface chemistry of titanium gettering," *J. Nucl. Mater.*, vol. 122 & 123, pp. 1151–1155, 1984.

[63] D. Edwards and C. Lanni, "Ti getter study," *J. Vac. Sci. Technol.*, vol. 17, no. 6, p. 1373, Nov. 1980.

[64] V. L. Stout and M. D. Gibbons, "Gettering of Gas by Titanium," *J. Appl. Phys.*, vol. 26, no. 12, p. 1488, 1955.

[65] L. F. Ehrke and C. M. Slack, "An Investigation into the Gettering Powers of Various Metals for the Gases Hydrogen, Oxygen, Nitrogen, Carbon Dioxide and Air," *J. Appl. Phys.*, vol. 11, no. 2, p. 129, 1940.

[66] J. M. Gregoire, R. B. Van Dover, J. Jin, F. J. Disalvo, and H. D. Abruña, "Getter sputtering system for high-throughput fabrication of composition spreads," *Rev. Sci. Instrum.*, vol. 78, no. 7, 2007.

[67] M. Y. Park, H. Ha, W. B. Kim, J. S. Park, C. Y. Suh, and S. B. Woo, "Activation and Gas Sorption Properties of Nano-Size Titanium Powder Getters," *Solid State Phenom.*, vol. 124–126, pp. 1281–1284, 2007.

[68] R. J. Knize and J. L. Cecchi, "Theory of bulk gettering," *J. Appl. Phys.*, vol. 54, no. 6, p. 3183, 1983.

[69] M. W. Roberts and C. S. McKee, *Chemistry of the metal-gas interface*. Clarendon Press, 1978.

[70] T. Smith, "Effect of Surface Coverage and Temperature on the Sticking Coefficient," *J. Chem. Phys.*, vol. 40, no. 7, p. 1805, 1964.

[71] A. Föhlisch, M. Nyberg, P. Bennich, L. Triguero, J. Hasselström, O. Karis, L. G. M. Pettersson, and A. Nilsson, "The bonding of CO to metal surfaces," *J. Chem. Phys.*, vol. 112, no. 4, p. 1946, 2000.

[72] F. Le Pimpec, O. Gröbner, and J. M. Laurent, "Electron stimulated molecular desorption of a non-evaporable Zr-V-Fe alloy getter at room temperature," *Nucl. Instruments Methods Phys. Res. Sect. B Beam Interact. with Mater. Atoms*, vol. 194, no. 4, pp. 434–442, 2002.

[73] M. Methfessel, D. Hennig, and M. Scheffler, "Trends of the surface relaxations, surface energies, and work functions of the 4d transition metals," *Phys. Rev. B*, vol. 46, no. 8, pp. 4816–4829, Aug. 1992.

[74] S. Poulston, P. M. Parlett, P. Stone, and M. Bowker, "Surface oxidation and reduction of CuO and Cu2O studied using XPS and XAES," *Surf. Interface Anal.*, vol. 24, no. 12, pp. 811–820, 1996.

[75] M. C. Deibert and R. Kahraman, "An Auger spectroscopic investigation of the high temperature reduction of zirconium dioxide surfaces in vacuum," *Appl. Surf. Sci.*, vol. 37, no. 3, pp. 327–336, Jul. 1989.

[76] A. L. Allred, "Electronegativity values from thermochemical data," *J. Inorg. Nucl. Chem.*, vol. 17, no. 3–4, pp. 215–221, Jun. 1961.

[77] A. Prodromides, C. Scheuerlein, and M. Taborelli, "The characterisation of non-evaporable getters by Auger electron spectroscopy: Analytical potential and artefacts," *Appl. Surf. Sci.*, vol. 191, no. 1–4, pp. 300–312, 2002.

[78] E. Puppin, L. Braicovich, B. De Michelis, P. Vavassori, and E. Vescovo, "Electron spectroscopy study of the oxidation of a Zr-Fe getter," *Surf. Sci.*, vol. 264, no. 3, pp. 429–434, Mar. 1992.

[79] K. Ichimura, K. Ashida, and K. Watanabe, "Surface characterization of a Zr–V–Fe getter by

XPS-SIMS—activation process and D_2O exposure," *J. Vac. Sci. Technol. A Vacuum, Surfaces, Film.*, vol. 3, no. 2, p. 346, Mar. 1985.

[80] M. M. Günter, D. Herein, R. Schumacher, G. Weinberg, and R. Schlögl, "Microstructure and bulk reactivity of the nonevaporable getter $Zr_{57}V_{36}Fe_7$," *J. Vac. Sci. Technol. A Vacuum, Surfaces, Film.*, vol. 16, no. 6, p. 3526, Nov. 1998.

[81] M. C. Bellachioma, J. Kurdal, M. Bender, H. Kollmus, A. Krämer, and H. Reich-Sprenger, "Thin film getter coatings for the GSI heavy-ion synchrotron upgrade," *Vacuum*, vol. 82, no. 4, pp. 435–439, 2007.

[82] L. Chao-Zhuo and S. Li-Qun, "Effect of Nickel Alloying Layer on Hydrogen Absorption Ability of Zr–Al Getter Material," *Chinese Phys. Lett.*, vol. 21, no. 6, pp. 1035–1038, Jun. 2004.

[83] O. B. Malyshev, K. J. Middleman, J. S. Colligon, and R. Valizadeh, "Activation and measurement of nonevaporable getter films," *J. Vac. Sci. Technol. A Vacuum, Surfaces, Film.*, vol. 27, no. 2, p. 321, 2009.

[84] P. Sutter, S. A. Tenney, F. Ivars-Barcelo, L. Wu, Y. Zhu, and E. Sutter, "Alloy oxidation as a route to chemically active nanocomposites of gold atoms in a reducible oxide matrix," *Nanoscale Horiz.*, 2016.

[85] J. Drbohlav, I. Matolínová, K. Mašek, and V. Matolín, "Sims study of Ti–Zr–V NEG thermal activation process," *Vacuum*, vol. 80, no. 1–3, pp. 47–52, Oct. 2005.

[86] C. Benvenuti, P. Chiggiato, P. Costa Pinto, A. Prodromides, and V. Ruzinov, "Influence of the substrate coating temperature on the vacuum properties of Ti–Zr–V non-evaporable getter films," *Vacuum*, vol. 71, no. 1–2, pp. 307–315, May 2003.

[87] O. B. Malyshev, R. Valizadeh, J. S. Colligon, a. Hannah, K. J. Middleman, S. Patel, and V. M. Vishnyakov, "Influence of deposition pressure and pulsed dc sputtering on pumping properties of Ti–Zr–V nonevaporable getter films," *J. Vac. Sci. Technol. A Vacuum, Surfaces, Film.*, vol. 27, no. 3, p. 521, 2009.

[88] C. C. Li, J. L. Huang, R. J. Lin, and D. F. Lii, "Preparation and characterization of non-evaporable porous Ti-Zr-V getter films," *Surf. Coatings Technol.*, vol. 201, no. 7 SPEC. ISS., pp. 3977–3981, 2006.

[89] Y. Xu, J. Cui, H. Cui, H. Zhou, Z. Yang, and J. Du, “Influence of deposition pressure, substrate temperature and substrate outgassing on sorption properties of Zr–Co–Ce getter films,” *J. Alloys Compd.*, vol. 661, pp. 396–401, Mar. 2016.

[90] M. Wu, J. Moulin, S. Lani, G. Hallais, C. Renard, and A. Bosseboeuf, “Low temperature activation of Au/Ti getter film for application to wafer-level vacuum packaging,” *Jpn. J. Appl. Phys.*, vol. 54, no. 3, p. 30220, Mar. 2015.

[91] V. Chidambaram, X. Ling, and C. Bangtao, “Titanium-Based Getter Solution for Wafer-Level MEMS Vacuum Packaging,” *J. Electron. Mater.*, vol. 42, no. 3, pp. 485–491, Mar. 2013.

[92] L. Tenchine, X. Baillin, C. Faure, P. Nicolas, E. Martinez, and A. M. Papon, “NEG thin films for under controlled atmosphere MEMS packaging,” *Sensors Actuators, A Phys.*, vol. 172, no. 1, pp. 233–239, 2011.

[93] R. K. Sharma, A. K. Sinha, Jagannath, D. C. Basak, S. C. Gadkari, M. R. Singh, and S. K. Gupta, “Surface studies and measurement of pumping characteristic of NEG coating (Ti-V-Zr),” in *2014 International Symposium on Discharges and Electrical Insulation in Vacuum (ISDEIV)*, 2014, pp. 529–532.

[94] M. P. Lozano and J. Fraxedas, “XPS analysis of the activation process in non-evaporable getter thin films,” *Surf. Interface Anal.*, vol. 30, no. 1, pp. 623–627, 2000.

[95] G. Ron, R. Oort, and D. Lee, “A simple, high-yield, apparatus for NEG coating of vacuum beamline elements,” *J. Instrum.*, vol. 5, no. 12, pp. P12007–P12007, 2010.

[96] J. Pavluch, L. Zommer, K. Masek, T. Skala, F. Sutara, V. Nehasil, I. Pis, and Y. Polyak, “Non-destructive depth profiling of the activated Ti-Zr-V Getter by means of excitation energy resolved photoelectron spectroscopy,” *Anal Sci*, vol. 26, no. 2, pp. 209–215, 2010.

[97] M. Ferreira, D. Tallarico, and P. Nascente, “Preparation and characterization of Ti-Zr-V non-evaporable getter films to be used in ultra-high vacuum,” in *Synchrotron Radiation in Materials Science: 6th International Conference*, 2009, pp. 168–172.

[98] F. Šutara, T. Skála, K. Mašek, and V. Matolín, “Surface characterization of activated Ti-Zr-V NEG coatings,” *Vacuum*, vol. 83, no. 5, pp. 824–827, 2009.

[99] M. Nishiwaki and S. Kato, “Influence of electron irradiation and heating on secondary electron yields from non-evaporable getter films observed with in situ x-ray photoelectron spectroscopy,” *J. Vac. Sci. Technol. A Vacuum, Surfaces, Film.*, vol. 25, no. 4, p. 675, 2007.

[100] N. Gupta, Jagannath, R. K. Sharma, S. C. Gadkari, K. P. Muthe, R. Mukundhan, and S. K. Gupta, “Studies of thin films of Ti- Zr -V as non-evaporable getter films prepared by RF sputtering,” vol. 795, pp. 794–795, 2013.

[101] E. Giorgi, C. Boffito, and M. Bolognesi, “A new Ti-based non-evaporable getter,” *Vacuum*, vol. 41, pp. 1935–1937, 1990.

[102] Y. Zhang, X. Y. Wei, C. H. Mao, T. F. Li, P. Yuan, and J. Du, “Preparation and pumping characteristics of Ti–7.5wt.%Mo getter,” *J. Alloys Compd.*, vol. 485, no. 1–2, pp. 200–203, Oct. 2009.

[103] E. Narducci, J. Kovac, F. Ghezzi, N. Venkataramani, and M. Sancrotti, “Water dissociation and selective absorption in the $Zr[V_{0.5}Fe_{0.5}]_2$ gettering alloy: An x-ray photoemission spectroscopy investigation,” *J. Vac. Sci. Technol. A Vacuum, Surfaces, Film.*, vol. 17, no. 2, p. 385, 1999.

[104] D. Cohen, M. Nahmani, G. Rafailov, S. Attia, Z. Shamish, M. Landau, J. Merchuk, and Y. Zeiri, “Oxidation mechanism of porous Zr_2Fe used as a hydrogen getter,” *Appl. Radiat. Isot.*, vol. 107, pp. 47–56, Jan. 2016.

[105] J. Kovač, O. Sakho, P. Manini, and M. Sancrotti, “Evaluation of temperature-dependent surface chemistry in Zr_2Fe and ZrVFe via X-ray photoemission spectroscopy,” *Surf. Interface Anal.*, vol. 22, no. 1–12, pp. 327–330, Jul. 1994.

[106] V. Matolín, J. Drbohlav, and K. Mašek, “Mechanism of non-evaporable getter activation XPS and static SIMS study of $Zr_{44}V_{56}$ alloy,” *Vacuum*, vol. 71, no. 1–2 SPEC., pp. 317–322, 2003.

[107] V. Matolín, V. Dudr, S. Fabík, V. Chàb, K. Mašek, I. Matolínová, K. C. Prince, T. Skála, F. Šutara, N. Tsud, and K. Veltruská, “Activation of binary Zr-V non-evaporable getters: Synchrotron radiation photoemission study,” *Appl. Surf. Sci.*, vol. 243, no. 1–4, pp. 106–112, 2005.

[108] Ming Wu, S. Lemettre, D. Mansour, M. Plante, A. Bosseboeuf, S. Seok, and J. Moulin,

"Evaporated Zr-V, Zr-Ti and Zr-Co getter thin films: Activation temperature and microstructure," in *2016 Symposium on Design, Test, Integration and Packaging of MEMS/MOEMS (DTIP)*, 2016, pp. 1–4.

[109] F. Wang, R. Li, C. Ding, J. Wan, R. Yu, and Z. Wang, "Effect of catalytic Ni coating with different depositing time on the hydrogen storage properties of ZrCo alloy," *Int. J. Hydrogen Energy*, pp. 1–12, Aug. 2016.

[110] J. G. Bu, C. H. Mao, Y. Zhang, X. Y. Wei, and J. Du, "Preparation and sorption characteristics of Zr-Co-RE getter films," *J. Alloys Compd.*, vol. 529, pp. 69–72, 2012.

[111] A. Heidary Moghadam, V. Dashtizad, A. Kaflou, and H. Yoozbashizadeh, "Effect of rare earth elements on sorption characteristics of nanostructured Zr–Co sintered porous getters," *Vacuum*, vol. 111, pp. 9–14, Jan. 2015.

[112] T. Zhang, M. Zhang, R. Hu, H. Kou, J. Li, and X. Xue, "Hydrogen absorption behavior of a Pd-coated Zr70Fe5.4V24.6 getter material against gaseous impurities," *Vacuum*, vol. 122, pp. 222–229, 2015.

[113] C. Boffito, "A nonevaporable low temperature activatable getter material," *J. Vac. Sci. Technol.*, vol. 18, no. 3, p. 1117, Apr. 1981.

[114] F. Sciuccati, B. Ferrario, G. Gasparini, and L. Rosai, "In situ pumping with NEG (non-evaporable getters) during vacuum processing," *Vacuum*, vol. 38, no. 8–10, pp. 765–769, Jan. 1988.

[115] Y. Jin, Z. Wang, L. Zhao, P. C. Lim, J. Wei, and C. K. Wong, "Zr/V/Fe thick film for vacuum packaging of MEMS," *J. Micromechanics Microengineering*, vol. 14, no. 5, pp. 687–692, May 2004.

[116] G. Valdrè, D. Zacchini, R. Berti, a. Costa, a. Alessandrini, P. Zucchetti, and U. Valdrè, "Nitrogen sorption tests, SEM-windowless EDS and XRD analysis of mechanically alloyed nanocrystalline getter materials," *Nanostructured Mater.*, vol. 11, no. 6, pp. 821–829, 1999.

[117] P. B. Barna and M. Adamik, "Fundamental structure forming phenomena of polycrystalline films and the structure zone models," *Thin Solid Films*, vol. 317, no. 1–2, pp. 27–33, 1998.

[118] N. Stojilovic, E. T. Bender, and R. D. Ramsier, "Surface chemistry of zirconium," *Prog.*

Surf. Sci., vol. 78, no. 3–4, pp. 101–184, Jan. 2005.

[119] D. O. Northwood, "The development and applications of zirconium alloys," *Mater. Des.*, vol. 6, no. 2, pp. 58–70, 1985.

[120] R. D. Penzhorn, M. devillers, and M. Sirch, "Evaluation of ZrCo and other getters for tritium handling and storage," *J. Nucl. Mater.*, vol. 170, no. 3, pp. 217–231, 1990.

[121] Y. Oshida, E. B. Tuna, O. Aktören, and K. Gençay, "Dental implant systems," *Int. J. Mol. Sci.*, vol. 11, no. 4, pp. 1580–1678, 2010.

[122] I. Denry and J. Kelly, "State of the art of zirconia for dental applications," *Dent. Mater.*, vol. 24, no. 3, pp. 299–307, Mar. 2008.

[123] G. Abadias, L. E. Koutsokeras, A. Siozios, and P. Patsalas, "Stress, phase stability and oxidation resistance of ternary Ti–Me–N (Me=Zr, Ta) hard coatings," *Thin Solid Films*, vol. 538, pp. 56–70, 2013.

[124] D. A. Asbury, G. B. Hoflund, W. J. Peterson, R. E. Gilbert, and R. A. Outlaw, "TPD and ESD studies of the interaction of hydrogen and oxygen on polycrystalline zirconium," *Surf. Sci.*, vol. 185, no. 1–2, pp. 213–226, Jun. 1987.

[125] G. B. Hoflund, D. A. Asbury, D. F. Cox, and R. E. Gilbert, "An investigation of the interaction of polycrystalline zirconium with O_2, N_2, CO and N_2O. II. Pretreatment effects on O_2 chemisorption properties," *Appl. Surf. Sci.*, vol. 22–23, no. PART 1, pp. 252–258, 1985.

[126] G. B. Hoflund, D. F. Cox, and R. E. Gilbert, "An investigation of the interaction of polycrystalline zirconium with O_2, N_2, CO, and N_2O. Part I," *J. Vac. Sci. Technol. A Vacuum, Surfaces, Film.*, vol. 1, no. 4, p. 1837, May 1983.

[127] C. O. DE Gonzàlez and E. A. García, "Determination of the diffusion coefficients of oxygen in zirconium by means of XPS," *Appl. Surf. Sci.*, vol. 44, pp. 211–219, 1990.

[128] C. O. De González and E. A. García, "An X-ray photoelectron spectroscopy study of the surface oxidation of zirconium," *Surf. Sci.*, vol. 193, no. 3, pp. 305–320, Jan. 1988.

[129] T. Tanabe, M. Tanaka, and S. Imoto, "AES and XPS studies of oxygen stabilized alpha zirconium," *Surf. Sci.*, vol. 187, no. 2–3, pp. 499–510, Sep. 1987.

[130] A. Roustila, J. Chêne, and C. Séverac, “XPS study of hydrogen and oxygen interactions on the surface of zirconium,” *J. Alloys Compd.*, vol. 356–357, pp. 330–335, Aug. 2003.

[131] R. L. Tapping, “X-ray photoelectron and ultraviolet photoelectron studies of the oxidation and hydriding of zirconium,” *J. Nucl. Mater.*, vol. 107, no. 2–3, pp. 151–158, Jun. 1982.

[132] P. E. West and P. M. George, “An x-ray photoelectron spectroscopy investigation of the incorporation of surface oxides into bulk zirconium,” *J. Vac. Sci. Technol. A*, vol. 5, p. 1124, 1987.

[133] P. C. Wong, Y. S. Li, M. Y. Zhou, and K. A. R. Mitchell, “XPS investigations of the interactions of hydrogen with thin films of zirconium oxide I. Hydrogen treatments on a 10 Å thick film,” *Appl. Surf. Sci.*, vol. 89, no. 3, pp. 255–261, Jul. 1995.

[134] Y. S. Li, P. C. Wong, and K. A. R. Mitchell, “XPS investigations of the interactions of hydrogen with thin films of zirconium oxide II. Effects of heating a 26 Å thick film after treatment with a hydrogen plasma,” *Appl. Surf. Sci.*, vol. 89, no. 3, pp. 263–269, Jul. 1995.

[135] W. J. Peterson, R. E. Gilbert, and G. B. Hoflund, “The interaction of hydrogen with polycrystalline zirconium,” *Appl. Surf. Sci.*, vol. 24, no. 1, pp. 121–124, Jan. 1985.

[136] D. L. Cocke and M. S. Owens, “XPS evidence for facile formation of surface zirconium carbides from zirconium oxide overlayer decomposition and surface carbon,” *Appl. Surf. Sci.*, vol. 31, no. 4, pp. 471–476, May 1988.

[137] D. L. Cocke and M. S. Owens, “Reactivity of metal oxide overlayers: Formation of metal carbides,” *J. Colloid Interface Sci.*, vol. 131, no. 1, pp. 166–180, Aug. 1989.

[138] H. . Holmes, E. . Fuller, and R. . Beh, “Adsorption of argon, nitrogen, and water vapor on zirconium oxide,” *J. Colloid Interface Sci.*, vol. 47, no. 2, pp. 365–371, May 1974.

[139] Y. C. Kang, D. a. Clauss, and R. D. Ramsier, “Behavior of zirconium surfaces in the presence of oxygen, nitrogen, and hydrogen containing adsorbates,” *J. Vac. Sci. Technol. A Vacuum, Surfaces, Film.*, vol. 19, no. 4, p. 1996, 2001.

[140] N. H. Turner, “Surface Analysis: X-ray Photoelectron Spectroscopy and Auger Electron Spectroscopy,” *Anal. Chem.*, vol. 60, no. 12, p. 377R–387R, 1988.

[141] A. Einstein, “Concerning an heuristic point of view toward the emission and transformation

of light," *Ann. Phys.*, vol. 17, p. 132, 1905.

[142] J. W. Niemantsverdriet, *Spectroscopy in Catalysis: An Introduction: Third Edition*. 2007.

[143] T. L. Barr, *Modern ESCA: The Principles and Practice of X-Ray Photoelectron Spectroscopy*. CRC Press, 1994.

[144] S. Hofmann, *Auger- and X-Ray Photoelectron Spectroscopy in Materials Science*, vol. 49. Springer Berlin Heidelberg, 2013.

[145] D. Briggs and M. P. Seah, *Practical surface analysis: by auger and x-ray photo-electron spectroscopy*. John Wiley & Sons, 1983.

[146] N. Stojilovic, "Why can't we see hydrogen in X-ray photoelectron spectroscopy?," *J. Chem. Educ.*, vol. 89, no. 10, pp. 1331–1332, 2012.

[147] C. J. Powell and A. Jablonski, "Evaluation of Calculated and Measured Electron Inelastic Mean Free Paths Near Solid Surfaces," *J. Phys. Chem. Ref. Data*, vol. 28, no. 1, p. 19, 1999.

[148] A. Jablonski and C. J. Powell, "The electron attenuation length revisited," *Surf. Sci. Rep.*, vol. 47, no. 2–3, pp. 33–91, Jun. 2002.

[149] C. J. Powell and A. Jablonski, *NIST Electron Effective-Attenuation-Length Database - Version 1.3*. Gaithersburg, MD: National Institute of Standards and Technology, 2011.

[150] P. J. Cumpson and M. P. Seah, "Elastic Scattering Corrections in AES and XPS. II. Estimating Attenuation Lengths and Conditions Required for their Valid Use in Overlayer/Substrate Experiments," *Surf. Interface Anal.*, vol. 25, no. 6, pp. 430–446, Jun. 1997.

[151] K. Oura, M. Katayama, A. V. Zotov, V. G. Lifshits, and A. A. Saranin, *Surface Science*. Berlin, Heidelberg: Springer Berlin Heidelberg, 2003.

[152] F. M. Hoffmann and R. A. de Paola, "Anomalous C-O Bond Weakening of Side-On-Bonded Carbon Monoxide on a Potassium-Promoted Ru(001) Surface," *Phys. Rev. Lett.*, vol. 52, no. 19, pp. 1697–1700, May 1984.

[153] J. H. Scofield, "Hartree-Slater subshell photoionization cross-sections at 1254 and 1487 eV," *J. Electron Spectros. Relat. Phenomena*, vol. 8, no. 2, pp. 129–137, Jan. 1976.

[154] C. D. Wagner, L. E. Davis, M. V Zeller, J. a Taylor, R. H. Raymond, and L. H. Gale, “Empirical atomic sensitivity factors for quantitative analysis by electron spectroscopy for chemical analysis,” *Surf. Interface Anal.*, vol. 3, no. 5, pp. 211–225, Oct. 1981.

[155] C. D. Wagner, “Sensitivity factors for XPS analysis of surface atoms,” *J. Electron Spectros. Relat. Phenomena*, vol. 32, no. 2, pp. 99–102, 1983.

[156] A. M. Belu, D. J. Graham, and D. G. Castner, “Time-of-flight secondary ion mass spectrometry: techniques and applications for the characterization of biomaterial surfaces,” *Biomaterials*, vol. 24, no. 21, pp. 3635–3653, Sep. 2003.

[157] A. Benninghoven, “Chemical Analysis of Inorganic and Organic Surfaces and Thin Films by Static Time-of-Flight Secondary Ion Mass Spectrometry (TOF-SIMS),” *Angew. Chemie Int. Ed. English*, vol. 33, no. 10, pp. 1023–1043, Jun. 1994.

[158] K. Iltgen, “Optimized time-of-flight secondary ion mass spectroscopy depth profiling with a dual beam technique,” *J. Vac. Sci. Technol. A Vacuum, Surfaces, Film.*, vol. 15, no. 3, p. 460, May 1997.

[159] H. R. Verma, “Elastic Recoil Detection,” in *Atomic and Nuclear Analytical Methods*, Berlin, Heidelberg: Springer Berlin Heidelberg, 2007, pp. 143–175.

[160] J. F. Moulder, W. F. Stickle, P. E. Sobol, and K. D. Bomben, “Handbook of X-ray Photoelectron Spectroscopy.” Physical Electronics, Inc., p. 255, 1995.

[161] F. Schiettekatte, M. Chicoine, S. Gujrathi, P. Wei, and K. Oxorn, “Allegria: a new interface to the ERD program,” *Nucl. Instruments Methods Phys. Res. Sect. B Beam Interact. with Mater. Atoms*, vol. 219–220, no. 1–4, pp. 125–129, Jun. 2004.

[162] M. F. Sunding, K. Hadidi, S. Diplas, O. M. Løvvik, T. E. Norby, and A. E. Gunnæs, “XPS characterisation of in situ treated lanthanum oxide and hydroxide using tailored charge referencing and peak fitting procedures,” *J. Electron Spectros. Relat. Phenomena*, vol. 184, no. 7, pp. 399–409, Jul. 2011.

[163] G. Praline, B. E. Koel, R. L. Hance, H.-I. Lee, and J. M. White, “X-Ray photoelectron study of the reaction of oxygen with cerium,” *J. Electron Spectros. Relat. Phenomena*, vol. 21, no. 1, pp. 17–30, Jan. 1980.

[164] M. Romeo, K. Bak, J. El Fallah, F. Le Normand, and L. Hilaire, “XPS Study of the reduction of cerium dioxide,” *Surf. Interface Anal.*, vol. 20, no. 6, pp. 508–512, May 1993.

[165] K. Mašek, M. Václavů, P. Bábor, and V. Matolín, “Sn–CeO_2 thin films prepared by rf magnetron sputtering: XPS and SIMS study,” *Appl. Surf. Sci.*, vol. 255, no. 13–14, pp. 6656–6660, Apr. 2009.

[166] M. C. Biesinger, B. P. Payne, A. P. Grosvenor, L. W. M. Lau, A. R. Gerson, and R. S. C. Smart, “Resolving surface chemical states in XPS analysis of first row transition metals, oxides and hydroxides: Cr, Mn, Fe, Co and Ni,” *Appl. Surf. Sci.*, vol. 257, no. 7, pp. 2717–2730, Jan. 2011.

[167] E. Bêche, P. Charvin, D. Perarnau, S. Abanades, and G. Flamant, “Ce 3d XPS investigation of cerium oxides and mixed cerium oxide ($Ce_xTi_yO_z$),” *Surf. Interface Anal.*, vol. 40, no. 3–4, pp. 264–267, 2008.

[168] C. Morant, J. M. Sanz, L. Galán, L. Soriano, and F. Rueda, “An XPS study of the interaction of oxygen with zirconium,” *Surf. Sci.*, vol. 218, no. 2–3, pp. 331–345, Aug. 1989.

[169] R. Kaufmann, H. Klewe-Nebenius, H. Moers, G. Pfennig, H. Jenett, and H. J. Ache, “XPS studies of the thermal behaviour of passivated Zircaloy-4 surfaces,” *Surf. Interface Anal.*, vol. 11, no. 10, pp. 502–509, Jul. 1988.

[170] E. Fromm and G. Hörz, “Hydrogen, nitrogen, oxygen, and carbon in metals,” *Int. Met. Rev.*, vol. 25, no. 1, pp. 269–311, Jan. 1980.

[171] P. Delporte, F. Meunier, C. Pham-Huu, P. Vennegues, M. J. Ledoux, and J. Guille, “Physical characterization of molybdenum oxycarbide catalyst; TEM, XRD and XPS,” *Catal. Today*, vol. 23, no. 3, pp. 251–267, Mar. 1995.

[172] W. Ma, F. W. Herbert, S. D. Senanayake, and B. Yildiz, “Non-equilibrium oxidation states of zirconium during early stages of metal oxidation,” *Appl. Phys. Lett.*, vol. 106, no. 10, pp. 1–6, 2015.

[173] B. W. Veal, D. J. Lam, and D. G. Westlake, “X-ray photoemission spectroscopy study of zirconium hydride,” *Phys. Rev. B*, vol. 19, no. 6, pp. 2856–2863, Mar. 1979.

[174] M. N. A. Hall, S. L. H. Martin, and A. L. G. Rees, “The solubility of hydrogen in zirconium

and zirconium-oxygen solid solutions," *Trans. Faraday Soc.*, vol. 41, p. 306, 1945.

[175] G. Ertl and M. Huber, "Interaction of nitrogen and oxygen on iron surfaces," *Zeitschrift fuer Phys. Chemie (Muenchen, Ger.*, vol. 119, pp. 97–102, 1980.

[176] J. Holgado, G. Munuera, J. Espinós, and A. González-Elipe, "XPS study of oxidation processes of CeO_x defective layers," *Appl. Surf. Sci.*, vol. 158, no. 1–2, pp. 164–171, May 2000.

[177] N. Yamazoe, Y. Teraoka, and T. Seiyama, "TPD and XPS study on thermal behavior of absorbed oxygen in $La_{1-x}Sr_xCoO_3$," *Chem. Lett.*, vol. 10, no. 12, pp. 1767–1770, Dec. 1981.

[178] D. Teschner, E. M. Vass, and R. Schlögl, "Photoelectron Spectroscopy of Catalytic Oxide Materials," in *Metal Oxide Catalysis*, Weinheim, Germany: Wiley-VCH Verlag GmbH & Co. KGaA, 2009, pp. 243–298.

[179] A. P. Grosvenor, B. A. Kobe, and N. S. McIntyre, "Studies of the oxidation of iron by water vapour using X-ray photoelectron spectroscopy and QUASES^{TM}," *Surf. Sci.*, vol. 572, no. 2–3, pp. 217–227, Nov. 2004.

[180] H. Wiame, M.-A. Centeno, S. Picard, P. Bastians, and P. Grange, "Thermal oxidation under oxygen of zirconium nitride studied by XPS, DRIFTS, TG-MS," *J. Eur. Ceram. Soc.*, vol. 18, no. 9, pp. 1293–1299, Jan. 1998.

[181] A. Lyapin, "The initial stages of the oxidation of zirconium," University of Stuttgart, 2005.

[182] A. Denis, E. Moyano, and E. A. Garcia, "Model to simulate high temperature oxidation kinetics of zircaloy-4: parabolic and linear behaviour," *J. Nucl. Mater.*, vol. 110, pp. 11–19, 1982.

[183] M. Ozawa and M. Kimura, "Preparation and characterization of zirconium dioxide catalyst supports modified with rare earth elements," *J. Less Common Met.*, vol. 171, no. 2, pp. 195–212, Aug. 1991.

[184] S. J. Kerber, J. J. Bruckner, K. Wozniak, S. Deal, S. Hardcastle, and T. L. Barr, "The nature of hydrogen in x-ray photoelectron spectroscopy: General patterns from hydroxides to hydrogen bonding," *J. Vac. Sci. Technol. A Vacuum, Surfaces, Film.*, vol. 14, no. 3, p. 1314, May 1996.

[185] Y.-R. Luo, *Comprehensive handbook of chemical bond energies*. Boca Raton, FL: CRC Press, 2007.

[186] W. Arabczyk, E. Rausche, and F. Storbeck, "On the underlayer and overlayer adsorption of oxygen, nitrogen and carbon on the iron (111) surface," *Surf. Sci.*, vol. 247, no. 2–3, pp. 264–268, May 1991.

[187] M. Housley and D. A. King, "Coadsorption studies by Auger electron spectroscopy: Nitrogen with oxygen and carbon on W {100}," *Surf. Sci.*, vol. 62, no. 1, pp. 93–105, Jan. 1977.

[188] R. G. Palgrave, D. J. Payne, and R. G. Egdell, "Nitrogen diffusion in doped TiO_2 (110) single crystals: a combined XPS and SIMS study," *J. Mater. Chem.*, vol. 19, no. 44, pp. 8418–8425, 2009.

[189] S. Brumbach and M. Kaminsky, "Gas Release from Surfaces under X-Ray Impact: Photodesorption, Photocatalysis," in *Radiation Effects on Solid Surfaces*, Washington, DC: American Chemical Society, 1976, pp. 183–199.

[190] L. Mi, P. Xu, and P.-N. Wang, "Experimental study on the bandgap narrowings of TiO_2 films calcined under N_2 or NH_3 atmosphere," *Appl. Surf. Sci.*, vol. 255, no. 5, pp. 2574–2580, Dec. 2008.

[191] F. Peng, L. Cai, H. Yu, H. Wang, and J. Yang, "Synthesis and characterization of substitutional and interstitial nitrogen-doped titanium dioxides with visible light photocatalytic activity," *J. Solid State Chem.*, vol. 181, no. 1, pp. 130–136, Jan. 2008.

[192] H.-J. Freund and R. P. Messmer, "On the bonding and reactivity of CO_2 on metal surfaces," *Surf. Sci.*, vol. 172, no. 1, pp. 1–30, Jun. 1986.

APPENDICES

APPENDIX A EVOLUTION OF XPS SPECTRA OF POLYCRYSTALLINE ZIRCONIUM

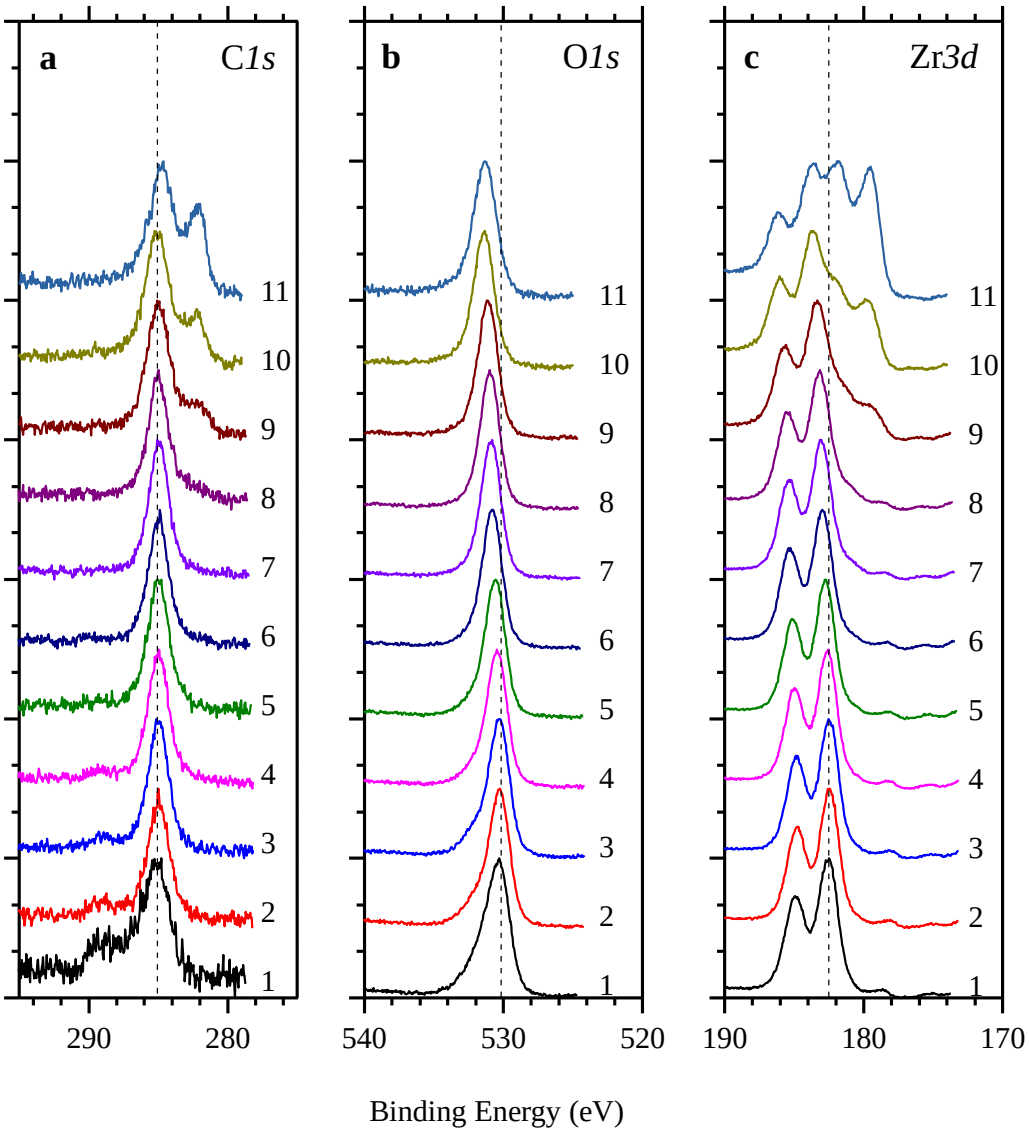

Evolution of high resolution XPS signal for (a) C1s, (b) O1s, (c) Zr3d for a polycrystalline Zr foil subjected to (1) 25 ºC, (2) 50ºC, (3) 100ºC, (4) 150ºC, (5) 200ºC, (6) 250ºC, (7) 300ºC, (8) 350ºC, (9) 400ºC, (10) 450ºC, and (11) 500ºC.

APPENDIX B

ARTICLE I: TEMPERATURE-DEPENDENT *IN SITU* STUDIES OF VOLATILE MOLECULE TRAPPING IN LOW TEMPERATURE-ACTIVATED ZR ALLOY-BASED GETTERS

Authors: *Zeinab Abboud and Oussama Moutanabbir*

Submitted to Journal of Physical Chemistry C, ACS Publications.

Abstract

The activation process and the gettering mechanisms of Zr-Co-rare earth metal alloy getters were investigated. The evolution of the surface composition prior to and upon exposure to volatile molecules (O_2, N_2, CO_2) was monitored *in situ* using X-ray photoelectron spectroscopy under annealing conditions compatible with low processing temperature regimes. The thermally activated process of surface oxygen diffusion into the bulk was elucidated and found to involve an activation energy of 0.21±0.02 eV in the 200-350^{o}C temperatures range. This activation process was also found to reversibly transform ZrO_2 into $Zr(OH)_2$ through the interaction with thermally desorbed hydrogen. Carbidic species form upon annealing at 250^{o}C via the interaction with adventitious carbon layer on the surface, which results in the decrease in the number of surface sites available for subsequent gettering. *in situ* studies of the material reactivity with high purity O_2, N_2, and CO_2 were also investigated. O_2 was found to saturate the surface after single exposure, while CO_2 dissociates into CO and O^-, where O^- is incorporated deeper in the material and CO forms an ad-layer on the surface of the getter. N_2 was found to weakly interact with the partially activated surface, and to form ZrN only upon annealing the sample to 350^{o}C indicating the poor reactivity of the material with N_2 at room temperature. The results display the importance of ridding systems of residual gases, especially N_2, by properly degassing the system prior to sealing to minimize and/or eliminate trapped gases within devices during operation.

Introduction

Developing materials for gas trapping and storage is of utmost importance for several technologies including; clean energy applications[1], noble gas separation[2], carbon sequestration[3], and removal of residual gases in vacuum cavities or chambers[4–7]. Such materials are very reactive and specifically designed with high porosity, nano- and micro-sized pores, to allow high gas sorption capacities[8,9]. Their functionality and gas selectivity can be tailored through material design and engineering for specific applications. Structural selectivity rises from the pore size distribution within the material that preferentially traps certain molecules; a behavior known as molecular sieving[10,11]. Chemical selectivity, on the other hand, originates from the nature of interaction

between impinging gas molecules and atoms present on the surface, which is governed by thermodynamics constraints[10]. Kinetics can also play an important role in selective interaction, where different gases have different diffusion rates depending on the adsorbent material[11]. Materials designed for gas trapping include metal-organic frameworks[12], carbon-based materials[13], polymeric networks[14], transition metal alloys[6], and alkaline earth metal alloys[5].

Transition and alkali earth metal alloys are used as getter materials for residual gas removal in vacuum chambers[6,7,15]. These materials are capable of sorbing a wide range of gases at room temperature. They are able to irreversibly trap O_2, N_2, H_2, CO, CO_2, H_2O, and hydrocarbons[15]. There are two main classifications of getter materials: evaporable (flashed), and non-evaporable (bulk getters). The former is composed of an alloy or pure metal (e.g. $BaAl_4$, Ti, Ni) in powder or bulk form, which is cyclically sublimated within the chamber, while the latter is deposited as a film of a few microns (<5 μm) in thickness and is often composed of transition metal alloys[15–17]. Flashed getters react with residual gases by sublimation (>1000ºC) and condensation on the inner walls of the vacuum chamber[16,18,19]. On the other hand, bulk getters are deposited prior to forming the vacuum cavity and are then thermally activated (<500ºC) to react with surrounding contaminants. Getters are used in sublimation pumps[18], ion pumps[20], accelerators[21], and microelectromechanical systems (MEMS) vacuum packaged devices[5,22–25].

Bulk getters were developed for vacuum chambers or cavities that are incompatible with the continuous evaporation of materials, and cannot withstand the high annealing temperatures at which flashed getters are sublimated (>1000ºC)[5,16,22]. Bulk getters are often integrated in vacuum packaged MEMS devices for maintaining proper operating conditions for the lifetime of the device (10+ years)[24,26]. The vacuum requirement varies depending on the application and ranges between 10^{-4}-225 Torr[22]. Considering a hermetically sealed cavity (i.e. no leakage), material outgassing would be the only source of pressure increase within MEMS cavities[27]. The material is generally sputter deposited on the cap wafer for wafer-level packaging prior to wafer bonding[22]. However, the material remains inactive due to the formation of an oxide layer on the surface upon exposure to ambient condition. The oxide acts as a passivation layer preventing further oxidation of the material and diffusion of gases to the bulk. Thus, the surface must be activated during or after formation of the microcavity. The activation process must also be compatible with the thermal budget required to maintain the device operation.

In order to activate the getter, the material is annealed to a critical temperature at which the oxide and other contaminants would diffuse into the bulk freeing up surface sites to interact with residual gases[16]. The activation temperature changes depending on the composition of the material, and can range between 200-400ºC[28–30]. The overall sorption capacity of the material is limited by the available surface area, which is dependent on the morphology of the thin film[21]. Bulk getters are mainly composed of zirconium due to its highly electropositive nature and

innate ability to dissolve its own oxides, carbides, and nitrides upon annealing[31–33].

Despite their technological importance, to the best of our knowledge, no detailed study has been conducted on the kinetics and the underlying mechanisms of gas trapping and surface contaminant diffusion into the bulk of a Zr-Co-REM getter material. *in situ* X-ray photoelectron spectroscopy (XPS) has been utilized to study the activation process of various getter materials due to its high surface sensitivity[34–43]. Bu *et al.*[44] investigated the sorption characteristics of the Zr-Co-REM getter on borosilicate substrate. They examined the effect of activation temperature, and substrate roughness on the pumping properties of the material. They found that with increasing substrate roughness, the sorption properties were improved due to an increase in the overall surface area and roughness of the deposited getter film. Petti *et al.*[43] and Xu *et al.*[26] investigated the influence of annealing temperature up to 450°C on the surface chemistry and microstructure from engineering and industrial perspectives. Petti *et al*. concluded that the Zr-Co-REM getter is activated at 300°C by reducing the ZrO_2 species to its metallic form and a segregation of Co towards the surface at 450°C. On the other hand, Xu *et al*. examined the effect of annealing temperature on the microstructure, as well as the resistance of the getter to various wafer cleaning processes by examining the getter's sorption characteristics [26]. Despite the recent efforts in providing a complete study of the gettering properties of the Zr-Co-REM alloy, a rigorous study of the physical and chemical characteristics of the alloy are still missing. The studies also lack an examination of trapping of common residual gases within MEMS cavities, especially N_2, since many industrial processes are conducted in an N_2 environment, increasing the partial pressure of N_2 within cavities. Therefore, it is of utmost importance to understand and quantify the ability of the Zr-Co-REM getter of trapping N_2, along with other volatile molecules.

In this paper we investigate, in detail, the thermal activation process of Zr-Co-REM getter and its interaction with O_2, N_2, and CO_2 molecules through *in situ* XPS studies. The aim is to describe, both qualitatively and quantitatively, the effect of low temperature activation (<350°C) on the surface composition, the kinetics of activation process, and the limitation of material reactivity with oxygen-free gases. Through *in situ* time-dependent studies, the activation energy for the diffusion of oxygen to the bulk of the material for getter activated at 200-350°C was approximated, and using controlled exposure experiments a qualitative mechanism of O_2, N_2, and CO_2 trapping is proposed.

Experimental details

Our investigations were performed on commercially available Zr-alloyed films sputtered on silicon wafers. Scanning electron microscopy (SEM) was used to examine alloy surface via Omicron NanoSAM system equipped with a UHV Gemini Column with a 15 kV accelerating voltage, operating at a base pressure of 10^{-10} Torr. To monitor the evolution of surface

chemistry upon heat treatment and exposure to gases, *in situ* X-ray photoelectron spectroscopy (XPS) studies were carried out using VG ESCALab 3MKII system, with a 300 W Al Kα source at an energy of 1486.6 eV and a spectrometer work function of 3.60 eV. The X-ray source was operated under an anode bias of 15 kV with an emission current of 20 mA. The UHV system consists of 3 chambers including a load-lock, a preparation chamber, and an analysis chamber, at base pressures of 10^{-4}, 10^{-9}, 10^{-10} Torr, respectively. *in situ* temperature dependent studies were conducted using a resistive heater and the temperature was measured using a thermocouple that is in direct contact with the sample holder. The estimated uncertainty in temperature measurement is approximately ±30ºC. Upon annealing, the pressure in the XPS analysis chamber would increase by an order of magnitude.

High energy resolution XPS scans were collected prior to each treatment. Scans spanning from 0 to 1400 eV were recorded at an energy step of 1 eV, a pass energy (E_{pass}) of 100 eV, and dwell time of 100 ms. High resolution spectra were collected for each element, with a resolution of 50 meV at E_{pass} energy of 20 eV and dwell time of 100 ms. An average over a minimum 9 scans is considered in these analyses in order to achieve a good signal to noise ratio for each high resolution scan. C*1s* core level orbital was used as a charge reference at a binding energy of 285±0.2 eV. The analyzed area is about 3×2 mm^2. XPS spectra were recorded and analyzed by means of Thermo Avantage v5.952 from Thermo Fisher Scientific. Shirley background subtraction was used for O*1s*, C*1s*, N*1s* XPS peaks, Smart background was used for the metal background subtraction, and relative sensitivity factors based on Wagner approximations were used for quantification of surface composition. Relative atomic composition is given in atomic %, which will be referred to hereon then as %, with an accuracy of ±1%. Handbook of X-ray Photoelectron Spectroscopy by Moulder *et al.* has been used as a main reference for the binding energies[45]. Values of 2.43 eV, 18.3 eV, 16.8 eV, and 15.2±0.2 eV were used for the spin orbit splitting for Zr*3d*, Ce*3d*, La*3d*, and Co*2p* orbitals, respectively[45].

To examine the kinetics of the activation process, different samples were heated under UHV in the XPS analysis chamber. Survey spectra were measured before subjecting the samples to annealing conditions, to have a baseline for the initial concentration of C, O, and Zr on the surface. The samples were then subjected to isothermal annealing, and XPS scans of Zr*3d*, C*1s*, and O*1s* orbitals were recorded. The area under the peaks was integrated to track the absolute change in the amount of Zr, O, and C present on the surface at a given time for each temperature. Each scan took 40 s to collect, and approximately 130 scans were recorded at each given temperature. The integrated area under the peak for O*1s*, C*1s*, and Zr*3d* were plotted as a function of time for each temperature and fitted accordingly. The analysis chamber is equipped with gas inlets, and valves that allow for the control of gas flow into the chamber. High purity gases were used for *in situ* studies O_2 (H_2O < 3 ppm, THC < 0.5 ppm), N_2 (H_2O < 3 ppm, O_2 < 2 ppm, THC < 0.5 ppm), and CO_2 (99.999% purity). Gases were introduced into the

analysis chamber up to a pressure of 10^{-5} Torr for various residence times at different temperatures. Exposure is given by Langmuir (L), that is 1L= 10^{-6} Torr s.

Time-of-flight secondary ion mass spectrometry (TOF-SIMS) analysis was performed using IONTOF TOF-SIMS IV, with Bi^+ as primary beam at 25kV (target current of 1.16 pA) and Cs^+ source for depth profiling at an energy of 3keV (target current of 20.13 nA). The sputter time/depth was calibrated by measuring depth of the 250×250 μm^2 crater using Veeco Dektak® 150 profilometer. TOF-SIMS data was acquired and analyzed using IONTOF Surface lab 6.2. Time-of-flight elastic recoil detection (TOF-ERD) analysis was carried out using I^{10+} with an energy of 55 MeV. TOF-ERD data was analyzed using Allegria, an ERD interface program[46]. The data was calibrated for depth by approximating the material density based on its constituents. The sensitivity limit in concentration is ±1 atomic %.

Results and Discussion:

1) Structure and chemical composition of the getter

Figure 11a displays representative SEM images of the as-deposited alloy surface. The material appears to be highly porous and nano-textured with average grain diameter between 20 and 100 nm. The large distribution of grains gives rise to a high active surface area of the getter. The thickness of the film has been measured using cross-sectional SEM and was found to be approximately 2 μm. EDX analysis shows the film is composed of 80% Zr, 15% Co, 5% traces of REM, including La, Nd, and Ce. The presence of REM has been reported to assist in the activation process of the getter, which will be discussed further in the following sections[43]. Shown in Figure 11b(inset), the O^- signal in TOF-SIMS drops an order of magnitude at an approximate depth of 70 nm, before it plateaus. The decrease in the O^- signal with increase depth is an artifact from the TOF-SIMS measurement. The high concentration of O^- within the "bulk" of the getter reflects the large active surface area of the material, such that there is an oxide passivation layer on the internal surface of the pores and grains within the material. The discrepancy between the thickness of the film measured with cross-sectional SEM (2 μm) and the thickness deduced from calibrated TOF-SIMS depth profile (~1.7 μm) due to a measurement artifact from TOF-SIMS. TOF-ERD (Figure 11c) measurement shows the atomic concentration profiles of the main components (Zr-Co) and the other impurities within the alloy. O concentration drops down from ~50% near the surface to ~20% beyond ~250 nm below the surface. Conversely, Zr content increases monotonically beyond a depth of ~250 nm due to the presence of ZrO_2 at the surface, and remains constant beyond this point. As for Co, its content is approximately 13.5 ± 0.4% within the material, with a slight depletion near the surface. The concentration of contaminants (N, H, and C) is negligible and remains below 2% across the analyzed thickness.

XPS analysis demonstrates that the surface (depth probed is approximately 4.7±1 nm) of the film is made up of 63.6% O, 18.3% Zr, 15% C, 2.4% Ce, and 0.8% La as shown in Figure 4.2a. Figure 4.2b-g shows a

representative set of XPS spectra recorded for as-deposited getter. Zr, and Co appear in their stable oxide states ZrO_2 and CoO, respectively, while La*3d5* at a binding energy of 835 eV, which has been reported to correspond to either hydroxide state $La(OH)_3$ or La_2O_3[45,47]. Ce is observed in its unstable oxide state as Ce_2O_3[48,49]. The presence of Ce^{3+} state indicates that it forms an intermetallic phase with other REM allowing Ce^{3+} to be stable at room temperature. Such behavior has been observed in $CeSnO_x$ intermetallic films, where Ce*3d* orbital displays a Ce^{3+} rather than Ce^{4+} oxidation state[50]. O1s orbital (Figure 4.2c) includes 3 peaks, at 529.7, 531.4, and 532.7 eV, which are attributed to metal oxides, metal hydroxides, and contaminant groups (carboxyl/alcohols), respectively. Co*2p* orbital has a shoulder at higher binding energy, which is associated with energy loss mechanisms (shake-ups)[51]. Ce*3d* orbital has multiplet splitting, which has been previously reported and also attributed to satellites and shake-up loss processes[52]. A summary of the details of the chemical species present on the surface of the getter with their relative quantities is presented in Table 5 column 1. The thickness of the oxide layer was approximated to be 2.4±1 nm using the attenuation length of the O*1s* signal in ZrO_2. However, this thickness would not be uniform on the surface of the material investigated in this work due to roughness and porosity. Details of the calculations of the oxide thickness can be found in the work by Morant *et al.*[53].

2) Activation process and its effects on surface composition

The Zr-Co-REM getter was developed for low temperature operating MEMS devices that cannot withstand processing temperatures exceeding 400ºC. 350ºC was selected as the target temperature for bonding and hence was used for our *in situ* analyses as the activation temperature of the getter. *in situ* monitoring of the surface composition evolution using XPS shows that as the temperature of the material increases to 350ºC, peaks corresponding to surface contaminants gradually diminish. However, C appears on the surface as carbidic species at 282 eV as shown in Figure 4.3a-spectrum #2. This observed formation of carbidic species upon heating Zr in the presence of hydrocarbons on the surface is in agreement with early reports on polycrystalline Zr[31,38,54–57]. Hydrocarbon decomposition at high temperatures on transition metals is known to result in incorporation of C into the metal and desorption of hydrogen as gas[58]. We also observe a wider peak with a full width half maximum (FWHM) of 3.2 eV at a binding energy of 283.8 eV attributed to a combination of oxycarbide groups on the surface, with residual hydrocarbons (Figure 4.3a-spectrum #4). The formation oxycarbide groups on metals has been observed previously by Delporte *et al.* where a flow of n-hexanes/H_2 mixture was introduced at 350ºC to a molybdenum oxide sample[59]. In their work, they reported a C*1s* peak at 283.5 eV associated to C bonded to a molybdenum oxide. Similarly, in this work, as the hydrocarbons dissociate into free C and H atoms, and as ZrO_2 is reduced to suboxide and metallic species, free C atoms would react with ZrO_x ($0<x<2$) to form ZrO_xC_y.

As the temperature increases, Co is reduced to a complete metallic phase (Figure 4.3d-spectrum #2), unlike La and Ce both of which remain in their oxide states. In parallel, Zr*3d* orbital evolves into 3 doublet groups (Figure 4.3c-spectra #2 and #3), with Zr*3d5* binding energies at 179.4, 180.5, and 183.4 eV. These doublet states represent the metallic/carbidic Zr^0/ZrC, non-stoichiometric suboxide ZrO_x, and ZrO_2, respectively[60,61]. The FWHM of the oxide states for Zr*3d5* increases from 1.6 eV at room temperature to 2.4 eV at 200 and 300ºC (Table 5-columns #2 and #3). This increase in FWHM can be attributed to an increase in disorder within the oxide matrix as opposed to the stoichiometric oxide initially present on the surface. The initial binding energy of Zr*3d5* for ZrO_2 appeared at 182 eV. After annealing, one of the doublet states for Zr*3d5* appears at a binding energy of 183.4 eV. This state was initially thought of to be ZrO_2, but have shifted from its initial position due to the oxide decomposition[57,62]. This peculiar behavior of O*1s* and Zr*3d* orbitals during the activation process will be addressed in more detail in the following section.

After activation at 350ºC, the alloy was cooled down to room in approximately 10 minutes. The surface was then exposed to 1.8×10^4 L of pure O_2 gas (10^{-5} Torr for 30 minutes). Subsequently, O_2 was evacuated and the surface composition was measured (Figure 4.3b, c-spectrum #4), both Zr*3d5* and O*1s* orbitals were found to shift back to 182.5 eV and 530.5 eV, respectively, with an increase in the percentage of stable oxide on the surface (ZrO_2) and a relative decrease in suboxides. Subsequent exposure to 1.8×10^4 L of O_2 had no significant impact on the surface composition. Dry oxidation resulted in a slight increase in the oxide and hydroxide levels (Table 5-columns #3 and #4). It has been shown that polycrystalline Zr surface is saturated upon exposure equivalent to 30-100 L of O at room temperature[31,53,63,64]. When the sample was stored in ambient atmosphere for one week, the surface did not revert to its initial state (see Table 5-column #6). However, the binding energies of Zr*3d* and O*1s* did revert to their original state, although a fraction of Zr shows carbidic traces, coupled with C*1s* carbidic species. Carbides were not present prior to activation and dry oxidation of the surface. It is also evident from the increase in the FWHM of the C*1s* 285 eV peak (Table 5-(columns #1 and #6)) that oxycarbide species are present on the surface after storing the sample in ambient conditions. The fact that the oxidation level was not completely recovered after exposure to ambient atmosphere can be explained by the formation of carbide species on the surface of Zr, which reduces the number of available adsorption sites that would otherwise be available to react with free O on the surface. The carbide poisoning of the surface was observed by Matolín *et al.*[35], where the aging mechanism of a Zr-V (58:42) getter surface was examined using XPS and SIMS. In their study, they repeatedly activated the getter *in situ* in XPS, and exposed it to air, and monitored the increase in carbide species on the surface of the getter. The repeated exposure to air led to the complete loss of the gettering ability of V after four cycles, thus impeding its overall capacity [35].

In order to elucidate the source of the shift in binding energy observed for both O*1s*

and Zr*3d* orbitals, a sample was heated *in situ* up to 350^{o}C in incremental steps of 50^{o}C. Since the activation process induces changes mostly in C*1s*, O*1s*, and Zr*3d* orbitals, high resolution spectra were only recorded for the 3 orbitals. Figure 4.4a-c shows the evolution of C*1s*, O*1s*, and Zr*3d* through thermal annealing up to 350^{o}C. The important observation from this set of data is the gradual shift in binding energy for Zr*3d5* (182 to 183.4 eV) as well as O*1s* (529.9 to 531 eV) from 25 to 350^{o}C. Charging is dismissed as a possible source for this shift, since the data have been adjusted for charging according to the binding energy of C*1s* up to 200^{o}C beyond which no charging effects were observed (Figure 4.4a-spectra #1-#5). Moreover, by monitoring the binding energy of C*1s* (285 eV) as a function of temperature (Figure 4.5a), it is noticeable that the peak associated with hydrocarbons does not shift, as opposed to O*1s* and Zr*3d* orbitals which experience shifts to higher binding energy with respect to room temperature spectra.

As the temperature increases, the first changes occur in the physisorbed alcohol/carboxyl groups that begin to desorb from the surface of the sample at 50 ^{o}C (Figure 4.4a, b-spectra #2). The shift in binding energy becomes apparent at about 150 ^{o}C (+0.46 eV for O*1s*, +0.42 eV for Zr*3d*), after which a new doublet state for Zr*3d* orbital appears corresponding to ZrC or ZrC-O or ZrH_x[42,43,45,55,60,61,65]. At 200 ^{o}C, the shift reaches +1.0 eV for both orbitals and increases further to about +1.5 eV at 250 ^{o}C with the dissolution of oxides into the bulk, and increase in the carbide and oxycarbide species. Figure 4.4a-c and Figure 4.5a show the gradual shift in binding energy for both O*1s* and Zr*3d* orbitals, while C*1s* binding energy is constant up to 250 ^{o}C until the dissociation of surface hydrocarbons becomes significant resulting in the formation of carbide/oxycarbide complexes with Zr. The shift has also been observed with a polycrystalline Zr foil sample that has been subjected to higher annealing temperatures (supplementary information).

One may invoke several pathways to explain the observed shifts. Initially, as the temperature increases to 100^{o}C, trapped H_2 molecules within the pores and the bulk of the material tend to desorb, and as the oxide layer is dissociated, some of the H_2 molecules would thermally dissociate and react with ZrO_x species forming hydroxide species. It has been observed that Zr based materials, as well as pure polycrystalline Zr trap H_2 molecules at temperatures as low as 25^{o}C, granted the surface if O-free[66]. H_2 desorption from polycrystalline Zr has been measured using temperature programmed desorption (TPD) method[63,67,68]. It was found that H_2 desorption peaks at 230 ^{o}C for polycrystalline Zr sample[63]. Asbury *et al.* examined the influence of the presence of an oxide on the surface of a polycrystalline Zr sample on H_2 desorption[63]. They gradually increased the O concentration on the surface of Zr by controlling the dosage, and measured the intensity of the H_2 TPD peak at 230 ^{o}C as a function of O concentration on the surface. They concluded that a higher surface O concentration increases the desorption of H_2 from the bulk of the material[63]. Peterson *et al.* observed that the presence of O on the surface of Zr induces a H_2 desorption peak at 230 ^{o}C, which is not present with an O-free Zr[67]. TPD analysis has also been performed on a Zr-

based getter, and hydrogen desorption was initiated at approximately 200 ^{o}C[69]. Our observations agree with these findings, where the shift in ZrO_2 and O*1s* orbitals to higher binding energy corresponds to metal hydroxide. This shift becomes significant at 250^{o}C, when the binding energy of the initial ZrO_2 (Zr*3d5*=182 eV) moves to 183.5 eV, which can be attributed to the presence of $Zr(OH)_2$ species [61]. The doublets at 181.2 eV and 179.8 eV are associated with ZrO_x ($0<x<2$) and ZrC-O/Zr-C and some metallic species, respectively. Transition metal hydroxide species have been reported to have a higher binding energy compared to their stable oxide states as has been observed by Biesinger *et al.* [51]. Moreover, the broadening of the peak as indicated by the increase in the FWHM (as shown in Table 5), is associated the increase in inhomogeneity of the species present on the surface. Thus, the peak at 183.4 eV (Zr*3d5* at 350^{o}C) would represent a non-stoichiometric $Zr(OH)_2$. Subsequently, when the activated sample was exposed to a controlled O atmosphere (as shown in Figure 4.3b, c-spectra #4 and Table 5-column #4), the binding energy shifted back to its original value. This observation points to either the formation of full oxide layer on top of a hydroxide layer or the decomposition of hydroxide species into H^+ and O^- to form H_2 upon O_2 chemisorption. Indeed, it has been shown that dissociative chemisorption of O_2 molecules on metal surfaces at room temperature is an exothermic reaction leading to the decomposition of chemical species on the surface and migration of their ions to deeper layers within the material[70].

It is noteworthy that similar shifts in the binding energy of Zr*3d* and O*1s* was reported by Li, Wong, and Mitchell in their *in situ* studies of a ZrO_2 thin film deposited on Au foil in a H_2O rich environment[61]. Their Zr*3d5* corresponding to ZrO_2 was initially at 182.9 eV, and after heating the sample to 500^{o}C in UHV, this binding energy shifted to 183.4 eV. They have attributed this shift to desorption of H_2 trapped within the grain boundaries of polycrystalline Zr, and the formation of hydroxide species at 183.4 eV[61]. Moreover, they reported that exposure of activated sample to oxidizing conditions reverts Zr*3d* to its original position, consistent with our results. Mašek *et al.* have also reported a similar shift in a Zr-V alloy getter as the sample was heated incrementally to 320^{o}C[37]. They observed a shift to higher binding energies for Zr*3d*, V*2p*, O*1s*, including C*1s*, which they attributed to the Fermi level shift as a result of oxide reduction[36,37].

The O*1s* peak has a shoulder that evolves throughout the activation process (Figure 4.4b). Initially the peak is observed at 531.6 eV, which corresponds to hydroxide species. This peak slowly merges into the main peak as $Zr(OH)_2$ forms and becomes the dominant state in O*1s*. A small peak however is still present at 150^{o}C, at 532.3 eV, and shifts towards 533.2 eV at 250^{o}C. The shift in binding energy for this peak with respect to room temperature is shown in Figure 4.5a-(O1s-M-OH). As the oxide and hydroxide species are dissociating at the surface, the O^- ions become mobile on the surface and within the grain boundaries and pores of the material, which increase their binding energy compared to lattice oxides O^{2-}. O-related defects in metal oxide surfaces have been detected at a binding energy of 532 eV[51,71–73].

The thermally activated process of O^- hopping from a lattice site to an interstitial site weakens the electron screening of the Coulombic attraction of the atomic species, increasing the binding energy of the photoelectron[74]. It is difficult to distinguish these O defect states from defective hydroxyl groups, which can also occur at this binding energy, for unstable hydroxyl groups on metal surfaces. Stable oxide states would be located at a lower binding energy for O*1s* orbital (<530 eV), while oxide or hydroxide defects hydroxide groups would appear at higher binding energies due to a reduced displacement of the electron density with respect to stable oxide species[73,75]. Physisorbed OH^- and H^+ ions would react resulting in the formation of physisorbed H_2O. This is evident by the presence of the 533.2 eV peak at 250^{o}C (Figure 4.4b-spectrum #6)), which corresponds to physisorbed H_2O on the surface[75,76].

3) Kinetics of the getter activation

The activation process is defined by the amount of O that diffuses/dissolves into the bulk, freeing up adsorption sites in the alloy surface for impinging gases. It is evident from Figure 4.5 (b) that 230^{o}C is the onset of activation, where O content decreases drastically. Therefore, in order to elucidate the physical and chemical phenomena involved in the getter activation further, the kinetics this process was investigated. Samples were heated separately to 200^{o}C, 250^{o}C, 300^{o}C, 330^{o}C, 350^{o}C, and the integrated area under the O, C, and Zr-related peaks were plotted as a function of annealing time. Figure 4.6a-c shows the evolution of the XPS signal of C*1s*, Zr*3d*, and O*1s* as a function of time and temperature. C*1s* signal initially decreases due to contaminant desorption, and then the concentration increased ever so slightly with oxide decomposition, and carbide formation (Figure 4.6a). The most significant change occurs in the O signal, which in turn influences the relative quantity of Zr on the surface. The attenuation of the O signal follows an exponential decay at an early stage (<800s) before showing a very slow, linear decrease with time. Both exponential and linear behaviors of diffusion of O into polycrystalline Zr have been observed on different time scales. Foord *et al.* observed an exponential decay in the O peak measured by Auger electron spectroscopy (AES) as polycrystalline Zr was heated *in situ* to 340^{o}C over a 160 s interval[31]. They associated the exponential decay of the O signal with the diffusion of O from the surface to the bulk forming a concentration gradient within the material. On the other hand, West and George reported a linear behavior for the integrated XPS peak intensity of O in polycrystalline Zr between 0-70 minutes[77]. West and George explained the linear behavior of the O signal attenuation with an "interface-controlled reaction", where the suboxide at the Zr-ZrO_2 interface acts as a diffusion barrier for O^- ions from the oxide to the metal side. The results presented in Figure 4.6c display both behaviors, indicating two limiting processes taking place in different time scales. Initially, as the sample is rapidly approaching the indicated temperature, oxide layer begins to decompose and O^- migrate into the bulk. This is a diffusion-limited process. Subsequently, a steady-state is reached at approximately 1000s, as shown in Figure 4.6e for O*1s* signal attenuation at 250 ^{o}C. The time-independent

process could be associated with the incorporation of diffused O into the bulk. As the O is increasingly diffusing into the bulk, driven by the gradient of concentration, the mobile O^- begins to incorporate into the Zr matrix. West and George have attributed the steady state behavior to the presence of a diffusion barrier that prevents O species from diffusing into the bulk of Zr from ZrO_2. The barrier is in the form of a non-stoichiometric interface develops between the oxide and the metallic phases, which has been proposed as a model for the formation of stable oxides on Zr surfaces[60,77–79].

The time constant (τ) for the attenuation of the O signal on the surface of the getter as a function of temperature are summarized Table 4.2. As the temperature increases from 200 to 350ºC, the time constant decreases from 360 to 106 s, indicating a faster decomposition and migration of the oxide from the surface and into the bulk of the material. The enhanced oxide decomposition is also evident in the significant decrease in oxide thickness as the temperature increases to 350ºC (Figure 4.6f). A more than 50% decrease in oxide thickness is obtained at 200 s when the sample is heated to 350ºC. The reduction in oxide thickness is not as pronounced at temperatures below 300ºC, where the thickness remains above 50% of its original value after reaching steady state. Activation energy for the diffusion of O ions into the bulk was extracted from the Arrhenius plot (Figure 4.6d). The activation energy of the diffusion process was found to be 0.21 ± 0.02 eV. Foord *et al.* have extracted the activation energy of 0.52 eV for O dissolution in polycrystalline Zr at temperatures between 200-350ºC via *in situ* AES experiments[31]. Other groups have also estimated the activation energy and diffusion coefficients of O in Zr, however, they were in a higher temperature regime (>400ºC)[80]. The activation energy extracted in this work is significantly smaller than that reported by Foord *et al.*[31] due to compositional and morphological differences between polycrystalline Zr and Zr-Co-REM getter investigated in this work. The presence of large pores within the getter structure facilitate the migration of O^- to the bulk of the material, in contrast to polycrystalline Zr, where grains are significantly larger and there are fewer grain boundaries.

Figure 4.6a displays the stability of the carbide species that forms on the surface. The fact that annealing temperature and time has no effect on C signal indicates that carbide is substitutional rather than interstitial. This is further supported the FWHM of carbide peak which is 1.2±0.1 eV, whereas that of the oxide peak 2.3±0.1 eV. The larger FWHM of oxide peak in the alloy, as well as the attenuation of the O signal as a function of time and temperature, and its higher binding energy (>530 eV) indicate that O is an interstitial rather than a lattice oxide. Lattice-oxides are often detected at lower binding energy (O*1s* < 530 eV) due to improved electron transfer from O^{2-} to Zr^{4+} and enhanced electron screening[74]. In polycrystalline Zr, both carbide and oxide form interstitial compounds, which allows the material to dissolve both contaminants in similar manner[31]. As a result, decomposition of carbonaceous compounds on the alloy poisons the surface and renders the adsorption sites occupied by C unavailable for subsequent adsorption.

Since XPS data can only provide information regarding the changes that occur on the surface, *ex situ* TOF-ERD analysis was utilized to examine the changes of O concentration within the bulk of the material. Two samples were analyzed, one which was unprocessed (control sample), and the other sample was annealed in rapid thermal annealing (RTA) under inert conditions (Ar, 1 atm) for 30 minutes at 400^{o}C, and cooled down to room temperature under the same atmosphere. The annealed sample was then transferred to the TOF-ERD system under ambient conditions. As shown in Figure 4.7a, b, the O content within the bulk of the material increases from 25% to 45% post annealing. The concentration profile post anneal is also more uniform compared to the untreated sample. The change in the profile is due to the diffusion of the O species present on the surface, which results in the smearing-out of the concentration profile within the bulk. The activation not only drives the O to diffuse from the topmost layers to deeper layers, it also drives the O within the pores (internal surfaces) to incorporate within the metallic matrix. As a result, the pores act as both a facile transport path for O ions from the surface, and as active gettering sites when exposed to gas.

4) Oxygen trapping

So far, we examined the reactivity of the alloy with O at room temperature, as shown in Figure 4.3a-f-spectra #4 and Table 5-column #4. Investigating the gas-alloy interaction at elevated temperatures would give insight on the competition between adsorption and diffusion processes. To this end, a sample was annealed *in situ* to 350 ^{o}C under UHV (<10^{-9} Torr), and O_2 gas was introduced into the chamber at a pressure of 10^{-5} Torr for 50 min, the sample was then cooled down to 25 ^{o}C under UHV to examine the surface composition via XPS. It is worth noting that prior to introduction of O_2 into the chamber; there was a delay of ~5-10 minutes in order for the sample to reach 350 ^{o}C. Figure 4.8a-f, show the spectra for the sample prior (1) and post high temperature oxidation conditions (2). From a qualitative point of view, Zr*3d* and O*1s* show the previously observed shift in binding energy, to a lesser extent, where Zr*3d5* appears at a binding energy of 182.9 eV, and O*1s* 530.9 eV, after the high temperature oxidation (1 eV above baseline measurement). In contrast to the previous experiment, Zr*3d* and O*1s* orbitals reverted to their initial binding energy position after exposure to O_2 *in situ* at room temperature (see Table 5 for details).

High temperature oxidation involves three processes: 1) the reduction of pre-formed oxide on the surface, 2) the dissociative adsorption of O_2 molecules impinging at the surface, and 3) the diffusion and incorporation of O^- ions into the bulk. Initially as the temperature is approaching 350^{o}C, the O concentration reaches 36% of its saturation point after 106 s (from diffusion measurements), thus freeing up adsorption sites for impinging molecules on the surface. After dosing the surface with O_2, O_2 molecules dissociate at the free sites on the surface and O^- ions diffuse into the bulk. The rates of adsorption *vs*. diffusion determine the level of oxidation on the surface and within the bulk of material. Quantitative analysis of the surface composition shows that the initial level of metal oxides (at binding energy of

529.7eV) is ~43% and metal hydroxides (531.5eV) ~18% (Table 4.3-spectra #1 and #2). After exposing the sample to O_2 at 350°C, the surface is composed of a defective layer of mixed oxide and hydroxide species appearing at a binding energy of 530.9 eV amounting to 47%. The fact that the O concentration on the surface of the getter remained approximately constant post treatment indicated that the rate of chemisorption of O_2 is faster than the rate of diffusion of O^- ions into the bulk. This is true under these high dosing conditions (3×10^4 L). If lower doses were imposed, the level of oxide would not reach saturation point. This was observed by Vedel and Schlapbach, where they investigated the oxidation of a Zr-V-Fe (14:5:1) alloy getter at 25, 225, and 425°C[42]. High temperature oxidation with low doses of O_2 (<100 L) was found to have no effect on the surface, where the alloy maintained its metallic state, while doses between 100-1000 L resulted in a sub-oxide formation on the surface[42].

Simultaneous oxidation and diffusion of O^- ions into the bulk results in the formation of non-stoichiometric oxide/hydroxide complexes. As a result, Zr*3d5* and O*1s* states appear at a binding energy, with a higher FWHM compared to their initial state (1.9 eV vs. 1.6 eV for Zr*3d*) which is further proof of the disordered state of the oxide present on the surface of the getter (Table **4.3**- columns #1 and #2). Moreover, the introduction of O at high temperature increased the amount of oxycarbides compared to carbides, with a ratio of ~6:1, while room temperature oxidation resulted in ~2:1 ratio. The FWHM is, however, the same for both treatments (see Table **4.3**). Other orbitals corresponding to REM Figure 4.8f show the stability of lanthanides despite various treatments. On the other hand, a slight change appears in Co*2p* orbital, where cobalt is reduced from its stable oxide state (CoO) to a non-stoichiometric oxide CoO_x (x<1) under high temperature oxidation. La, Ce, and Nd are more electropositive compared to Zr with electronegativity values of 1.1, 1.12, 1.14, and 1.33, respectively[81]. It has been observed with alloys that involve metals with different electronegativies that the more electropositive species tends to be reduced at higher temperatures compared to more electronegative species[15,37,39]. In Zr_xV_{1-x} alloys, higher V content has been shown to lower the activation temperature of the getter, where ZrV_2 has the lowest reported temperature of most alloys used as getter materials due to the more electronegative nature of V compared to that of Zr[39]. This behavior was also observed in a TiFe alloy where Ti, the more electropositive species, remains oxidized during the thermal activation process while Fe is completely reduced at 350°C[39]. In Zr-Co-REM alloy, Petti *et al*. correlated the thermal stability of lanthanide oxide states to the fact that they participate in the activation process, where O attaches to REM during the diffusion process[43]. Ozawa and Kimura[82] have examined the role of modifying ZrO_2 catalyst supports with REM, and they observed an enhanced catalytic activity for CO with the addition of 10 mol.% REM into the material. However, the experimental proof on the role of REM in the activation process of the getter is not compelling and further studies are required to establish their specific behavior in the activation and gettering process. Specific

studies must address if the REM play a significant role in assisting the reduction process, where a Zr-Co behavior would be compared to its REM counterpart, while taking into account the variations in the microstructure and their role in the activation process.

5) Nitrogen Trapping

N_2 is often used in various microfabrication processes, and thus can often be trapped during material and device processing and can be later outgassed, which can limit the device performance and lifetime. N_2 gettering is therefore important for maintaining a proper environment for normal device operation. The getter reactivity with N_2 was examined at both room temperature and high temperature. A getter sample was activated at 350ºC as previously described, and exposed to N_2 at pressure of 10^{-5} Torr for 30 min at 25ºC. XPS showed no evidence of N-related compounds on the surface. Subsequent exposures to N_2 room temperature for extended time (up to 20 hours at same base pressure) were found to be futile in inducing a reaction on the surface of the getter. However, when N_2 was introduced at high temperature (350ºC for 50 min at 10^{-5} Torr), a peak appeared at 396.9 eV corresponding to N*1s* (Figure 4.8c-spectrum #4). N*1s* peak appears on the surface as nitride corresponding to ZrN at its low binding energy and amounting to 3.5% of surface content[83]. These results indicate that N_2 gettering is a thermally activated process. The low reactivity of the getter alloy with N_2 can be attributed to the presence of pre-adsorbed O on the surface, which renders the surface N_2 inactive. Room temperature dissociative chemisorption of N_2 molecules on metal surfaces occurs if the N-metal bond is larger than 5.12 eV, equivalent to half of the bond energy within a single N_2 molecule[84]. The dissociation energy of the Zr-N bond is on the order of 5.9±0.3 eV, thus theoretically, N_2 would readily react with Zr surfaces[85]. Foord *et al.*[31] and Hoflund *et al.*[86] observed N_2 reaction with Zr at room temperature. Foord *et al.* studied the kinetics of adsorption and absorption of N_2 and NO molecules in polycrystalline Zr via AES[31]. They determined the activation energy of diffusion of N into the bulk by monitoring the attenuation of N Auger signal as a function of time, which was determined to be 0.6 eV.

Foord *et al.* also examined the effect of pre-adsorbed species, specifically O, on the adsorption of N at room temperature. They found the presence of O on the surface of Zr significantly influences N_2 adsorption. Through controlled experiments, they concluded that N chemisorption on Zr would only occur if the amount of pre-adsorbed O were less than 30% of its saturation point. Conversely, the presence of N on the surface has little or no influence on the adsorption of O[31]. N was then considered to form an underlayer, which was also observed on Fe by Ertl and Huber[70] using AES and modeled by Arabczyk *et al.*[87]. Ertl and Huber proposed that the reaction of Fe with O is exothermic, releasing enough energy to displace N atoms to deeper layers. Similar behaviour was observed by Housley and King on W (100) surface[88]. In their study, N-saturated W (100) surface underwent controlled oxidation conditions, and the AES signal of both N and W were found to be attenuated. They concluded that N adatoms were buried in

deeper layers due to the formation of an electric field between the W, W-N and chemisorbed O, which drives W^+ to diffuse towards O^- [88].

To investigate N_2 dissociative chemisorption further on the Zr-Co-REM alloy, the following experiment was conducted. First the sample was activated at 350°C, activation is evident by the significant drop in O intensity as displayed in Figure 4.9a-spectrum #2. The sample was then cooled down and dosed with 1.2×10^4 L of N_2 at 25 °C. No N-related compounds were detected after N exposure at room temperature, as has been observed previously (Figure 4.9b, c-measurement #4). The sample was then annealed at 350°C under UHV after which N*1s* peak was detected (Figure 4.9b, c-measurement #5). The N-exposure and annealing cycle was repeated several times to monitor the evolution of N*1s*. Zr*3d* and C*1s* intensities remain roughly constant, whereas, O*1s* intensity tends to fluctuate, but stays within the same order of magnitude after the initial drop due to the activation process (Figure 4.9a). The main observation in Figure 4.9c-measurement #5, is the detection of N-species on the surface only after annealing the sample that was previously dosed with N_2 at room temperature. By repeating the cycles of sample exposure to N_2 at 25°C and annealing at 350°C, we see a gradual increase in the N*1s* intensity (Figure 4.9c). After the first annealing step (Figure 4.9b, c-treatment #5), the N*1s* peak observed is located at a binding energy of 397 eV and a FWHM of 1.5 eV. N*1s* at this binding energy is correlated with substitutional N in an oxide matrix[89]. After cooling down the sample, the intensity of N*1s* remains roughly unchanged. Unexpectedly, N increases in intensity after exposing the sample to N_2 at room temperature in the second cycle (Figure 4.9c-measurement #7). This behavior was repeatedly observed in following cycles, except for measurement #10, where the sample was stored under UHV for 12 hours, which allows for contaminants (hydrocarbons) within the chamber to adsorb on the surface. In order to explain the increase N content on the surface of the alloy following these treatments, we propose the following mechanisms.

Exposing the alloy surface to N_2 at room temperature allows for a certain amount of N_2 molecules to physisorb onto the surface, and within the pores of the material. When irradiating the sample with X-rays during the measurements, molecules on the surface gain enough energy to desorb. Thus, after the first dose of N_2 at room temperature, no N-related species were detected on the surface. Photoinduced gas desorption from stainless steel and Al_2O_3 surfaces has been observed for various gases [90]. On the other hand, N_2 molecules physisorbed within pore sites may re-adsorb on a different pore site post X-ray irradiation. Upon annealing the sample, the trapped N_2 molecules obtain enough thermal energy to hop from one adsorption site to another, and dissociate into N^- ions and bind to available sites forming nitrides on the surface. It is also possible that N_2 molecules would dissociate within the pores at room temperature, however, due to the limitation of XPS, these sites cannot be probed.

After the initial annealing cycle, it is observed that N_2 dosing at room temperature results in increase in N content on the surface (Figure 4.9c-measurements #7, 13, 16)). This

increase in N content is coupled with the appearance of a shoulder in N*1s* orbital at a binding energy of 399.4±0.2 eV and a FWHM of 3.5 eV (Figure 4.9b-spectra #7, 13, and 16). This new N*1s* mode is correlated with the presence of adsorbed NO molecules, or interstitial N[89,91,92]. It is difficult to correlate the 399.2 eV peak to a single species. The fact that the FWHM is so large (3.5 eV); it is more likely that it represents a combination of weakly adsorbed interstitial (or surface) molecules/atoms. This indicates that the presence of chemisorbed N on the surface act as nucleation sites for the adsorption and dissociation of N_2 molecules on the surface. The decrease of N intensity after annealing the sample at 350^{o}C (see Figure 4.9b, c-measurements #11, 14, and 17)) is attributed to the diffusion of chemisorbed N and interstitial N to the bulk of the material. Note that there is a gradual increase in N intensity with increasing number of cycles Figure 4.9c-measurements #6 and #18. This increase indicates that there is an accumulation of N on the surface as the number of cycles increases, which supports our hypothesis of the trapping mechanism of N_2 within the alloy at room temperature.

6) CO_2 Trapping

We also investigated the reactivity of the material with CO_2. As with the previous studies, the sample was initially activated at 350^{o}C, and then exposed to CO_2 (1.8×10^4 L) at 25^{o}C. The evolution of the XPS spectra are shown in Figure 4.10 for C*1s* (a), O*1s* (b), and Zr*3d* (c). Exposing the activated alloy surface to CO_2 results an increase in intensity of the 285 eV peak in C*1s* orbital (Figure 4.10a-spectrum #3) accompanied by a slight broadening of the O*1s* peak (Figure 4.10b-spectrum #3). However, no significant change was observed in Zr*3d* orbital. The increase in the C*1s* 285 eV mode is associated with metal-CO bonds, which is consistent with the increase in the 532 eV peak associated with O*1s* orbital. Semi-quantitative analysis shows that metal hydroxide/oxide species surprisingly decreased on the surface (Table 4.4). This result was unexpected, since CO_2 interaction with transition metals often results in dissociation of the molecule into CO and O[93]. Thus one would expect an increase in the oxide content at the surface. The attenuation of both O*1s* and Zr*3d* signals (Table 4.4-column #3) indicates a shadowing effect. Angle-resolved XPS (ARXPS) measurements were then utilized to understand the source of this decrease in the signal. Shown in Figure 4.10a-c (3-6), the signal evolution as the take-off angle was varied from 0-80^o with respect to the surface normal. By increasing the take-off angle, the XPS signal would be more sensitive to the top-most surface layers. Figure 4.10b-spectrum #6 shows the O*1s* signal measured at a take-off angle of 80^o, where the shoulder at binding energies of 532 and 533 eV are accentuated compared to 0^o signal. This indicates that CO and CO_2 molecules are physisorbed on the surface burying the oxide species underneath (Table 4.4-columns #3 and #6).

Reannealing the sample at 350 ^{o}C displayed a decrease in the higher binding energy peaks in C*1s* and O*1s* orbitals (Figure 4.10a, b-spectra #7 and #8). This result indicates that upon annealing, physisorbed CO and CO_2 molecules either desorb or

incorporate into the material. However, no increase in carbide formation was observed, which reveals that hydrocarbons are the sole source of carbide species. Therefore, we postulate that CO would not decompose further into C and O species. Foord *et al.* has shown that CO molecules occupy a single adsorption site[31]. In addition, the lack of evidence for the increase in oxide content means that O^- resulting from CO_2 decomposition would preferentially diffuse to deeper layers than react with available surface sites, which would be populated with CO molecules instead.

Conclusions

This work investigated gas trapping mechanisms in a Zr-Co-REM alloy getter designed for MEMS cavities. SEM analysis showed the porous nature of the getter with nanocrystalline grains that range between 20-100 nm in size. The bulk of the getter is composed of 80% Zr, 15% Co, and 5% of rare-earth metals (Ce, La, Nd) as displayed by EDS analysis. On the other hand, XPS analysis showed that O makes up 60% of the surface composition. The O content on the surface of the getter is mainly in the form of metal oxides, where ZrO_2 is the dominant surface component. *in situ* thermal activation at 350^{o}C showed the partial activation of the surface, where the O composition decreased to 27%, such that ZrO_2 was reduced to ZrO_x and Zr^0. The annealing process was found to partly transform ZrO_x to $Zr(OH)_2$ by interacting with H_2 that out-diffused from the bulk of material evident by the shifting of the binding energy Zr3d and O1s orbitals to higher binding energy (up to 1.4 eV). The activation process also converted the adventitious carbon layer to carbides, where C from hydrocarbons spontaneously bonded to reduced ZrO_2 forming a ZrC compounds. Time dependent *in situ* XPS studies showed that O diffusion from the surface to the bulk requires an activation energy of 0.21eV indicating the essential role of the pores and the grain boundaries in facilitating O diffusion away from the surface.

Controlled exposure of the partially activated surface to N_2 at room temperature was found to have no observable change in the composition of the surface; however, upon annealing the surface after a single exposure to N_2 at room temperature, nitrides were detected on the surface. This peculiar behavior was associated with the weak trapping of N_2 within the pores of the material, beyond the detection limits of the XPS instrument, and the surface-diffusion of N-species within the pores and grain boundaries upon annealing. Thus, Zr-Co-REM was found to have a poor gettering capacity for N_2, and for technological applications, N_2 must be eliminated from device processing to avoid build-up of N_2 pressure post bonding of MEMS cavities. On a device level, in our case, the 350^{o}C was selected due to its compatibility with the bonding process, therefore for other devices. The activation temperature of the getter must equal to or be less than the bonding temperature of MEMS cavities. Finally, to improve our understanding of the gettering mechanisms and design superior getter materials, thorough theoretical calculations must be developed to rigorously evaluate the contributions of the pores, grain size distribution, as well as the electronic structure

of the surface to the efficiency of the gas-trapping mechanism within such alloys.

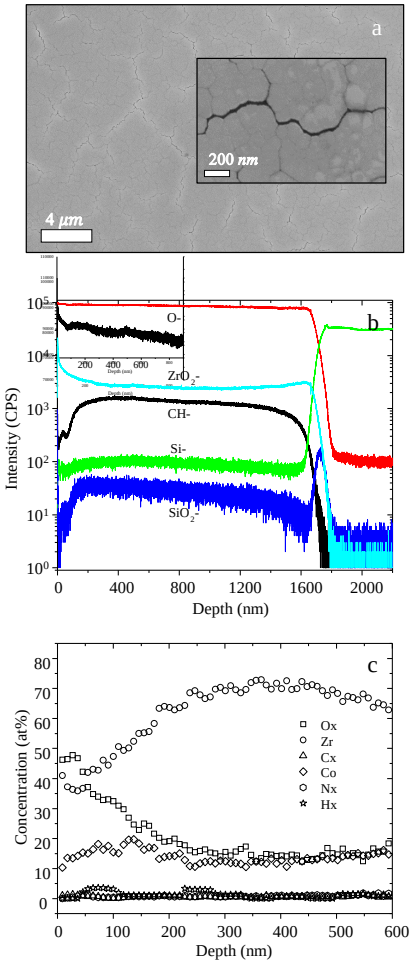

Figure 11. (a) SEM image of as received alloy. The inset is a close-up SEM image providing more details on the morphology of the alloy under investigation, (b) TOF-SIMS depth profile of alloy film constituents, with O^- signal shown in inset for clarity, and (c) TOF-ERD concentration profile of the important constituents in as received alloy (uncertainty ±1 at.%).

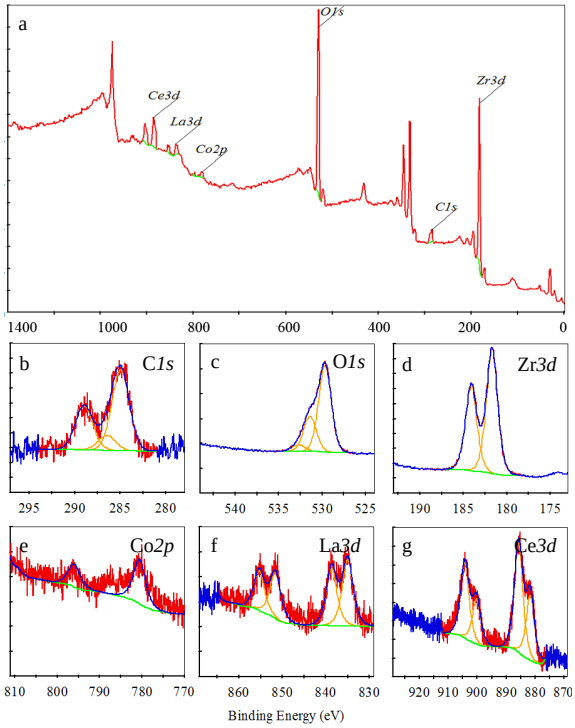

Figure 12. XPS of Zr-Co-REM alloy (a) Complete spectrum of as-received alloy, high resolution spectra of (b) C*1s*, (c) O*1s*, (d) Zr*3d*, (e) Co*2p*, (f) La*3d*, and (g) Ce*3d*. (red = raw counts, blue = fit, yellow = deconvoluted peaks, green = subtracted background)

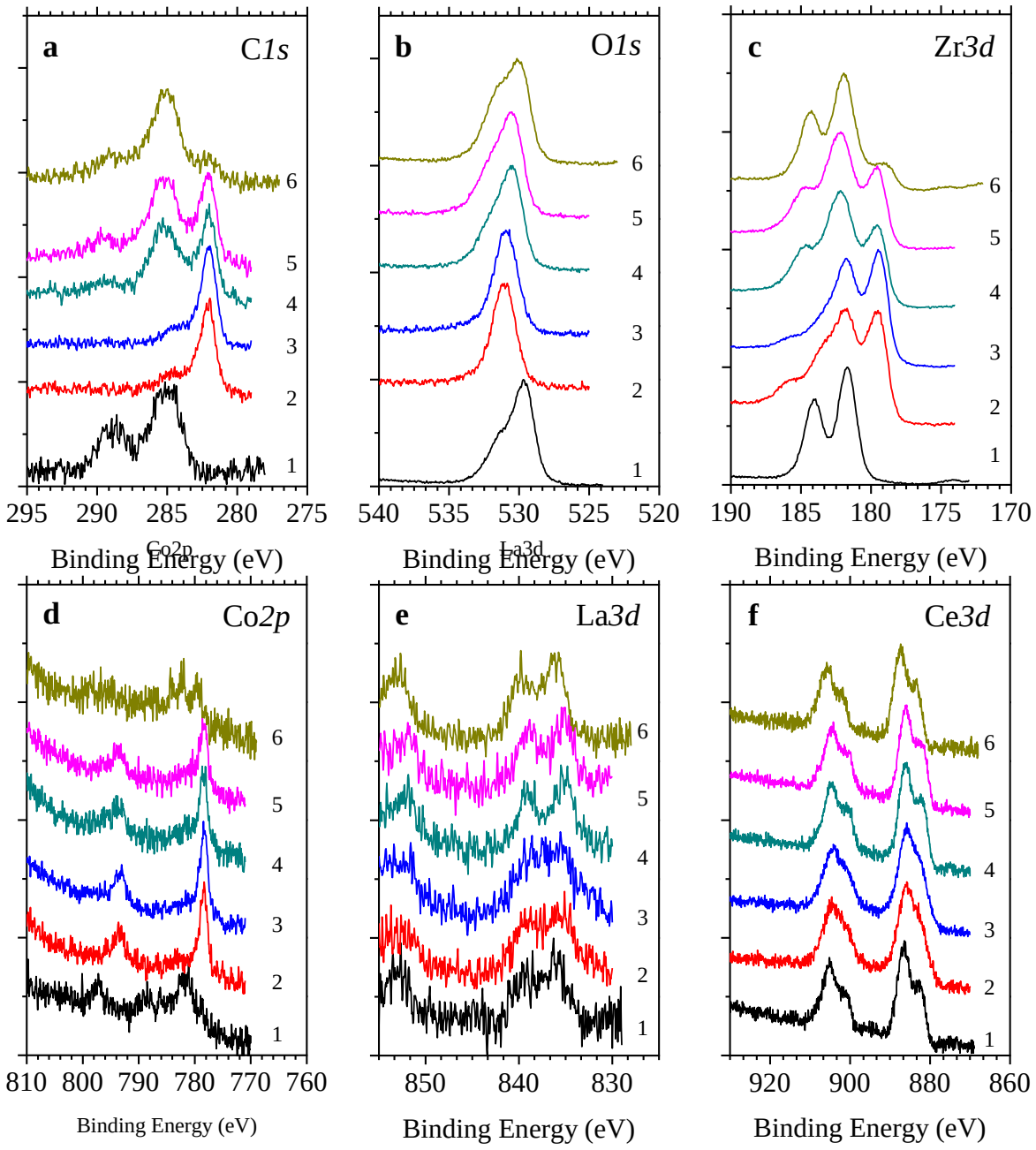

Figure 13. Evolution of normalized XPS spectra of (a) C*1s*, (b) O*1s*, (c) Zr*3d*, (d) Co*2p*, (e) La*3d*, and (f) Ce*3d* orbitals under the following consecutive treatments: (1) As received. (2) Annealed at 200 ºC. (3) annealed at 350 ºC. (4) sample cooled down to 25 ºC and exposed to 1.8×10^4 L of O_2 (30 min at 10^{-5} Torr). (5) Sample #4 exposed to 3.6×10^4 L of O_2. (6) Sample #5 stored in ambient conditions for 1 week.

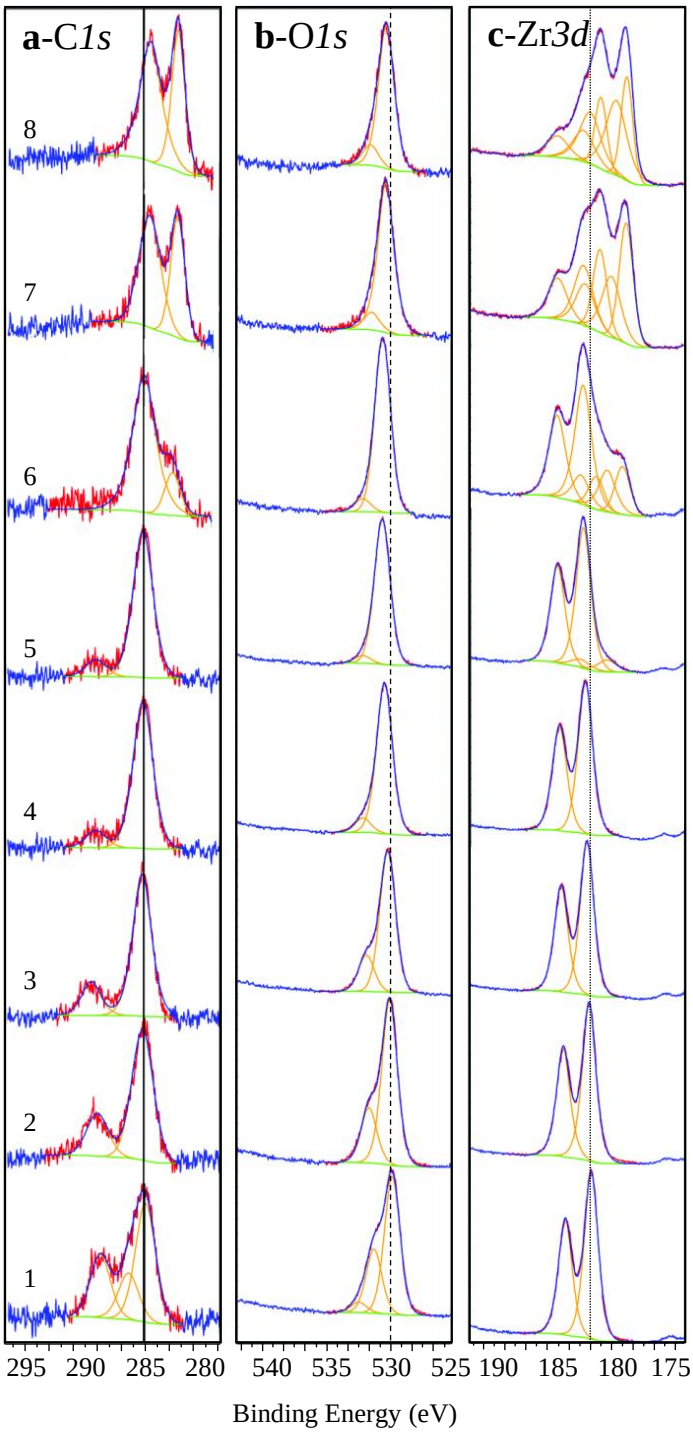

Figure 14. Evolution of normalized high resolution XPS spectra as a function of temperature of (a) C*1s*, (b) O*1s*, and (c) Zr*3d* orbitals. (1) 25^{o}C, (2) 50^{o}C, (3) 100^{o}C, (4) 150^{o}C, (5) 200^{o}C, (6) 250^{o}C, (7) 300^{o}C, (8) 350^{o}C. (red line represent raw data, blue line represents the overall fit, the deconvoluted peaks are represented by yellow traces, and the background is denoted by green lines).

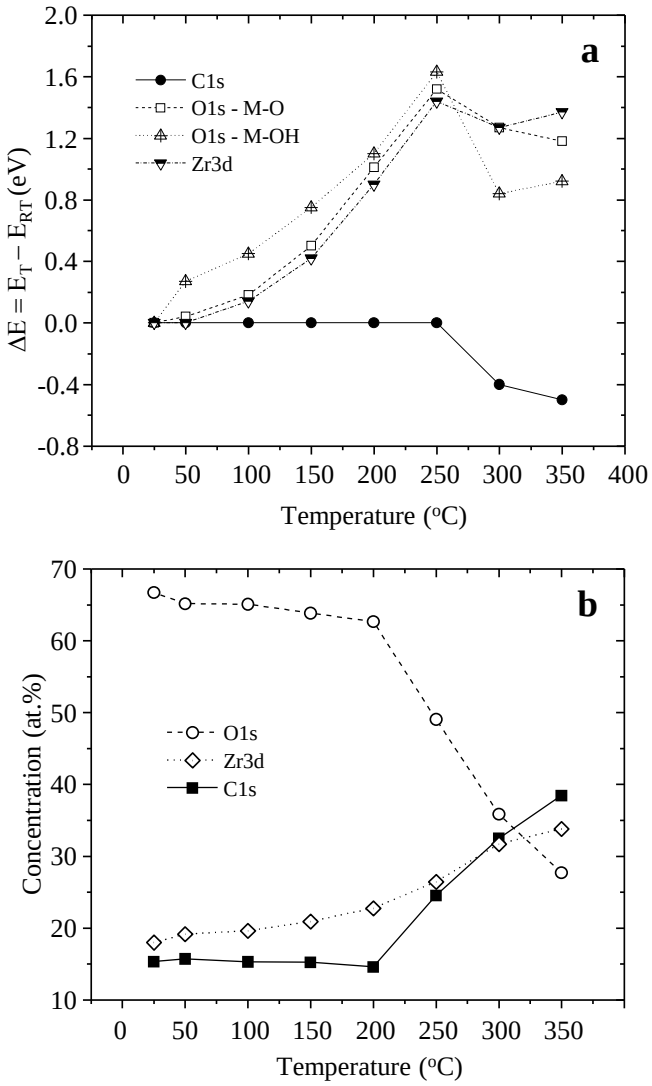

Figure 15. (a) Shift in binding energy with respect to room temperature upon thermal annealing for C*1s*, O*1s* and Zr*3d*, vs. temperature ($\Delta E = BE_T - BE_{25^oC}$). (b) Atomic concentration as evaluated by XPS measurement of C*1s*, O*1s*, and Zr*3d* orbitals as a function of temperature (±1%).

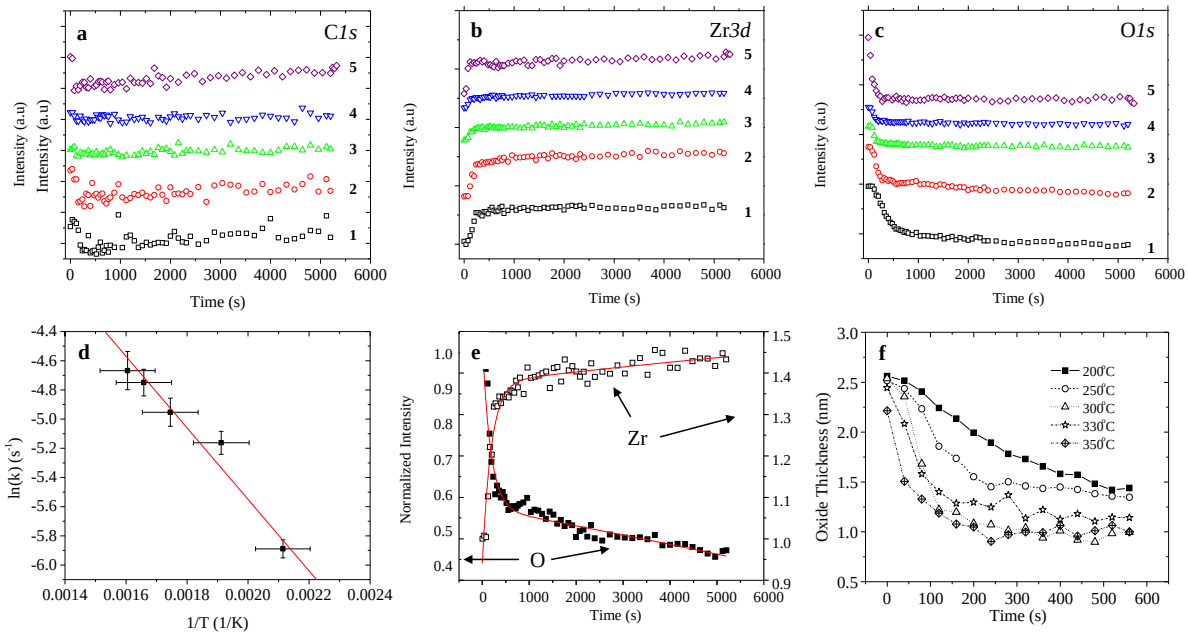

Figure 16. Integrated XPS signal evolution for: (a) C*1s*, (b) Zr*3d* and (c) O*1s* annealed at (1) 200 ºC, (2) 250 ºC, (3) 300 ºC, (4) 330 ºC, (5) 350 ºC. (d) Arrhenius plot of the diffusion rate for O. (e) Evolution of XPS intensity for O, Zr at 250 ºC. (f) Oxide thickness vs. time and temperature (±0.2 nm).

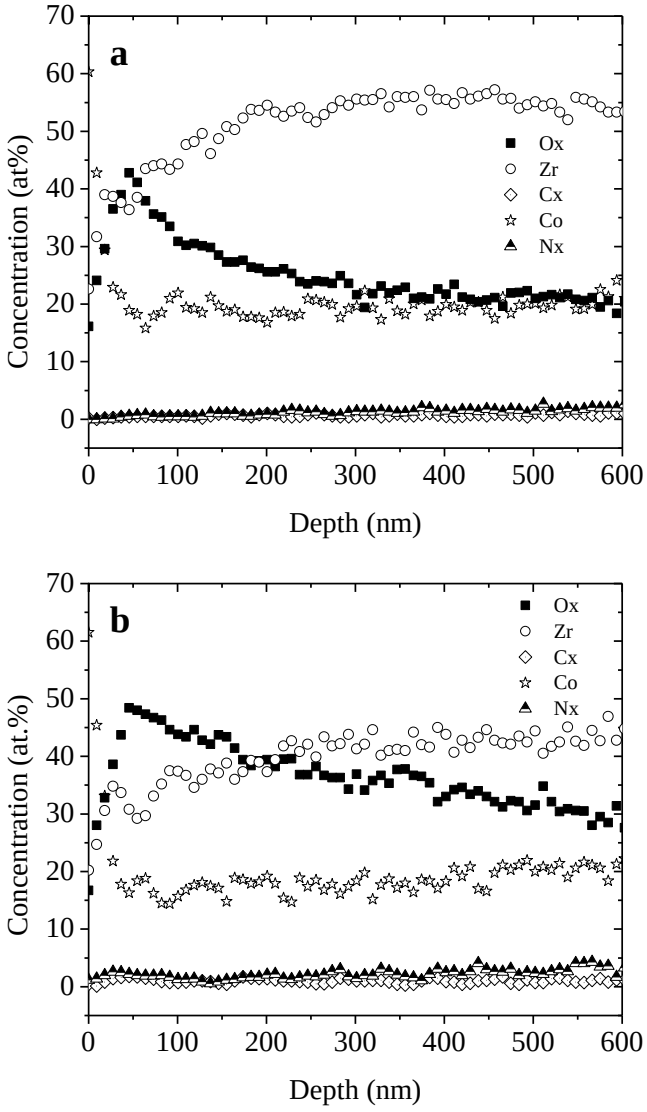

Figure 17. TOF-ERD depth profiles of getter sample (a) as-received, (b) treated in RTA at 400 ºC under Ar for 30 min.

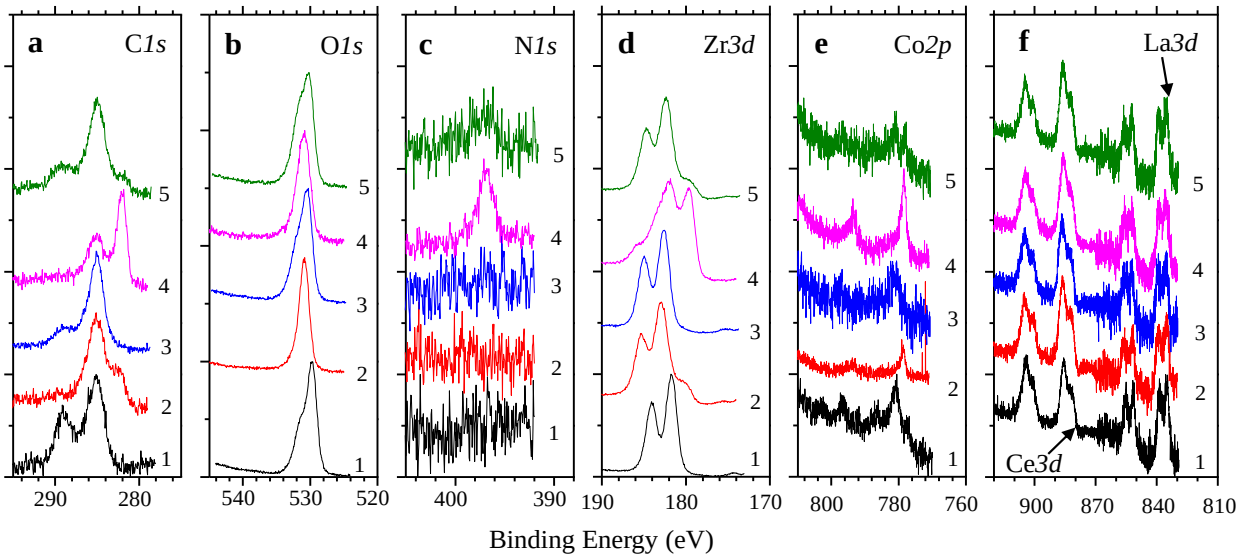

Figure 18. Evolution of normalized XPS spectra of (a) C*1s*, (b) O*1s*, (c) N*1s*, (d) Zr*3d*, (e) Co*2p*, (f) Ce*3d* and La*3d* orbitals; (1) as received (2) sample heated to 350°C in the presence of O_2 (10^{-5} Torr for 50 min) followed by cooling to room temperature under UHV (3) Sample 2 stored in ambient atmosphere (4) A new sample heated to 350°C under N_2 (10^{-5} Torr - 50 min) followed by cooling to 25°C under UHV (5) Sample 4 stored in ambient conditions.

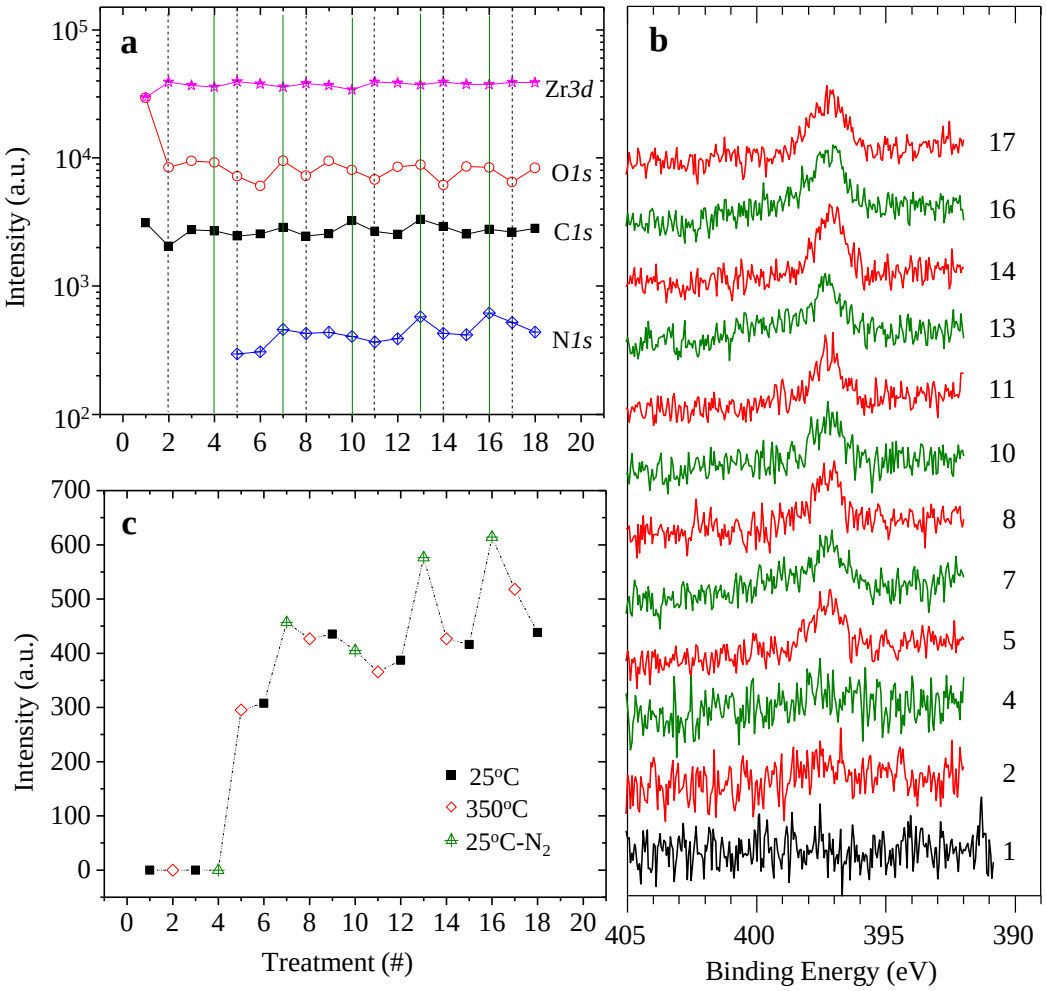

Figure 19. (a) Integrated XPS intensity for sample undergone repeated annealing at 350 ºC (----), cooling to 25ºC (no line), and dosing with N_2 (10^{-5} Torr – 20 min) (—). (b) Evolution of N*1s* signal as the sample undergone multiple annealing and nitriding steps (black = baseline measurement, red = 350 ºC, green = N_2 (1.2×10^4 L – 25 ºC)). (c) Evolution of normalized XPS intensity for N*1s* under several cycles of N_2 dosing at 25 ºC (⧋), annealing at 350 ºC (◇), and cooling down to 25 ºC (■).

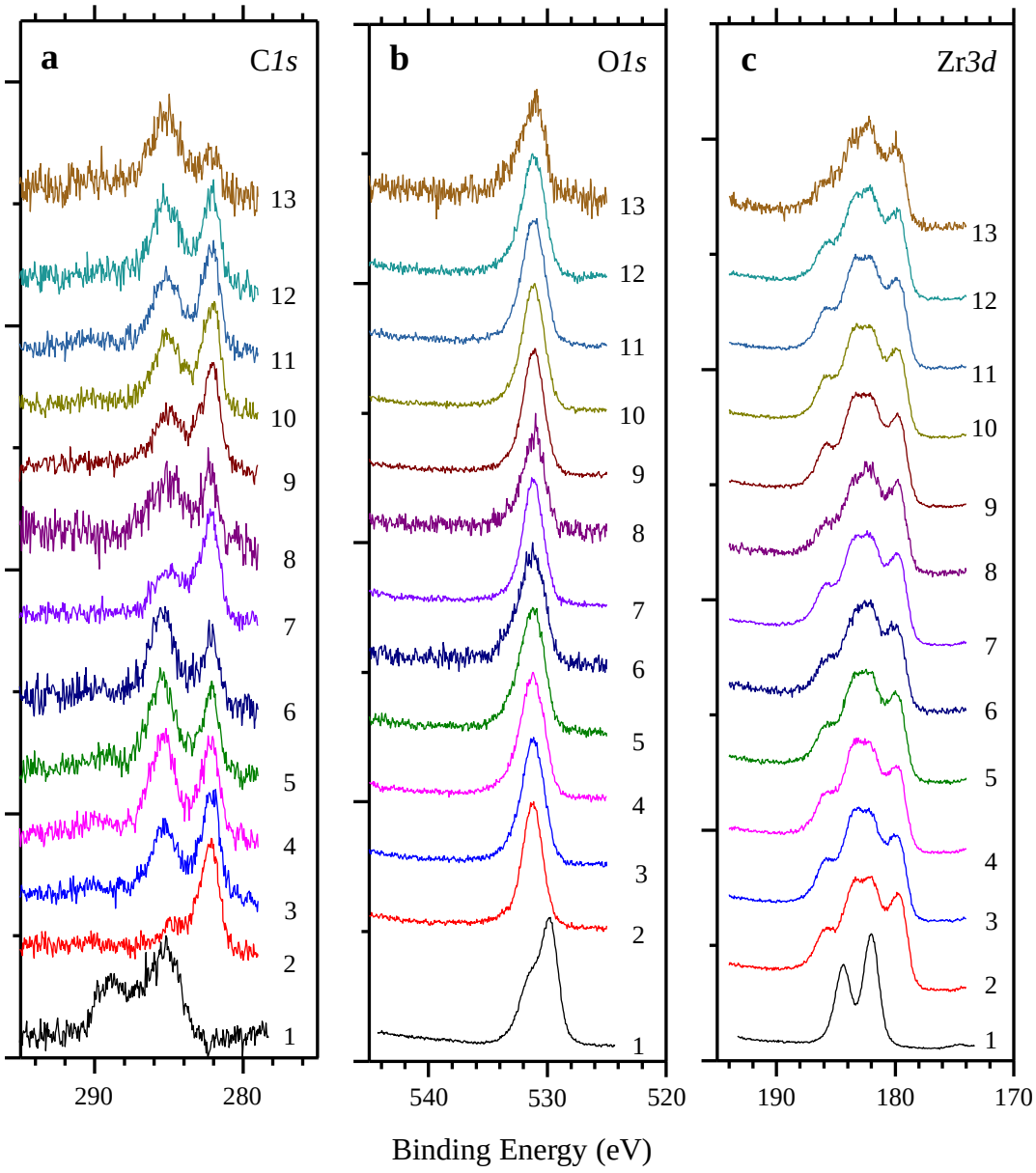

Figure 20. Evolution of normalized XPS spectra of (a) C*1s*, (b) O*1s*, (c) Zr*3d*, for samples under the following conditions: (1) untreated, (2) annealed at 350 ^{o}C, (3) sample #2 cooled down to 25 ^{o}C and dosed with 1.8×10^{4} L of CO_2 measured at 0^{o} take off angle. ARXPS measurements on sample #3 (4) 40^{o}, (5) 60^{o}, (6) 80^{o}. (7) Sample #3 heated to 350 ^{o}C and measured at 0^{o} and (8) 80^{o} take-off angles. (9) Sample #7 cooled down to 25 ^{o}C, (10) exposed to 1.8×10^{4} L of CO_2 and measured at 0^{o}, (11) 40^{o}, (12) 60^{o}, and (13) 80^{o}.

Table 5. Summary of XPS analysis of the alloy surface at (1) 25ºC (2) 200 ºC. (3) 350 ºC. (4) cooled down to 25 ºC and dosed with 1.8×10^4 L of O_2 (30 min at 1×10^{-5} Torr). (5) Sample 4 dosed with an additional 3.6×10^4 L of O_2. (6) Sample 5 stores in ambient conditions for 1 week. (spectra shown in **Figure 4.3**). M = Metal

			Atomic% (±1%) [**FWHM**±0.1 *eV*]					
	E_b		**1**	**2**	**3**	**4**	**5**	**6**
Orbital	**(**±0.2*eV*)	**Species**	**25ºC**	**200ºC**	**350ºC**	**O_2-01**	**O_2-02**	**Ambient**
C*1s*	282	M-C		14.6 [1.3]	16.3 [1.2]	8.6 [1.4]	8.5 [1.4]	1.7[1.4]
	283-284	M-C-O		7.6 [3.2]	8.3 [3.0]	13.5 [2.8]	15.8 [2.7]	
	285	C_xH_y	8.1 [2.2]					16.3 [2.5]
	286.5	Alcohol	1.5 [2.2]					
	289	Carboxyl	4.4 [2.2]			2.2 [2.8]	3.4 [2.7]	3.9 [2.5]
O*1s*	529.7	M-O	42.8			29	27	31.4
[1.8eV]	531.5	M-OH	17.5	26.8	22.9	13	13	20.8
	532.3	defect O^- /OH^-		5.2	4	2.9	3.5	
	533	Carboxyl	3.2					4.4
Zr3d5	179.4	Zr^0/ZrC		12.7 [1.4]	14.8 [1.3]	6.3 [1.3]	6.6 [1.4]	3.5 [1.9]
	180.5	ZrO_x		14 [2.4]	18.1 [2.4]	7.3 [2.2]	6.2 [2.1]	
	182	ZrO_2	16.9 [1.6]			10.2 [2.2]	9.8 [2.1]	13.6 [1.8]
	183.4	$Zr(OH)_2$		7.7 [2.4]	4.1 [2.4]			
Co*2p3*	778.5	Co^0		2.7 (2.7)	1.9 [2.2]	1.4 [3.5]	1.3 [3.2]	0.7 [3.5]
	780.6	CoO	1.4 [3.2]					
Ce*3d5*	882.2	Ce_2O_3	3.4 [3.5]	6.7 [3.5]	6.8 [3.4]	4.6 [3.5]	4.3 [3.5]	2.1 [3.5]
La*3d5*	835	La_2O_3 /$La(OH)_3$	0.8 [3.2]	1.9 [3.5]	1.6 [3.5]	1.0 [2.7]	0.8 [2.7]	0.7 [2.9]

Table 6. Summary of fitting parameters for the decay of XPS signal for O*1s* as a function of temperature.

Temperature (ºC)	Fitting Parameters	
	τ (s)	$k\times10^{-3}$ (s^{-1})
200	361 ± 22	2.8 ± 0.2
250	175 ± 14	5.7 ± 0.6
300	142 ± 14	7.1 ± 0.7
330	116 ± 11	8.7 ± 0.8
350	106 ± 14	9.4 ± 1

Table 7. Analysis for XPS spectra shown in. Figure 4.8. (1) as received (2) 350 ^{o}C + O_2 (10^{-5} Torr, 50 min) (3) Sample 2 stored in ambient conditions (4) New sample heated to 350 ^{o}C and dosed wtih N_2 (10^{-5} Torr, 50 min) and cooled down to 25^{o}C (5) Sample 4 stored in ambient conditions. M = Metal.

			Atomic% (±1%) [**FWHM**±0.1 *eV*]				
			Sample Number				
	BE			**O_2**			**N_2**
Orbital	**(**±0.2*eV*)	**Species**	**1**	**2**	**3**	**4**	**5**
C*1s*	282	M-C		2.6 [1.5]		12.8 [1.4]	1.4 [1.5]
	283-284	M-C-O		16.2 [2.7]		11.4 [2.6]	15 [2.7]
	285	Hydrocarbon	6.8 [2.2]		17.3 [2.0]		
	286.5	Alcohol	2.0 [2.2]		2.8 [2.0]		
	289	Carboxyl	4.2 [2.2]		4 [2.0]		4.4 [2.7]
O*1s*	529.7	M-O	43.3		35.4		31.9
[1.8eV]	530.6	M-O/-OH		47		20	
	531.5	M-OH	18.2		15.9	11.1	19.6
	533	Carboxyl	2.6		3.9		4.5
	533.6	O^{-}		4.9		2.0	
N*1s*	396.9					3.5 [1.8]	1.7 [3.5]
Zr*3d5*	179.4	Zr^{0}/ZrC		4.5 [2.1]		9.1 [1.4]	2.7 [2.0]
	180.5	ZrO_x				14.5 [2.5]	
	182	ZrO_2	16.6 [1.6]		15.8 [1.7]		14 [1.9]
	182.9	$Zr(OH)_x$		18.3 [1.9]			
	183.3	$Zr(OH)_2$				6.3 [2.5]	
Co*2p3*	778.5	Co^{0}				1.8 [2.9]	
	778.9	CoO_x		1.0 [3.5]			
	780.6	CoO	1.4 [3.5]		0.6 [3.5]		0.7 [3.5]
Ce*3d5*	882.2	Ce_2O_3	3.6 [3.5]	3.9 [3.9]	2.5 [3.5]	5.3 [3.5]	3 [3.5]
La*3d5*	835	La_2O_3 /$La(OH)_3$	1.3 [3.0]	1.5 [3.4]	0.9 [3.1]	2.0 [3.5]	1.2 [3.5]

Table 8. Semi-quantitative analysis of ARXPS data for examining surface reactivity with CO_2 *in situ*.

		Atomic% (±1%)							
		1	**2**	**3**	**6**	**7**	**8**	**10**	**13**

			T	25ºC	350ºC	25ºC-CO_2		350ºC		25ºC-CO_2	
Orbital	**BE** (±0.2eV)	**Species**	***θ***	**0º**	**0º**	**0º**	**80 º**	**0 º**	**80 º**	**0 º**	**80 º**
C*1s*	282	Metal-C			14.4	13.6	13.9	14.7	8.9	10.2	6.5
	283-285	Metal-C-O			3.4	10.1	21.1	8	24.5	14.8	29.9
	285	Hydrocarbons		5.75							
	286.5	C-O		3.1							
	289-289.5	Phys-CO		4.55		2.6					
	289.5-290.4	CO_2					2.2			2.8	4.5
O*1s*	529.7	Metal-O		44.2							
	531	Metal-OH		21.1	36.4	30.9	15	34.3	28.7	31	21.8
	532	C-O			9.8	12.9	16	9.7	7.3	11.5	9
	533	CO_2		3.3			5.2				3
Zr3d5	179.5	ZrC/Zr^0			14.5	10.6	8	11.1	14	10	9.1
	181.8	ZrO_2/ZrO_x/Zr-C-O		18.1	9.7	8.9	10.6	10.9	7.7	9.5	9
	183.2	$Zr(OH)_2$			11.8	10.4	8.1	11.4	8.9	10.3	7.3